Getting Close to Gravity: Developing the Experimental Techniques to Measure the Inverse Square Law of Gravity

Conner Gettings

A thesis submitted to the University of Birmingham for the degree of

DOCTOR OF PHILOSOPHY

Astrophysics and Space Research Group

School of Physics and Astronomy

College of Engineering and Physical Sciences

University of Birmingham

July 23, 2020

Abstract

The torsion balance has a long history of measuring weak forces. Its inherent design results in a very low rotational stiffness and some degree of immunity to tilt and horizontal accelerations coupling into the rotational motion of the suspended mass. Due to, however, the vertical distance of the centre-of-mass from the point of attachment, horizontal accelerations can couple strongly to the simple pendulum mode. This makes control of the torsion bob difficult. Additionally, at some level there will always be some coupling to rotational motion.

I present work on experimental techniques to circumvent these issues. This revolves around the Superconducting Torsion Balance (STB) - a novel torsion balance with zero fibre length, and the Air Bearing - a proof-of-concept experiment demonstrating centre-of-buoyancy tuning to decouple horizontal accelerations from the rotational mode. I designed and implemented the capacitive displacement sensor for the STB, where it is projected to give a signal-to-noise ratio greater than 1 for a signal of 2×10^{-17} N·m within a days integration. I employed finite element analysis of the magnetic forces in the superconducting suspension to demonstrate the feasibility of levitating the test mass. The Air Bearing demonstrates centre-of-buoyancy tuning to a precision of $\pm$ 0.3 mm.

Statement of Originality

This thesis reports the research I conducted during my PhD at the University of Birmingham between September 2016 and April 2020.

The work reported in Chapter 2 was originally led by Clive C. Speake with assistance from Christopher J. Collins. It has been published in:

C. C. Speake and C. J. Collins. Torsion Balances with Fibres of Zero Length. Physics Letters A, 382(16):1069-1074, Apr 26 2018.

The work reported in Chapter 3 includes both my original contributions as well as work from other group members. Specifically, in Section 3.1 the current experimental float was designed and implemented by myself, whereas the bearing and superconducting coil actuator design and implementation, as well as the source and test mass manufacturing procedures, were devised by Clive C. Speake and Christopher J. Collins. The signal and noise modelling in this section was originally led by Clive C. Speake and the results were first published in:

E. C. Chalkley, S. Aston, C. J. Collins, M. Nelson, and C. C. Speake. Testing the Inverse Square Law of Gravitation at Short Range with a Superconducting Torsion Balance. In The XLVIth Rencontres de Moriond and GPhyS Colloqium 2011, pages 207-210, Mar 20-27 2011.

The work then reported in Sections 3.2 and 3.3 was led by myself.

The work reported in Chapter 4 was led by myself with assistance from Clive C. Speake. We both worked on the models presented in this chapter while I performed all the measurements and their analysis. This work has been published in:

C. Gettings and C. C. Speake. A Method for Reducing the Adverse Effects of Stray-Capacitance on Capacitive Sensor Circuits. Review of Scientific Instruments, 90(2):025004, Feb 2019.

The work reported in Chapter 5 was led by myself with assistance from Clive C. Speake. Clive C. Speake worked on the models presented in this chapter while I performed all the measurements and their analysis. This work has been published in:

C. Gettings and C. C. Speake. An Air Suspension to Demonstrate the Properties of Torsion Balances with Fibres of Zero Length. Review of Scientific Instruments, 91(2):025108, Feb 2020.

Acknowledgements

To begin with, I must thank my supervisor Clive for allowing me to join him on an exciting and engaging PhD project. He's given me a new appreciation for experimental physics and the guidance he's provided throughout my time in Birmingham has not only been invaluable for getting me through the various pitfalls of PhD life, but will serve me well for the rest of my time in scientific research. A special mention must of course be given to our numerous discussions of progressive rock music in the pub.

I would like to thank Chris for his help in the lab, especially in the early stages of my PhD, and for helping me with my many technical and theoretical questions that I relayed to him over the years. A special thanks must also go to John and Dave for their invaluable help with LabVIEW and electronics issues. Without their input all my work would have taken twice as long (or even more). Additionally, I would like to thank Conor, my secondary supervisor, for our talks on issues outside of research and for fun times at pub club.

Thanks go to everyone in the ASR group for making it a great place to work and for the friendships that have been formed. A special mention goes to David for his IT support as well as his unflinching defence of the classic cup of tea over coffee at our 11 o'clock group tea/coffee breaks. I would also like to thank the inhabitants of G26 and G27, past and present, for many fun office parties. Long may they continue!

I'd like to thank my colleagues in the LP, BMS, MSF, SA and IMT, for introducing me to dialectical materialism, which has helped me appreciate science and the world as a whole in a completely different way, as well as giving me opportunities do good away from all the science. Our work has been a great way to appreciate the bigger picture, to help make society better, and a refuge when things didn't go as expected.

I'd like to thank all my friends, both here in Birmingham and back in Greenock and Glasgow, old and new, for the many memories and happy times that have taken the edge off of work. Finally, I want to acknowledge my family, especially my mum and brother, for their support during my PhD

and all my other studies. Without your help and sacrifices I wouldn't have made it this far. Last but not least, I'd like to thank Georgie for all the proof reading!

Contents

List of Figures

List of Tables

Chapter 1

Introduction

I have been trying to point out that in our lives chance may have an astonishing influence and, if I may offer advice to the young laboratory worker, it would be this—never neglect an extraordinary appearance or happening. It may be—usually is, in fact—a false alarm that leads to nothing, but may on the other hand be the clue provided by fate to lead you to some important advance.

Alexander Fleming

In 1798 Henry Cavendish performed the first laboratory based measurements of gravity by measuring the force of gravity between two masses using a torsion balance [1]. His experiment was an attempt to accurately determine the mass and average density of the Earth, but based on his measurements a value for the gravitational constant, G, could be found to within a few percent of the modern accepted value. This, along with Charles-Augustin de Coulomb's work on determining what would become Coulomb's law in 1785 also with a torsion balance [2], were the beginnings of precision measurements of weak forces. Cavendish's experiment had the test and source masses located approximately 23 cm away from each other. Since that time many other experiments have been performed to test the inverse square law of gravitation with mass separations at astronomical scales [3] down to tens of micrometres [4, 5]. What motivates these searches, especially at

sub-millimetre ranges, is the existence of several interesting theories that aim to solve some of the biggest issues in modern physics that would violate Newton's law of gravity at these scales and which lie within or near current experimental limits.

1.1 Problems with Gravity

The Hierarchy Problem

Nothing is more indicative of the trouble surrounding gravity than the theoretical issue posed by the hierarchy problem. In the case of gravity, this problem highlights the fact that there is no consensus as to why gravity is so much weaker than the other fundamental forces of nature. The fundamental energy scale of the electroweak scale is $m_{EW} \approx 250$ GeV/c^2 [6], while for gravity the Planck scale is defined as $m_{Pl} \approx 1 \times 10^{19}$ GeV/c^2. The hierarchy problem is related to the fact that the higher order loop terms in the associated field theory need to exactly cancel out in order to not 'raise' the the electroweak scale to the Planck scale. Coming to terms then with the reason behind this massive difference in scales is one of the biggest challenges in modern physics.

The Cosmological Constant Problem

The cosmological constant, from Einstein's theory of General Relativity, is needed to take into account the now observed accelerating expansion of the Universe [7, 8]. This constant is linked to what is now known as Dark Energy. The calculated value of this energy density from theory is $\rho_{vac} \approx 10^{92}$ g/cm^3 [9], while from observations the value is $\rho_{vac} \approx 6.76{\times}10^{-30}$ g/cm^3 $= 6.08{\times}10^{-10}$ J/m^3 [6]. This is assuming the highest energy possible is available to all virtual particles at the Planck scale and so is a worst case scenario and is another manifestation of the hierarchy problem. The difference then between theory and observations is around 120 orders of magnitude. While invoking supersymmetry lowers this to around 80 orders of magnitude of difference, the theoretical prediction remains insurmountable and this discrepancy is still unexplained by quantum field theory [10].

The Renormalisation Problem

The renormalisation problem relates to the fact that General Relativity cannot be quantised in the same manner as electromagnetic fields, and as such no coherent theory can be devised where the exchange of virtual particles for the gravitational force does not become unphysical [10, 11]. This means there is currently no consistent way to merge General Relativity with Quantum Mechanics and so as it currently stands, gravity cannot be unified to the other fundamental forces; we cannot progress from the Grand Unified Theory to the fabled Theory of Everything.

1.2 A Possible Solution: Large Extra Dimensions

Many theoretical solutions have been proposed to help alleviate the aforementioned issues. Most of them, especially those originating from String Theory, involve violating Newton's inverse square law at small mass separations. Some of these theories include string moduli, where scalar fields called moduli can couple to elementary particles leading to microscopic forces, and the fat graviton scenario, where the mediating particle for gravity is massive and finite in size such that it does not interact with anything over scales smaller than its own size [10]. Both of these scenarios, if true, would effectively lower the theoretically derived cosmological constant from Section 1.1 due to the changes they introduce to the gravitational force over these ranges, and hence bring it closer to the observed value. See Adelberger *et al.* [3] for a detailed review of these different theories. Regardless of the theory, for comparisons between the experiments that try to evaluate these possibilities it is useful to have a generalised expression for any of the violations to Newtonian gravity. This generalised term can be characterised by an additional Yukawa-type potential on the Newtonian gravitational potential energy as follows [12],

$$V(r) = -\frac{GM_1M_2}{r}\left(1 + \alpha e^{-\frac{r}{\lambda}}\right), \tag{1.1}$$

where G is the gravitational constant (at infinite distance), r is the distance between some point masses M_1 and M_2, and α and λ are the strength and range of the new force violating Newton's inverse square law respectively. Here α is dimensionless and the Compton wavelength, $\lambda = \frac{\hbar}{mc}$,

relates the range to the mass, m, of the mediating particle of the new force. The myriad theories of possible violations are beyond the scope of this thesis, instead the discussion that follows will focus on one particular theory that originates from String Theory: supersymmetric large extra dimensions, due to the fact that for certain conditions it could be directly tested by the experiment that forms the basis of this thesis, the Superconducting Torsion Balance described in Chapter 3.

The concept of large extra dimensions originates from a model proposed by Arkani-Hamed *et al.* [13, 14]. There it is suggested that there could be extra spacial dimensions, so called 'large' because they are much larger than the Planck scale, compactified into different geometries. Then, if gravity was the only force that could propagate into these dimensions, then not only would it help to explain why it is so much weaker compared to the other fundamental forces due to the loss of gravitational flux to these extra dimensions, but it would in turn allow its unification to the other forces at a much lower energy scale than the Planck scale. This helps to overcome the hierarchy problem. In this model, the strength and range of the altered gravity, α and λ in Equation 1.1, depends on the specific geometry and number, n, of the extra dimensions respectively, where the new dimensions would appear as a new Yukawa-type force due to the exchange of massive spin-2 particles called Kaluza-Klein gravitons [3]. Typically $\lambda = R$ where R is the range of the force due to the Kaluza-Klein particles and hence also the radius of these new spatial dimensions. For the case of the large extra dimensions having an equal flat torus geometry, when $n = 1$ then $R \approx 10^{12}$ m and $\alpha \approx 2$, and this has been ruled out by solar system based observations [3]. When $n = 2$, $R \approx 100$ μm and $\alpha \approx 4$, and this has also been ruled out by experiment [15]. When $n > 2$, R is less than a nanometre which is beyond current experimental limits for torsion balance based experiments [3, 5].

A more promising approach was proposed in [16], where the idea of large extra dimensions was combined with a supersymmetric field theory to give a Supersymmetric Large Extra Dimensions theory. This is based on the concept that while supersymmetry is broken in the 'branes' of our 3-dimensional world to at least below the electroweak scale at $m_{EW} \approx 250$ GeV/c^2 [6], it holds to a much lower scale in the 'bulk' of the 2 extra spacial dimensions. This means the zero-point energy

densities due to particles in the brane are cancelled by those in the bulk, with the net zero-point energy density contributing to Dark Energy, and the corresponding cosmological constant, coming from particles in the bulk alone. This gives a cut-off wavelength to the zero-point energy density of Dark Energy that should lower its theoretical value which helps to solve the cosmological constant problem. Using the observed value of this energy density, $\rho_{vac} \approx 6.08 \times 10^{-10}$ J/m^3 [6], a simple calculation can be performed to determine this zero-point energy cut-off wavelength, a, for Dark Energy:

$$E_{vac} = \frac{hc}{a} \implies \rho_{vac} = \frac{E_{vac}}{V} = \frac{3}{4\pi a^3}\frac{hc}{a} \approx \frac{\hbar c}{a^4}. \tag{1.2}$$

This gives a length scale for Dark Energy of $a \approx 85$ μm. Equating this to the radius of the 2 large extra dimensions, $a = 2\pi R$, we have $R \approx 14$ μm, where it is assumed the 2 extra dimensions have equal radii. We can equate this radius to λ in Equation 1.1, and so this implies if we measure the inverse square law of gravity between masses with a separation of this scale then violations could be detected. This is an important result, because compared to the scale lengths suggested by the non-supersymmetric large extra dimensions theory, it has not been ruled out by experiment and is not unrealistically far from current experimental limits.

Another important consequence of this theory is that it predicts the supersymmetry breaking energy scale, E_{Sym}, in the brane. Using the extra dimensional radius, R, calculated from Equation 1.2, this energy is given by [16]:

$$E_{Sym} \approx \frac{\hbar^{\frac{3}{4}} c^{\frac{7}{4}}}{(2\pi R)^{\frac{1}{2}} G^{\frac{1}{4}}} \approx 8.4\,\text{TeV}. \tag{1.3}$$

The current highest energy probed by the Large Hadron Collider is approximately 6.5 TeV [17] and so the predictions from Supersymmetric Large Extra Dimensions theory have not yet been ruled out.

In addition to knowing a range, λ, the relative strength to Newtonian gravity, α in Equation 1.1, of the violations to the inverse square law due to the presence of the large extra dimensions must also be known. This depends on the geometry of the extra dimensions [18, 19]. In the simplest case where the 2 dimensions have been compactified onto the same geometry and have the same

radii, and for the simplest geometries (a sphere and a torus), we find [19]

$$\begin{aligned} \alpha_{sphere} &= n+1, \\ \alpha_{torus} &= 2n. \end{aligned} \tag{1.4}$$

For 2 large extra dimensions, $n = 2$, we have $\alpha_{sphere} = 3$ and $\alpha_{torus} = 4$. Of course, different geometries and more complicated compactifications involving more than one geometry would result in different values.

It is important to note that any violations of the inverse square law of gravitation at small scales could be due to a number of possible theories. It could be the geometrical effect of the extra spacial dimensions or it could be due to a new mediating boson [5]. As such, if a violation was detected then further investigation would be needed to differentiate between these different possibilities. One way to do this would be to see if this violation of Newtonian gravity also violated the equivalence principle, as not all bosons would necessarily couple to matter in a uniform way [20] while the geometrical effect of extra dimensions would always adhere to the equivalence principle.

1.3 Environmental Landscape

1.3.1 Current Experimental Limits

From Equation 1.1, we can create an α-λ plot to show what region of this parameter space has been ruled out by previous experiments to a 95% confidence level and as such where Newtonian gravity still holds, and which region has yet to be investigated and the associated theories which have yet to be ruled out. This is shown in Figure 1.1. Crucially, this figure shows the projected sensitivity of the Superconducting Torsion Balance experiment here in Birmingham, described in Chapter 3, and its relation in the parameter space to the many proposed theories including that of Supersymmetric Large Extra Dimensions. The experiments shown in this figure are torsion balance based, with the exception of the IUPUI 2014 experiment which was based around a cantilever design [21]. This graph can be extended to much larger and smaller values of both α and λ, as in [5]; where towards smaller α and larger λ experiments become more geophysical and solar system based, whereas

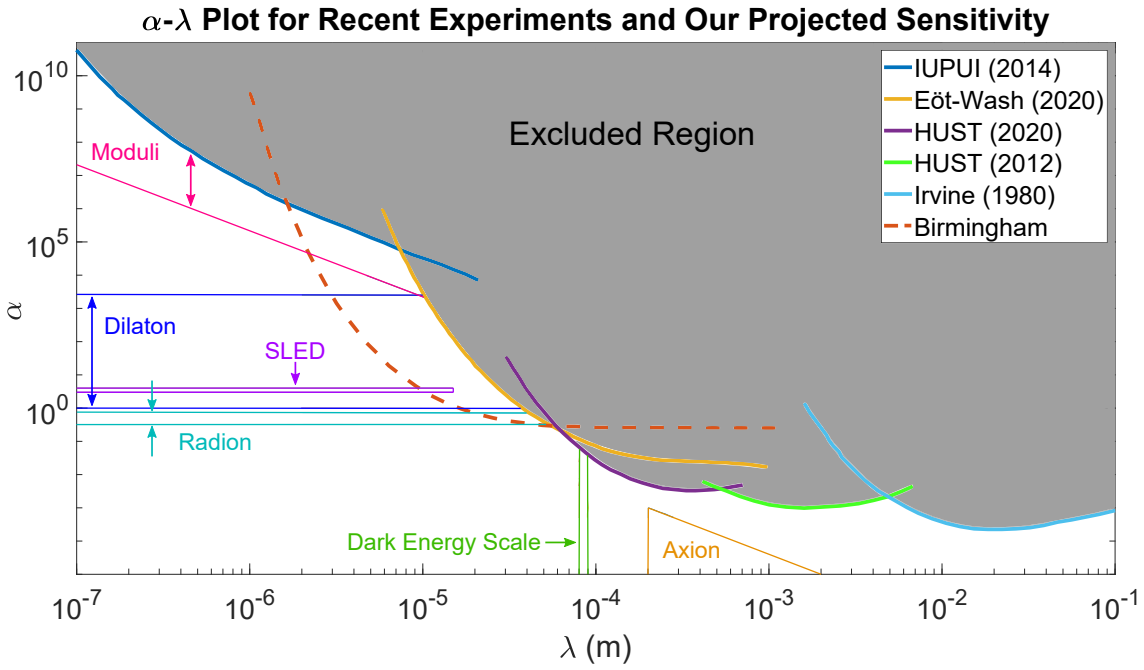

Figure 1.1: An α-λ plot showing the region of this parameter space that has been ruled out by the previous experiments described in references [21, 22, 23, 24, 25]. This region, where Newtonian gravity still holds, is excluded at a 95% confidence level. Also shown is the region yet to be investigated and the possible theories yet to be probed as summarised in references [3, 4, 5]. Of note is the projected sensitivity of the Superconducting Torsion Balance experiment here in Birmingham which is described in Chapter 3, and the possible Supersymmetric Large Extra Dimensions (SLED) region described previously in Section 1.2 which could be tested by this experiment.

toward larger α and smaller λ they tend toward cantilever based designs, and ultimately atomic force microscope and particle collider experiments. What follows will be a brief discussion of the previous experiments shown in Figure 1.1.

1.3.2 Previous Tests of the Inverse Square Law of Gravity

Irvine Experiment

The Irvine experiment, performed at the University of California in 1980, still provides the best constraints on α at the centimetre scale [22]. This experiment consisted of a copper cylinder test mass attached below one end of a bar on a torsion balance. The test mass was positioned inside the source mass which was stainless steel pipe. The source mass could be positionally modulated in the direction perpendicular to the torsion bar along a horizontal rail, which would induce a gravitational torque on the torsion balance. At the opposite end of the torsion bar to the test mass were electrostatic plates that could be used to control the torsion balance. The rotational displacement sensor for the torsion balance was an optical lever. The whole setup was placed in a copper vacuum chamber. This design is shown in Figure 1.2 [5].

The results from this experiment were in good agreement with Newtonian gravity, and they constrained the value on α of a violation to Newtonian gravity to $\alpha < 2 \times 10^{-4}$ at $\lambda = 2$ cm [22]. Apart from uncertainties related to the geometrical parameters of the experiment, the biggest source of uncertainty present in the measurements was due to microseismic and gravitational noise.

IUPUI Experiment

The IUPUI experiment, performed at the Indiana University–Purdue University Indianapolis in 2014, is not a torsion balance experiment but rather a cantilever based experiment [21]. This is because it was designed to probe λ from a few micrometres down to the tens of nanometres scale which is beyond the capabilities of current torsion balances. This experiment consisted of a gold-coated sapphire spherical test mass glued to a cantilever that was free to oscillate. The source mass consisted of a disk, whose surface contained a pattern of gold and silicon sectors. The

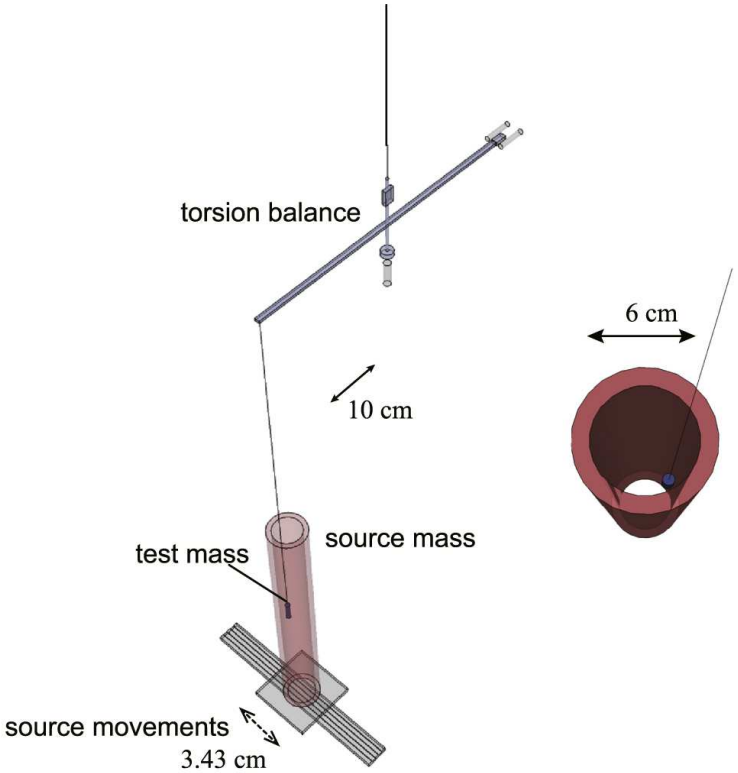

Figure 1.2: A graphic diagram of the Irvine experiment performed at the University of California in 1980; taken from the review of the field by Murata and Tanaka [5].

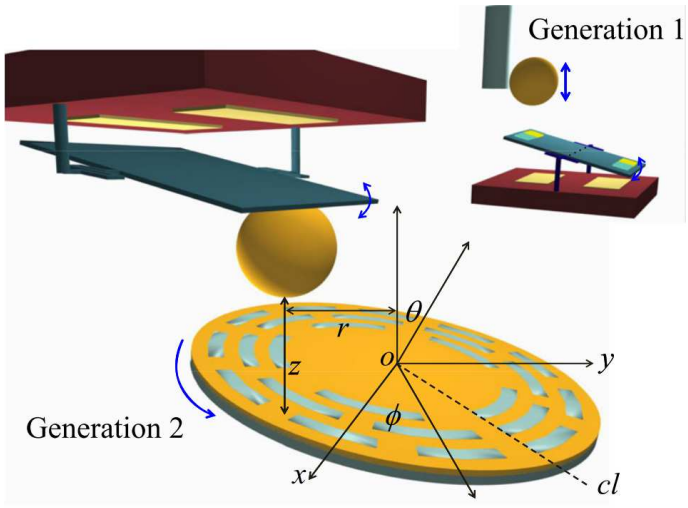

Figure 1.3: A graphic diagram of the IUPUI experiment performed at the Indiana University–Purdue University Indianapolis in 2014; taken from the paper by Chen *et al.* [21]. It shows the test mass attached to a cantilever, while a previous version of the setup, labelled Generation 1, is shown for comparison where the there was no separate mass attached to the cantilever.

disk was then rotated, and the differential density pattern would cause the test mass to oscillate. The test mass could be controlled with piezoelectrically driven micro-positioners, while the source mass disk was controlled via an air bearing spindle. The motion of the test mass on the oscillator was measured via a capacitive displacement sensor. This setup was contained within a vacuum chamber, a design of which is shown in Figure 1.3 [21].

The results from this experiment constrained the α for any violation to Newtonian gravity over a range of λ=30-8000 nm by a factor of up to 10^3 over previous limits [21]. At these mass separations, the biggest source of uncertainty came from the Casimir force between the masses masquerading as a gravitational signal, which in this case could at the least have been over a factor of 10 larger than the gravitational force. This experiment was able to suppress this force by coating the masses in gold to a thickness larger than that of the plasma wavelength in gold which is 135 nm, resulting in an attenuation of the Casimir interaction between the underlying structure of the masses by a factor greater than 10^6. These gold coatings had the added bonus of shielding against electrostatic noise forces as well.

HUST Experiments

The HUST experiments, performed at the Huazhong University of Science and Technology, were torsion-balanced-based and were designed to be null experiments for Newtonian gravity [23, 24]. Both experiments had similar designs. The 2012 experiment had a novel symmetric I-shaped torsion pendulum and source mass holder, with tungsten source and test masses placed at either end of the I-shaped designs. The source masses were driven linearly toward and away from the test masses with a motor. On one end of both the torsion pendulum and source mass holder, the masses were kept at greater separations from each other but were appropriately larger in order to counteract a Newtonian torque due to the unbalanced forces, but allowing any non-Newtonian effects to impart a torque on the test masses and the torsion pendulum from the other set of masses that were at a much smaller separation. The motion of the torsion pendulum was measured with an autocollimator. A gold-coated beryllium-copper membrane was placed between the source and test masses to act as shield to electrostatic noise sources. Capacitive actuators were used to control the torsion pendulum. This setup was contained in a vacuum chamber, a design of which is shown in Figure 1.4 [23].

The 2020 experiment's main physical difference was a change in the source mass setup. The tungsten source masses were now arranged on a disk shaped 'attractor'. The surface of this disk was held parallel to the I-shaped torsion pendulum and the test masses, and the disk rotated about a horizontal axis at a nominal drive frequency. A similar scheme to the 2012 experiment was used to allow for a Newtonian null measurement, where the disk shaped 'attractor' consisted of alternating tungsten source and compensation masses at greater separations. This updated design is shown in Figure 1.5 [24].

The 2012 experiment constrained α in the range $\lambda = 0.7 - 5.0$ mm by up to an order of magnitude more compared to previous experiments over the same range [23]. This experiment was ultimately limited by the ability to remove the Newtonian signal, as it would have swamped any non-Newtonian signal. The 2020 experiment constrained the value on α of a violation to Newtonian gravity to $\alpha \leq 1$ at $\lambda = 48$ μm [24]. This experiment overcame the issues of the negating of

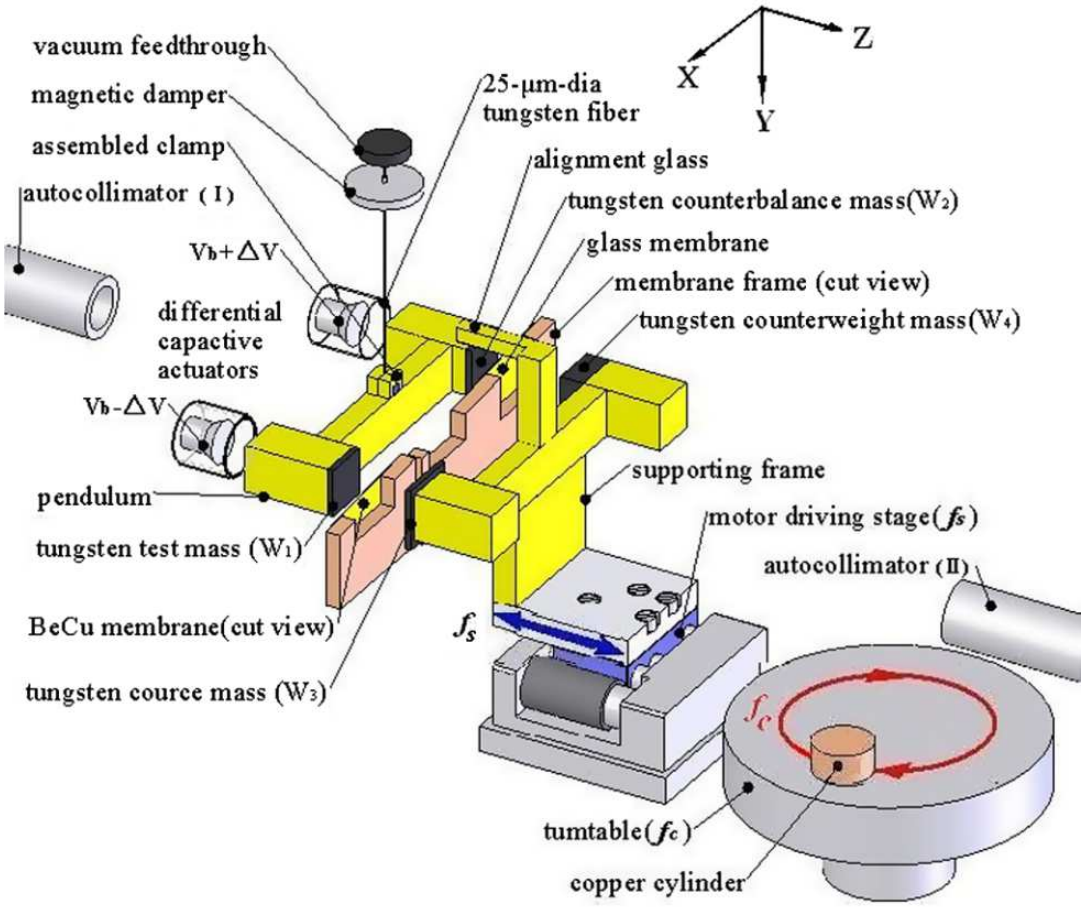

Figure 1.4: A graphic diagram of the HUST experiment performed at the Huazhong University of Science and Technology in 2012; taken from the paper by Yang *et al.* [23].

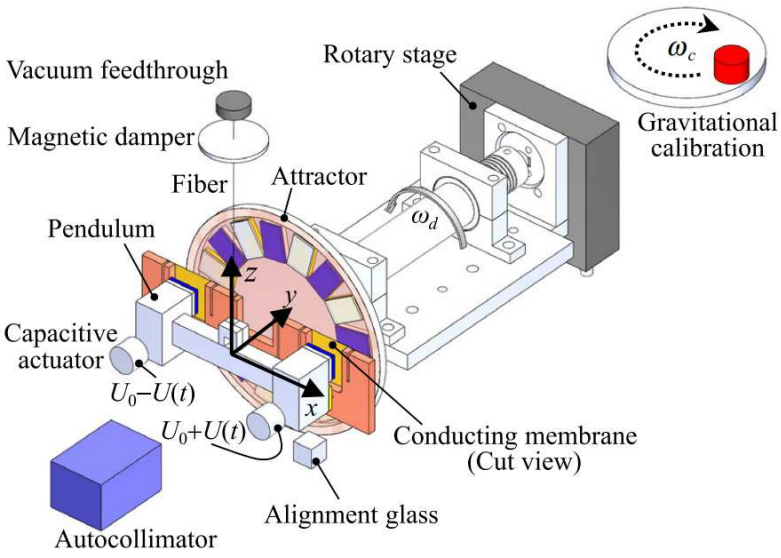

Figure 1.5: A graphic diagram of the HUST experiment performed at the Huazhong University of Science and Technology in 2020; taken from the paper by Tan *et al.* [24]. The alternating colours on the 'attractor' disk represent the tungsten source and compensation masses.

the Newtonian signal by using the new 'attractor' design. It also reduced another significant noise source which was the vibration of the shielding membrane between the source and test masses which coupled into residual surface potential related torques on the test masses and torsion pendulum. They made this improvement by using a different type of drive unit on the attractor. This vibration, however, was still the main source of uncertainty in the measurements.

Eöt-Wash Experiment

The Eöt-Wash group's most recent experiment, performed at the University of Washington in 2020, currently provides the best constraints on Newtonian strength Yukawa-type interactions at small length scales with a traditional torsion balance design [25]. This experiment consisted of a torsion balance detector and disk-shaped test mass located above a rotating disk-shaped source mass 'attractor'. The detector and 'attractor' masses both had a novel 18-fold and 120-fold azimuthal symmetry hole pattern which allowed for simultaneous measurements of torques at two different length scales. The masses themselves were made of platinum foils attached to glass annuli and were gold-coated. The torsion balance detector was placed in a gold-coated electrostatic shield that

Figure 1.6: A rendering of the Eöt-Wash group's experiment's torsion balance detector and 'attractor'. The experiment was performed at the University of Washington in 2020. The render is taken from the paper by Lee *et al.* [25].

surrounded it almost entirely, with a goal-coated beryllium-copper foil located directly between the detector and 'attractor'. In addition to this, the detector was also placed within several layers of μ-metal to shield against magnetic sources. The rotation of the detector was measured with an autocollimator and the 'attractor' could be rotated with a turntable motor. A rendering of the torsion balance detector and its test mass along with the source mass 'attractor' is given in Figure 1.6 [25].

This experiment constrained the value on α of a violation to Newtonian gravity to $\alpha \leq 1$ at $\lambda = 38.6$ μm, and the results imply a maximum radius of $R \approx 30$ μm for large extra spatial dimensions

(assuming they have a toroidal shape) [25]. The biggest source of noise in this experiment was environmental vibrations coupling into the patch fields of the shield between the detector and 'attractor' masses, leading to torque noise on the detector.

1.4 Common Experimental Issues

Many inverse-square law experiments share common issues, especially those based on the use of a torsion balance, beyond the expected problem of small signals due to the small masses required for sub-millimetre mass separations. As described in [22], one of the main limiting factors on the experiment's sensitivity was seismic noise imparting a torque onto the torsion balance. For the experiments in [24] and [25] the biggest source of uncertainty was the vibration of the shield between the test and source masses directly coupling into torque noise due to surface potentials. Improved seismic isolation would be an obvious solution, however this is difficult to achieve at low frequencies (typically < 1 Hz) where torsion balances tend to operate. Removing the shields used between the source and test masses would remove this source of noise, but then increased electrostatic noise from the masses themselves may dominate. Also, for $\lambda < 50$ μm maintaining a shield between the masses starts to become difficult to achieve. Another issue with the experiments described in [24] and [25] is that they directly measured the inverse square law down to mass separations for $\lambda > 50$ μm and then extrapolated the data down to the stated values using models acting within given error bounds. This then introduces the question of the validity of these models and the assumptions made about gravity over these ranges. The possible dangers of this modelling approach are highlighted in a previous experiment by the Eöt-Wash group [26], where in the process of changing between different setups deformations of the masses occurred. These were large enough to affect the measurements and, while in this case they were identified and accounted for, it raises the important issue of what other possible deformations and systematic effects might not be accounted for in such models. Improvements to some of these experiments are possible, such as in the Eöt-Wash group's most recent work, where to overcome seismic noise coupling into the patch fields on the experiment they plan to implement an active system to reduce vertical

vibrations [25].

What is required then, are novel designs and experimental techniques that would start to overcome these problems. Measuring the inverse square law of gravity directly below 50 μm mass separations, rather than extrapolating data, would realistically require the removal of any physical electrostatic shielding between the test and source masses due to the issues stated previously. These direct measurements would provide more reliable limits on violations to Newtonian gravity in this λ range. Also, more sensible choices of source and test mass geometries could reduce the Newtonian signal compared to any possible violation, making it easier to detect. The reduction of the coupling of seismic noise, and other horizontal forces and accelerations due to environmental vibrations, to the rotational mode of the torsion pendulum detector then becomes essential as this was a limiting factor for the most recent experiments. If the centre-of-mass and centre-of-buoyancy of suspended objects are aligned exactly then this is achieved. Additionally, the vertical distance between the attachment point of fibres and the centre-of-mass of torsion balances results in a simple pendulum mode that is difficult to control without increasing the rotational stiffness of the devices, limiting their measurement sensitivity. Removing these fibres, and suspending the torsion 'bob' and controlling it through external actuators could resolve these issues. In this thesis a novel experimental design and associated techniques, with these ideas in mind and based on the inherent advantages of the traditional torsion balance, are described with the aim of achieving these goals.

1.5 Thesis Overview

In this thesis I present my work on developing the experimental techniques to enable reliable measurements of the inverse square law of gravity down to mass separations of the order of 10 μm. This has revolved around working on the Superconducting Torsion Balance experiment and its capacitive displacement sensor, as well as on the Air Bearing experiment.

Chapter 2 provides a succinct summary of the concepts of the rotational stiffness and centre-of-buoyancy tuning of a suspended torsion bob and the necessary theory to enact them, applied to

the case of the Superconducting Torsion Balance, as published in [27]. In Chapter 3 a thorough description of the Superconducting Torsion Balance itself is given, where my contribution to it is highlighted. Chapter 4 details the work on the capacitive displacement sensor for use with the test mass of the Superconducting Torsion Balance, as published in [28]. In Chapter 5 the Air Bearing experiment, which was developed to showcase the principle of the centre-of-buoyancy tuning described in Chapter 2, is described in full as published in [29].

Chapter 2

Torsion Balances with Fibres of Zero Length

The economic anarchy of capitalist society as it exists today is, in my opinion, the real source of the evil. We see before us a huge community of producers the members of which are unceasingly striving to deprive each other of the fruits of their collective labour—not by force, but on the whole in faithful compliance with legally established rules.

Albert Einstein

In this chapter I give an overview of the theory behind torsion balances with fibres of zero length. This explains the premise of the in-situ tuning of the rotational stiffness and centre-of-buoyancy of suspended objects through the use of external actuators. This is a summary of the work in the paper 'Torsion Balances with Fibres of Zero Length' [27] of which I was not an author. The figures in this chapter were also copied from this paper and then amended with additional labels. I give a concise account of the general cases described in this paper applied specifically to the Superconducting Torsion Balance described in Chapter 3 and its superconducting magnetic actuators, due to its importance in underpinning the motivation for that experiment's design and also to that of the

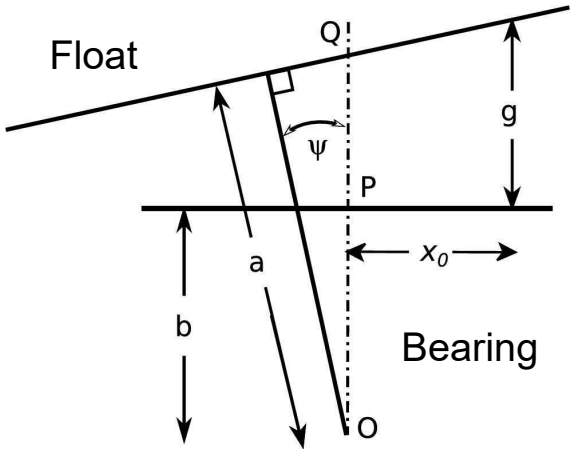

Figure 2.1: A diagram showing the position of a superconducting magnetic actuator located at x_0 from the symmetry axis of the bearing that holds the actuator in place, and how the parameters of the geometry can be used to calculate the gap, g, between the actuator's location and the inner surface of the float. The float is a levitated object whose motion in the horizontal plane is controlled by said actuators. This diagram is taken from the paper by Speake and Collins [27].

Air Bearing described in Chapter 5.

2.1 Rotational Stiffness Tuning

The rotational stiffness of a levitated object called the float, whose motion in the horizontal plane of the laboratory is controlled via applied forces due to the Meissner effect from superconducting coils on an object called the bearing, can be tuned by changing the relative stiffnesses of these actuators. This can be done by changing the magnitude of the persistent currents in these coils, while taking into account their relative positions to one another and with the float. Consider one such actuator located at a point x_0 from the symmetry axis of the bearing, as shown in Figure 2.1 [27]. The change in gap between the actuator and the position on the float's inner surface directly opposite it due to the rotation of the float, $g(\psi)$, around the centre-of-geometry of the setup, O, can be described as

$$g(\psi) = \frac{a}{\cos\psi} - b + x_0 \tan\psi, \tag{2.1}$$

where the symbols correspond to those in Figure 2.1. Here the linear displacement of the float will be ignored as it would nominally be negligible in a servoed system.

The stiffness of the actuators can be expressed in terms of the change in energy, ε, stored by them with regards to the changing gap, much like the stiffness of a spring being expressed through its stored energy changing with its length. It can be assumed that energy can also be stored by the float's rotation alone, with no change in the gap [27]. As such, two stiffness terms for the superconducting actuators can be defined,

$$k_{\psi\psi} = \left[\frac{d^2\varepsilon(\psi, g = const)}{d\psi^2}\right]_{\psi=0}, \tag{2.2}$$

for when there is no change in gap, and

$$k_{\psi\psi}^{x_0} = \left[\frac{d^2\varepsilon(g(\psi))}{d\psi^2}\right]_{\psi=0}, \tag{2.3}$$

for a change in gap due to a rotation, ψ. Equation 2.3 can be expanded to take into account this change in gap due to rotation as described by Equation 2.1 as follows,

$$k_{\psi\psi}^{x_0} = \frac{d}{d\psi}\left(\frac{d\varepsilon}{dg}\frac{dg}{d\psi}\right) = \frac{d\varepsilon}{dg}\frac{d^2g}{d\psi^2} + \frac{d^2\varepsilon}{dgd\psi}\frac{dg}{d\psi} = a\frac{d\varepsilon}{dg} + x_0\frac{d^2\varepsilon}{dgd\psi}, \tag{2.4}$$

where Equation 2.1 has been substituted in and differentiated with respect to ψ where necessary. Small angles of rotation have been assumed. The total rotational stiffness of the float due to the ith actuator of possibly several is then the sum of Equations 2.2 and 2.4:

$$K_{\psi\psi}^{i} = k_{\psi\psi} + a\frac{d\varepsilon}{dg} + x_0\frac{d^2\varepsilon}{dgd\psi}. \tag{2.5}$$

It can be seen that an actuator's contribution to the float's rotational stiffness depends not only on how its stored energy varies with the gap and tilt angle of the float, but also on its position with respect to the float and bearing.

For a superconducting coil magnetic actuator with a persistent current, the energy stored will depend on the inductance [27]. If an initial persistent current, I_0, is stored when the inductance is equal to L_0, then the flux,

$$\Phi_0 = I_0 L_0, \tag{2.6}$$

must be conserved. The inductance, $L(g)$, however will change with the gap between the coil and the inner surface of the float, and so the energy stored by the actuator can be defined as,

$$\varepsilon = \frac{\Phi_0^2}{2L(g)}. \tag{2.7}$$

If the coil is flat, and if the gap between it and the float is much smaller than the coil's radius, then it can be assumed that the inductance will be proportional to the volume of the gap [30]. The surface of the float can also be considered to extend sufficiently beyond the edges of the coil such that edge effects can be ignored. Then from Equation 2.1 and Figure 2.1, it is shown that for rotational motion alone the volume is proportional to the gap. It can then be assumed that

$$L(g) \approx \beta g(\psi), \tag{2.8}$$

where β is a constant. Substituting this into Equation 2.7 gives,

$$\varepsilon \approx \frac{\Phi_0^2}{2\beta g(\psi)}. \tag{2.9}$$

This implies for the case of superconducting magnetic actuators, that $k_{\psi\psi} = 0$ from Equation 2.2. Finally, substituting Equation 2.9 into Equation 2.5 yields:

$$K^i_{\psi\psi} = \frac{\Phi_0^2}{\beta g(\psi)^2}\left(\frac{x_0^2}{g(\psi)} - \frac{a}{2}\right). \tag{2.10}$$

This is the rotational stiffness due to one superconducting magnetic actuator, so summing over all such actuators applying forces to the float will give the total rotational stiffness of the float itself. This equation implies that there will be some distance from the central symmetry axis of the bearing in Figure 2.1 such that for an actuator placed there the terms in the brackets will cancel out, and hence it will impart zero rotational stiffness onto the float. This can be calculated to be,

$$x_0 = \sqrt{\frac{g(\psi)a}{2}}, \tag{2.11}$$

where ψ is nominally a small angle whose mean is zero. Alternatively, the rotational stiffness of the float could be adjusted in-situ by changing the persistent currents in the coils which would change the magnitude of the Φ_0 term.

In the case of the Superconducting Torsion Balance described in Chapter 3, there are 3 superconducting coil magnetic actuators on each side of a triangular prism shaped bearing (see Figure 3.3

in Chapter 3). One coil lies on the symmetry axis of each side where $x_0 = 0$, and the other 2 are equally spaced to either side of it, giving 9 coils in total. From Figure 2.1 and Equation 2.10, this implies that these centre coils impart a negative rotational stiffness on the float, while the side coils impart a positive rotational stiffness. The total rotational stiffness of the float can then be adjusted accordingly in-situ by changing the ratio of the persistent currents in the side coils to the centre coils. For a given ratio of currents, keeping the current in each coil the same as its respective equivalent on the other sides of the bearing mean the change in the forces applied to the float from the coils should cancel out. The float itself is levitated by a separate superconducting coil on the top surface of the bearing. Possible effects such as trapped flux pinning the levitated float, which would increase its rotational stiffness, have been ignored in this analysis. The details of these coils, the bearing and the float are given in Section 3.1.1 of Chapter 3. The approach described here is taken to derive a term for the rotational stiffness for the float used in the Air Bearing experiment described in Chapter 5. The difference in that application being the use of room temperature coil-magnet actuators to control the float instead of superconducting magnetic ones and so the material differences between the types of actuators and how they function are taken into account there.

2.2 Centre-of-Buoyancy Tuning

In the same way that external actuators can be used to tune in-situ the rotational stiffness of a levitated object, or float, they can also be used simultaneously to tune in-situ the float's centre-of-buoyancy to lie at its centre-of-mass. The centre-of-mass is the point where inertial forces act, whereas the centre-of-buoyancy is the location of the resultant of the forces that are applied to levitate the float and control its position. Alternatively, starting from some equilibrium position, if the float is slightly displaced it will experience a restoring force due to a combination of the actuators. The point through which this force acts we refer to as the centre-of-buoyancy. In the general case the centre-of-mass will not lie at the centre-of-buoyancy due to manufacturing imperfections and so horizontal accelerations and tilts will couple to the rotational mode of the

device [29].

The coupling of horizontal accelerations into the rotational mode and how to circumvent this is a long-standing problem for torsion balances. In [31] the motion of a simplified torsion balance model was analysed by considering the Lagrangian of the system. It was shown that a horizontal acceleration, due to seismic ground vibrations for example, would cause a simple pendulum oscillation of the torsion balance. If, however, the direction of the ground displacement was not exactly perpendicular to the balance arm length of the torsion balance, then the torsion balance would attempt to align itself to this position. This is a result of the balance wanting to minimise its moment of inertia and kinetic energy about the rotation axis, and results in a coupling of horizontal accelerations into the rotational mode.

Ways of mitigating against this coupling are detailed in [32], where torsion balances used in gradiometers can take advantage of specific design choices of geometries of the torsion balance beams to maximise or minimise their spherical multipole moments to create insensitivities to horizontal accelerations. Also, in these set-ups differential torsion balances, consisting of two torsion balances with a common axis giving a differential measurement, can be used to reject some of the common mode noise associated with seismic vibrations. While these methods are possible for balances utilised for measuring gravity gradients over geophysical scales, they cannot be used for torsion balances sensitive to weak forces at scales less than 1 mm. The method presented here, however, is applicable to torsion balances with fibres of zero length for short-range force measurements.

Consider a float, like that described in Section 2.1, that is levitated and is controlled in the 2-dimensional plane perpendicular to the Earth's gravity by external actuators, as shown in Figure 2.2 [27]. Here the actuators are represented by springs, but these, as well as the geometry of the float and the entire system, could be different. The centre-of-mass and centre-of-buoyancy, as well as the position of the centre-of-buoyancy relative to the centre-of-mass, $(\Delta x, \Delta y)$, are shown to highlight how horizontal accelerations and tilts can introduce a torque, Γ_z, to the float around the z-axis which would be parallel to the Earth's gravity. The difference in position between the centre-of-buoyancy and centre-of-mass has been exaggerated here, a well manufactured float would

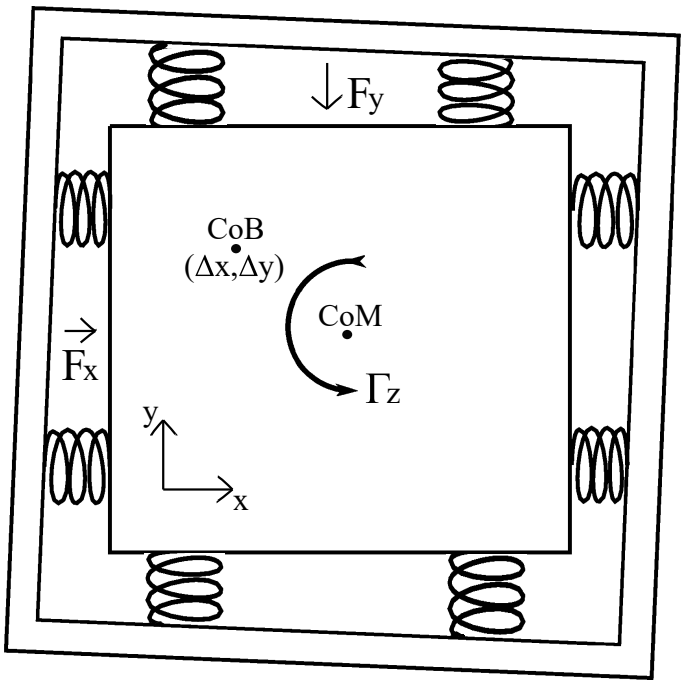

Figure 2.2: A diagram showing a levitated float, whose motion in the 2-dimensional plane perpendicular to the Earth's gravity is controlled by external actuators represented here by springs. The centre-of-mass (CoM) and centre-of-buoyancy (CoB) are also shown to highlight how horizontal accelerations and tilts can introduce a torque, Γ_z, to the float. This diagram is taken and adapted from the paper by Speake and Collins [27].

make this difference minimal. To completely decouple horizontal accelerations due to seismic noise and tilt from the float's rotational mode however, the difference should nominally be made zero.

To do this, we can take into account the equations of motion of the float in the horizontal plane where there are 3 degrees of freedom; ξ and η linear motion in the x and y axes respectively from Figure 2.2, and ψ rotational motion around the z-axis which is perpendicular to the page. For these degrees of freedom the full general equation of motion is given by [27],

$$\underline{F} = -\underline{\underline{K}} \cdot \underline{\Delta} \implies \begin{pmatrix} F_x \\ F_y \\ \Gamma_z \end{pmatrix} = - \begin{pmatrix} K_{\xi\xi} & K_{\xi\eta} & K_{\xi\psi} \\ K_{\xi\eta} & K_{\eta\eta} & K_{\eta\psi} \\ K_{\xi\psi} & K_{\eta\psi} & K_{\psi\psi} \end{pmatrix} \cdot \begin{pmatrix} \xi \\ \eta \\ \psi \end{pmatrix}, \tag{2.12}$$

where the forces and torque F_x, F_y and Γ_z are those defined in Figure 2.2, and the K terms refer to the stiffness of the float in the respective degrees of freedom and of the various cross-couplings between those degrees of freedom. Based on the components of the forces and torque and of the separation of the centre-of-buoyancy with respect to the centre-of-mass, $(\Delta x, \Delta y)$, in Figure 2.2, the torque acting on the float can be defined as,

$$\Gamma_z = \Delta x F_y - \Delta y F_x. \tag{2.13}$$

Substituting this into Equation 2.12 and solving for ψ yields,

$$\psi = -\left(K_{31}^{-1} - \Delta y K_{33}^{-1}\right) F_x - \left(K_{32}^{-1} + \Delta x K_{33}^{-1}\right) F_y, \tag{2.14}$$

where the K terms now refer to the elements of the inverse matrix of $\underline{\underline{K}}$. We are interested in the condition of the stiffnesses which results in no rotation of the float, $\psi = 0$, and so this combined with finding the inverse matrix of $\underline{\underline{K}}$ gives,

$$\begin{aligned} 0 = &\left(K_{\eta\eta}K_{\xi\psi} - K_{\xi\eta}K_{\eta\psi} - \Delta y\left(K_{\xi\eta}^2 - K_{\xi\xi}K_{\eta\eta}\right)\right) F_x \\ &+ \left(K_{\xi\xi}K_{\eta\psi} - K_{\xi\eta}K_{\xi\psi} + \Delta x\left(K_{\xi\eta}^2 - K_{\xi\xi}K_{\eta\eta}\right)\right) F_y. \end{aligned} \tag{2.15}$$

We are also interested in the condition where $\psi = 0$ regardless of the magnitudes of the horizontal forces acting on the float. This gives two equations, one for each coordinate in the 2-dimensional

horizontal plane, which the stiffnesses of the float have to satisfy in order to move the centre-of-buoyancy to lie at the centre-of-mass and therefore decouple these horizontal forces from the rotational mode:

$$\Delta x = \frac{K_{\xi\xi}K_{\eta\psi} - K_{\xi\eta}K_{\xi\psi}}{K_{\xi\xi}K_{\eta\eta} - K_{\xi\eta}^2}, \tag{2.16}$$

and

$$\Delta y = \frac{K_{\eta\eta}K_{\xi\psi} - K_{\xi\eta}K_{\eta\psi}}{K_{\xi\eta}^2 - K_{\xi\xi}K_{\eta\eta}}. \tag{2.17}$$

Through the use of reasonable manufacturing tolerances for superconducting actuators (typically sub-μm tolerances), the cross-coupling terms can be made much smaller than the non-cross-coupled stiffness terms [27], which simplifies these equation to:

$$\Delta x \approx \frac{K_{\eta\psi}}{K_{\eta\eta}}, \tag{2.18}$$

and

$$\Delta y \approx -\frac{K_{\xi\psi}}{K_{\xi\xi}}. \tag{2.19}$$

These equations imply that in principle it should be possible to alter the stiffness of the actuators in order to tune in-situ the centre-of-buoyancy to lie at the float's centre-of-mass, and hence decouple tilt and horizontal accelerations due to seismic noise from its rotational mode.

In the case of the Superconducting Torsion Balance, where the energy stored, ε, by each superconducting magnetic actuator is given by Equation 2.9, the stiffness terms in Equations 2.18 and 2.19 can be derived. The stiffnesses on the denominators of these equations are simply the linear stiffnesses of the actuators in the horizontal plane. As described in Section 2.1, and from Equations 2.1 and 2.3, it can be seen these linear stiffnesses depend on the change in gap, $g(\psi)$, in a given axes. We can define therefore, say for the y-axis in Figure 2.2, the linear stiffness in that axis from the ith actuator as,

$$K_{\eta\eta}^i = \left[\frac{d^2\varepsilon(g_\eta(\psi))}{dg_\eta(\psi)^2}\right]_{\psi=0} = \frac{\Phi_0^2}{\beta g_\eta(\psi)^3}. \tag{2.20}$$

The stiffnesses on the numerators of Equations 2.18 and 2.19 represent the cross-coupling between the degrees of freedom, and in the case of the y-axis in Figure 2.2 again, the cross coupling term

from the ith actuator can be defined as,

$$K^i_{\eta\psi} = \left[\frac{d^2\varepsilon(g_\eta(\psi))}{d\psi dg_\eta(\psi)}\right]_{\psi=0} = \frac{x_0\Phi_0^2}{\beta g_\eta(\psi)^3}, \tag{2.21}$$

where x_0 is once again the distance of the actuator from the symmetry axis in the x-axis as in Figure 2.1. Therefore, in the case of tuning the centre-of-buoyancy along the x-axis, we sum over the contributions of each actuator acting perpendicular to that axis giving,

$$\Delta x \approx \frac{\sum_{i=1}^n K^i_{\eta\psi}}{\sum_{i=1}^n K^i_{\eta\eta}} = \frac{\sum_{i=1}^n x_i\Phi_i^2}{\sum_{i=1}^n \Phi_i^2}, \tag{2.22}$$

where we have n actuators in total applicable to that axis (the 0 subscripts have been dropped for clarity). The superconducting coil that lies on the symmetry axis of each side of the bearing in the experiment, as described in Section 2.1 where $x_0 = 0$, will not alter the centre-of-buoyancy. The other 2 coils spaced to either side of it, because of their positions of x_0 relative to the symmetry axis, will have either a positive or negative contribution to Δx. Therefore Δx can be adjusted accordingly in-situ by changing the ratio of the persistent currents between the side coils. Keeping the total overall current in side coils the same as the ratio between them changes means there should be no overall change in force applied to float from the coils and the rotational stiffness should not be altered. This treatment can be applied to the other axis in the horizontal plane with an appropriate change in subscripts. As with the rotational stiffness tuning, the approach described here is taken to derive a term for the centre-of-buoyancy tuning for the float used in the Air Bearing experiment described in Chapter 5, with its room temperature coil-magnet actuators.

This analysis of the centre-of-buoyancy tuning ignores cross-coupling effects between the coils which is acceptable assuming reasonable geometries of the actuators and also the fact that in the case of the Superconducting Torsion Balance, each actuator is closer in distance to the surface of the float that it acts on than it is to its adjacent actuator by a factor of at least 10. Certain techniques can also be employed to avoid magnetic field leakage between the coils; details of one method which was used on the Superconducting Torsion Balance is given in Sections 3.1 and 3.3 of Chapter 3.

Chapter 3

The Superconducting Torsion Balance

The natural scientist must be a modern materialist, a conscious adherent of the materialism represented by Marx, i.e., he must be a dialectical materialist.

Vladimir Lenin

In this chapter I give an overview of the Superconducting Torsion Balance. The bulk of this device was constructed prior to my work, with the initial description of the experiment given in the conference proceedings 'Testing the Inverse Square Law of Gravitation at Short Range with a Superconducting Torsion Balance' [33]. I give a detailed description of its main components, expected signal and noise sources in Section 3.1. In Section 3.2 I describe my contribution to the experiment apparatus. In Section 3.3 I describe the finite element analysis work I performed to demonstrate the feasibility of levitating the torsion balance's test mass. Section 3.4 gives a brief description of the current status of the Superconducting Torsion Balance.

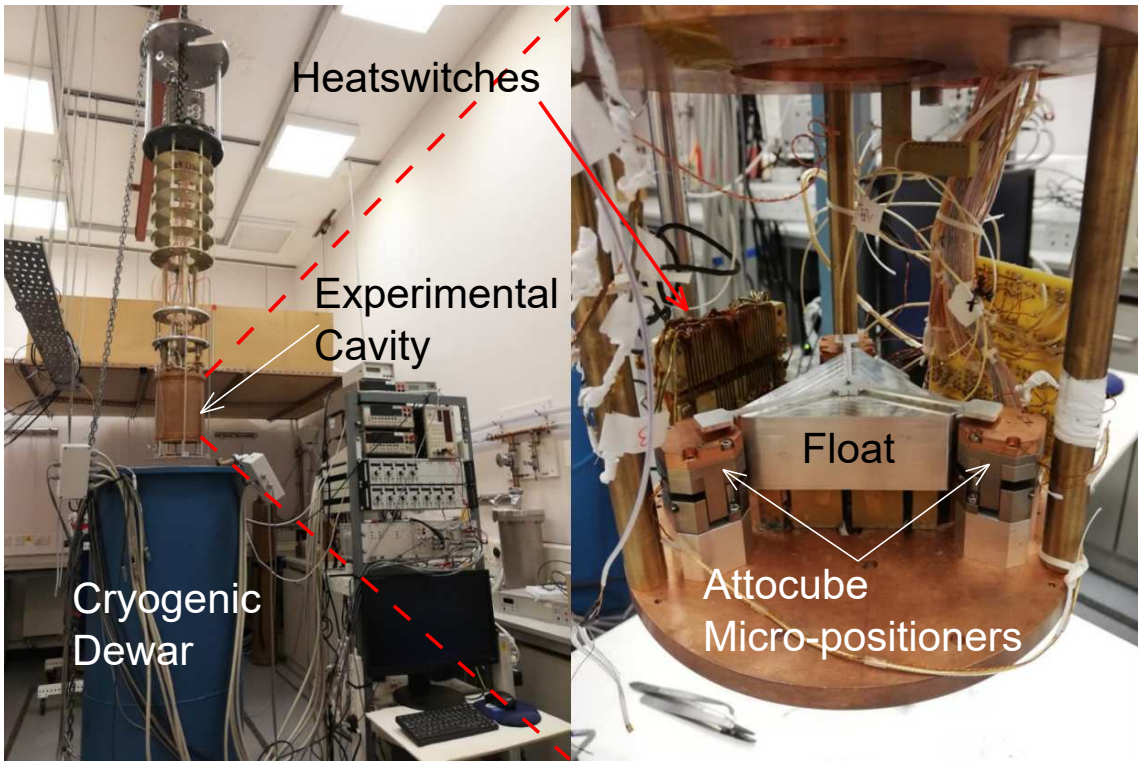

Figure 3.1: A photograph of the full experiment in its current status, with the major components labelled.

3.1 Overview

The Superconducting Torsion Balance was designed to measure the inverse square law of gravity down to mass separations of the order of 10 μm [34]. A photograph showing the full experimental setup in its current state as a reference, which will be expanded upon by other images later in the chapter, is given in Figure 3.1. This experiment was based on previous work on developing superconducting levitating torsion balances, called the Superconducting Spherical Torsion Balances, which were designed to perform weak-force measurements [10, 35, 36, 37, 38]. These previous versions were used to successfully put new constraints on short-range forces coupling mass to intrinsic spin [39]. The new Superconducting Torsion Balance was based on the same principle of a superconducting levitation suspension of the torsion bob due to the Meissner effect in lieu of a traditional torsion fibre, with the interactions of the various pieces of hardware that made up the experiment controlled through custom made LabVIEW software. It was a cryogenic experiment;

the process for cooling it down to 4.2 K from room temperature is described in Appendix A. There were, however, several key differences in the experimental design between the older and new versions. These differences were implemented in order to increase the stiffness of the torsion bob with respect to the tilting and translational degrees-of-freedom, which would allow for shorter ranged measurements at smaller mass separations. A change of design to a planar geometry in the torsion balance was also planned as a way to increase the gravitational signal strength for a given setup.

3.1.1 Superconducting Bearing and Float

The first key design change was the move away from a spherically symmetric suspended mass and superconducting bearing to levitate it. This was to take advantage of the in-situ rotational stiffness and centre-of-buoyancy tuning detailed in Chapter 2. Also, a planar geometry of source and test masses would allow for a better signal-to-noise ratio compared to spherical masses. The bearing and the float, which was the levitated torsion bob that would hold the test mass, were redesigned to be equilateral triangular prism shaped. A photograph of the float is shown in Figure 3.2, and a photograph of the bearing is shown in Figure 3.3 [40]. The bearing contained the superconducting lead coils which through the use of persistent currents and the Meissner effect would control the dynamics of the float in the relevant degrees of freedom. The process of storing these persistent currents is described in Section 3.2.2.

The bearing held 10 coils in total: 3 circular coils on each side of the bearing and 1 large triangular coil on the bearing's top surface. These coils were hand-wound with 250 μm diameter lead wire. The coild holders were made of anodised aluminium. The coil on the top surface was split into three separate kite-shaped sections in order to maximise the number of windings to surface area. Each kite-shaped section contained 29 windings in total and the total length across one side of the bearing was 55 mm. On each side of the bearing there were 3 coils, one larger circular centre coil and two smaller circular coils either side of it with 28 and 20 windings, and diameters of 20 mm and 14 mm, respectively. All the coils featured an outer winding which was wired in the opposite direction to the inner windings to minimise magnetic field leakage. Figure 3.4 [40] shows a close-up

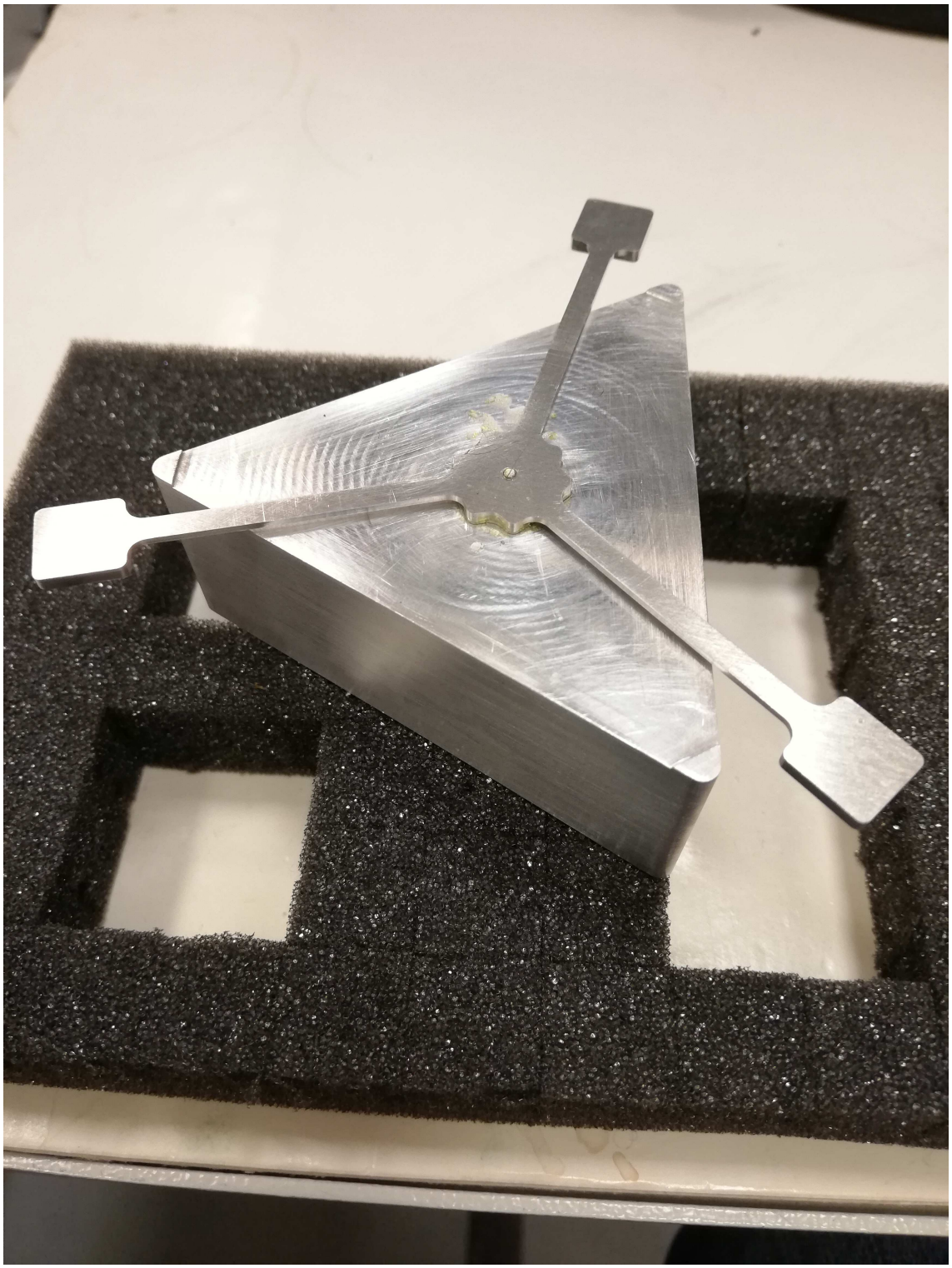

Figure 3.2: This is the float used in the experiment. This was the object that would be levitated via the Meissner effect using the superconducting lead coils in the bearing, and which would support the test mass which would be attached to its top surface. The three-armed attachment to the top of the float is explained in Section 3.2.1.

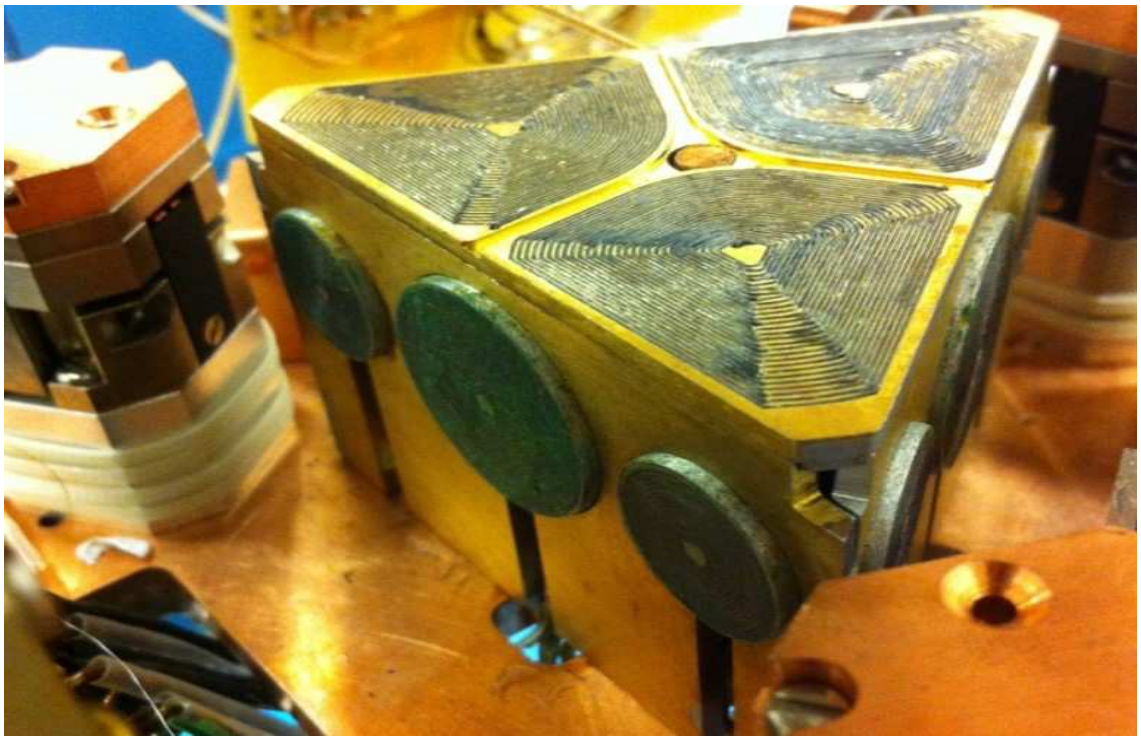

Figure 3.3: This is the bearing that held the superconducting lead coils which, through the use of persistent currents, would levitate and control the float through the Meissner effect. The photograph was taken by Collins [40].

Figure 3.4: A close-up of one of the larger bearing centre side coils with a pound coin to give a sense of scale. The photograph was taken by Collins [40].

of one of the larger side coils with a pound coin to give an idea of scale.

The float was made of aluminium, with a mass of approximately 30 g which excludes the test mass that would be attached to its top surface. Each surface of the float was 1 mm thick, and the side panels had dimensions of 68.4 mm by 28 mm. In order to use the Meissner effect to levitate it and control its dynamics, however, the float itself had to include some superconducting elements. The inside of the float was lined with 25 μm thick lead foil that was held in place by a thin layer of cryogenic and high vacuum compatible Apiezon N Grease. This is shown in Figure 3.5. The three-armed attachment to the top of the float is explained in Section 3.2.1. A diagram showcasing how the coils in the bearing could control the float dynamics is shown in Figure 3.6 [41]. The top coil in the bearing provided the magnetic pressure and hence a lift force to levitate the float, the physics of which is described in Section 3.3. The side coils could be used to provide a transverse stiffness to the float in the horizontal plane of the laboratory in order to keep it stable. As detailed in Chapter 2, they could also be used to tune the rotational stiffness and centre-of-buoyancy of the float in-situ. This was done by changing the ratio of the strength of these actuators by changing the ratio of the persistent currents between the large and smaller circular coils on each side of the bearing. This was the main reason for the geometry of the float and bearing design. The float was lowered into position above the bearing, and hence its height could be monitored, using three Attocube micro-positioners and the float's three-armed attachment. The details of this are described in section 3.2.1. The mean distance between the bearing coils and the inner surfaces of the float was typically 100 μm to 150 μm.

The rotational displacement of the float was measured through the use of a differential capacitive sensor which consisted of two capacitive electrodes forming a transducer bridge, positioned at each end of one side of the float. The details of its design, specifically its pre-amplifier layout and sensitivity, are given in Chapter 4. The mean separation between the float's outer surface and the capacitive electrodes was 1 mm. A photograph of the capacitive electrodes in position next to the float is shown in Figure 3.7. The dimensions of the front face of each electrode was 25 mm by 15 mm, and the separation between their centres was 40 mm. The float would need to be grounded

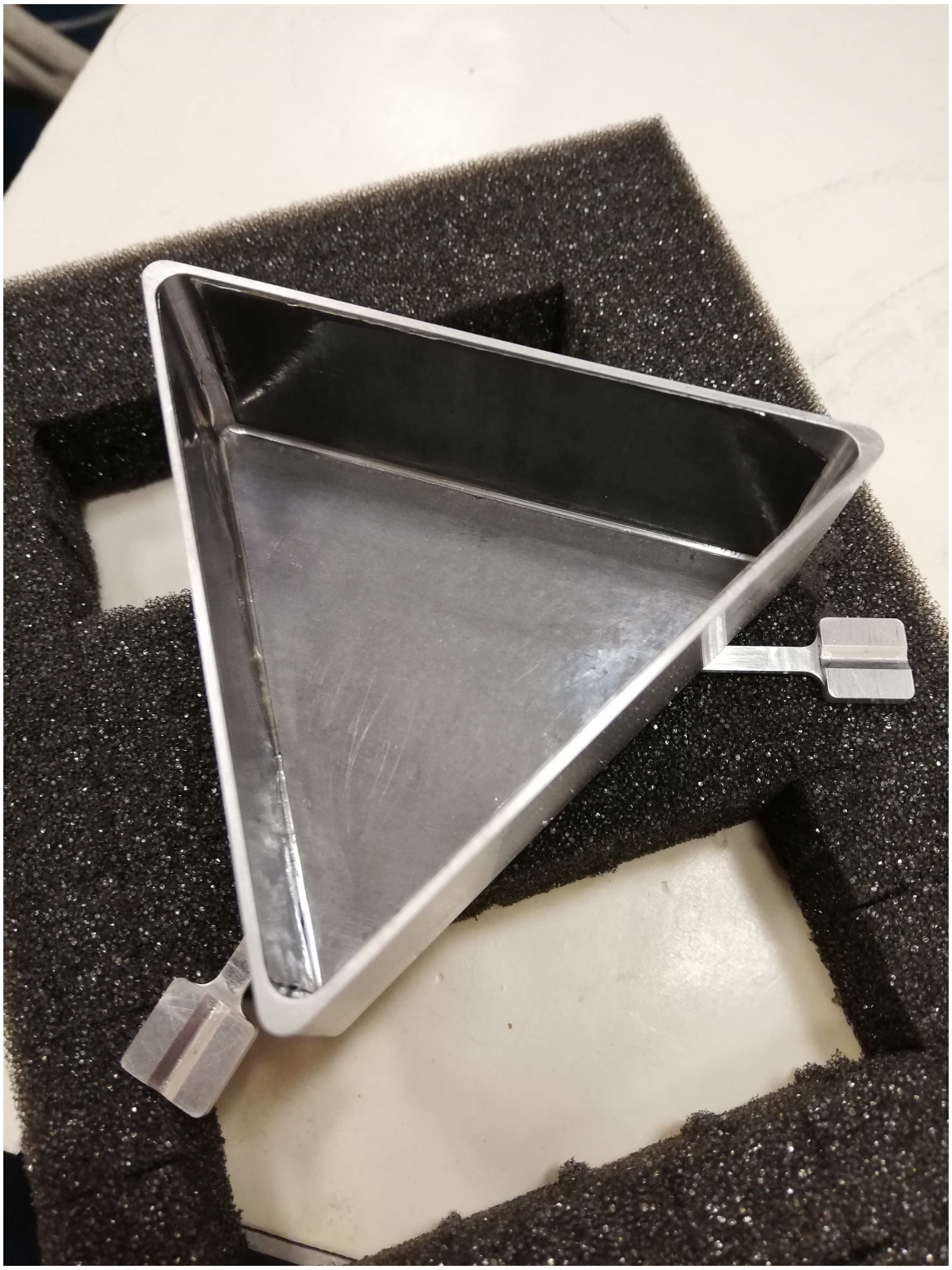

Figure 3.5: A photograph of the interior of the float showing the lead foil lining which was needed to produce the Meissner effect along with the superconducting coils in the bearing, in order to control its dynamics.

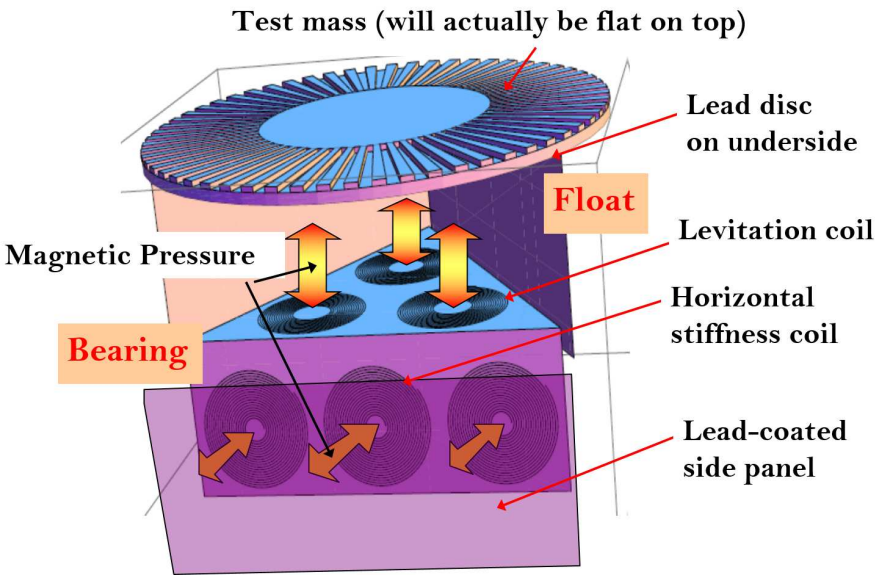

Figure 3.6: A graphic diagram showing how the superconducting coils can control the dynamics of the lead-lined float through the use of persistent currents and the Meissner effect. The graphic was designed by Collins [41]. The test mass design on top of the float in this graphic is emphasised here, where it is not featured in Figure 3.2.

for this to work, and was through the use of a 50 μm diameter gold wire which was electrically connected to it. This wire was light and flexible enough to have a negligible effect on its motion.

3.1.2 Source and Test Masses

The source and test masses that are to be used in the Superconducting Torsion Balance have been designed to have a disk geometry. This allows a maximum amount of mass to be at the minimum separation distance between the source and test masses. Hence, it provides the maximum gravitational signal. The source and test masses are designed to have diameters of (80.00 ± 0.15) mm and masses of 2-3 g. The float and test mass will have a combined mass of 31.3 g. Both the source and test masses will have an initial base layer of silicon substrate with a thickness of (0.700 ± 0.025) mm. Silicon will be used as the base layer as it is unlikely to mix with or react to the other materials in the masses. The test mass will be positioned on top of the float described in Section 3.1.1, with its top surface parallel to the horizontal plane of laboratory. The source

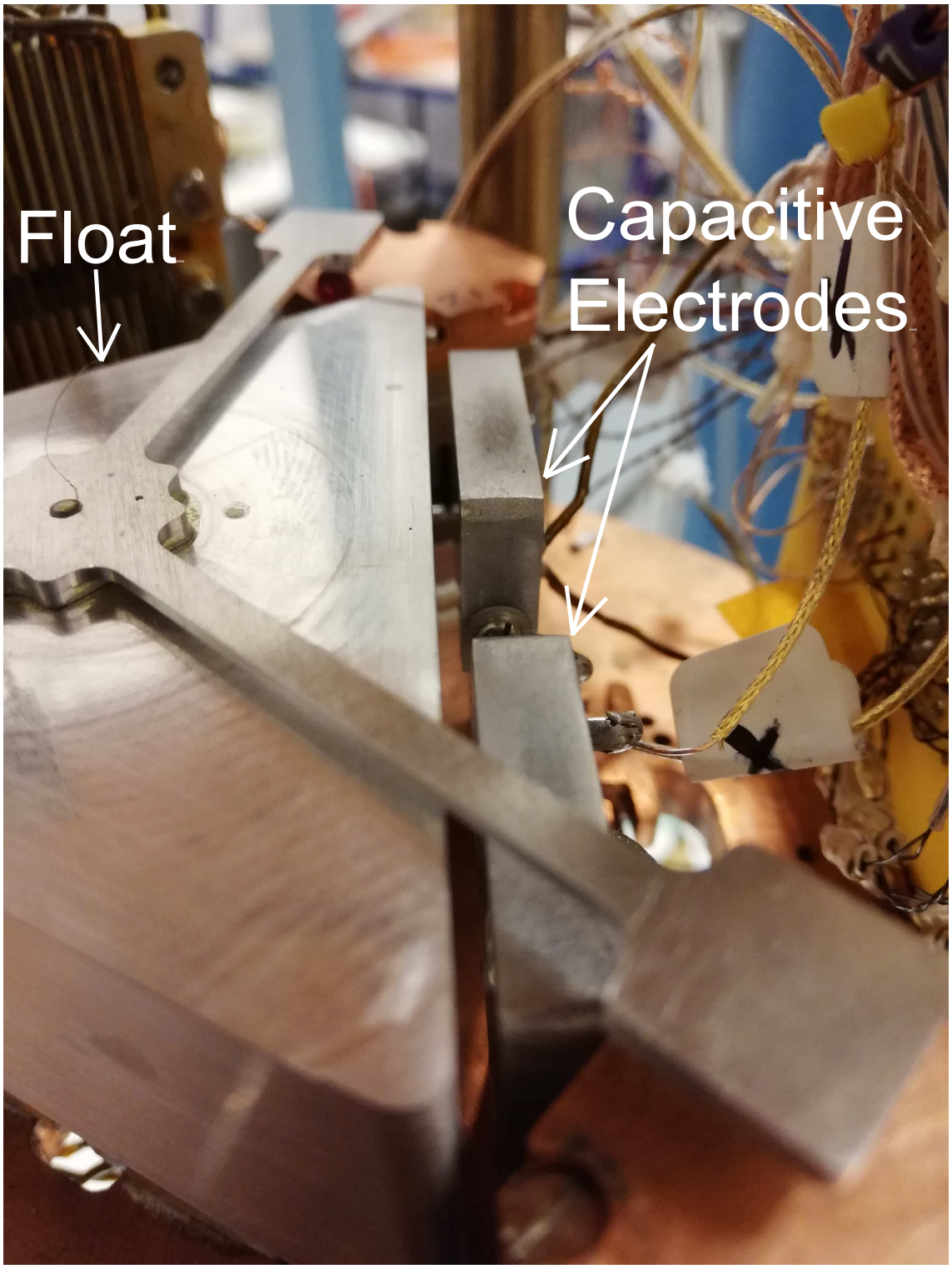

Figure 3.7: A photograph of the float and the capacitive electrodes used to measure its rotational displacement during the experiment.

mass, also with its surface parallel to the horizontal plane but with it's top surface facing down toward the test mass, will be held in place above the test mass and float with an Attocube micro-positioner. The Attocube could be used to lower the source mass, with capacitive measurements between the two masses allowing their separation and relative tilt to be determined. This Attocube could also rotate the source mass, allowing its rotational position to be modulated and hence in an experiment induce a corresponding gravitational torque signal on the levitated test mass. It and the float would then be rotationally displaced accordingly. Figure 3.8 shows an Autodesk Inventor design of the full setup of the experiment with the float, source and test masses in place.

The important component of both masses is the foil of material on their base silicon substrates which after processing will make up their top surfaces. What follows is the foil's manufacturing process, which is demonstrated in Figure 3.9. First, the silicon will be coated with a 5 nm barrier layer of tungsten-titanium to prevent interdiffusion with the material on top of it. A 100 nm layer of gold will then be thermally deposited on top of this, followed by a 1 μm layer that will be electro-deposited. Then a patterned photoresist coating will be placed on top of this gold layer. This will consist of a radial spoke pattern of stripes, with an average pitch of 92 μm and 2048 pairs of stripes in total [42]. Gold will then be electro-deposited on top of this pattern to a depth of 10 μm. Another 5 nm barrier layer of tungsten-titanium will then be used to coat the gold to prevent interdiffusion with the material added to it next. Copper will then be electro-deposited into the empty spokes in the pattern, filling these gaps and then adding an extra 5 μm layer on top of the whole surface. This will form the 'back layer' or bottom surface of the finished masses. Finally, the silicon substrate on the 'front layer' or top surface will be etched away with 40% potassium hydroxide solution at approximately 353 K. The titanium-tungsten layer that was 'below' this will then be removed with a 5% ammonium-hydrogen difluoride solution at room temperature. This will leave the $\sim$1 μm gold layer on 'top' of the radial spoke pattern of gold and copper stripes as the top surface of both masses. This extra 1 μm top layer will act as a shield to electrostatic forces between the disks and it is this radial spoke pattern that will provide the gravitational torque signal due to the change in density of the material across the disks. Gold and copper were chosen

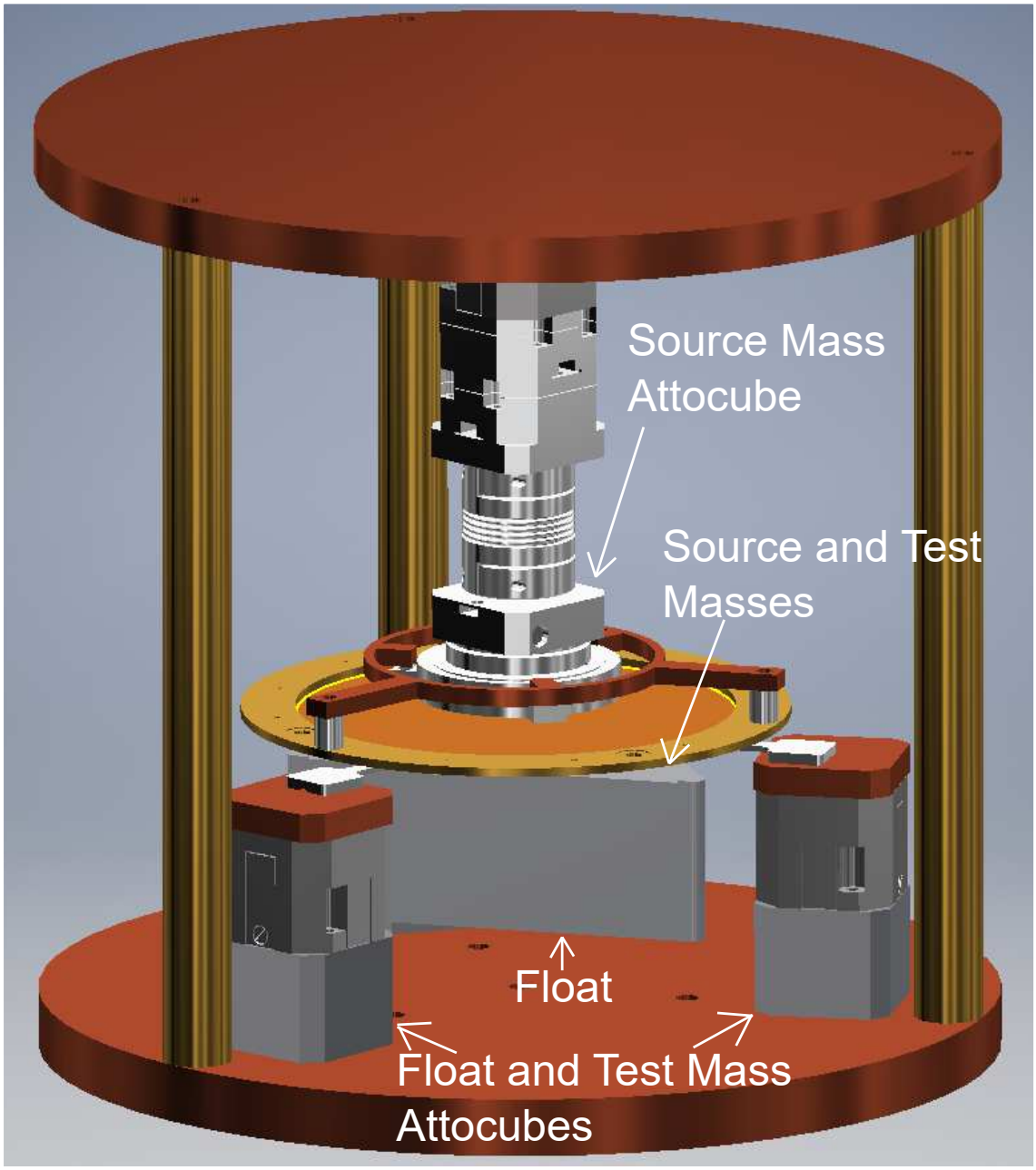

Figure 3.8: A graphic of the design of the full experimental setup with the float, source and test masses in place.

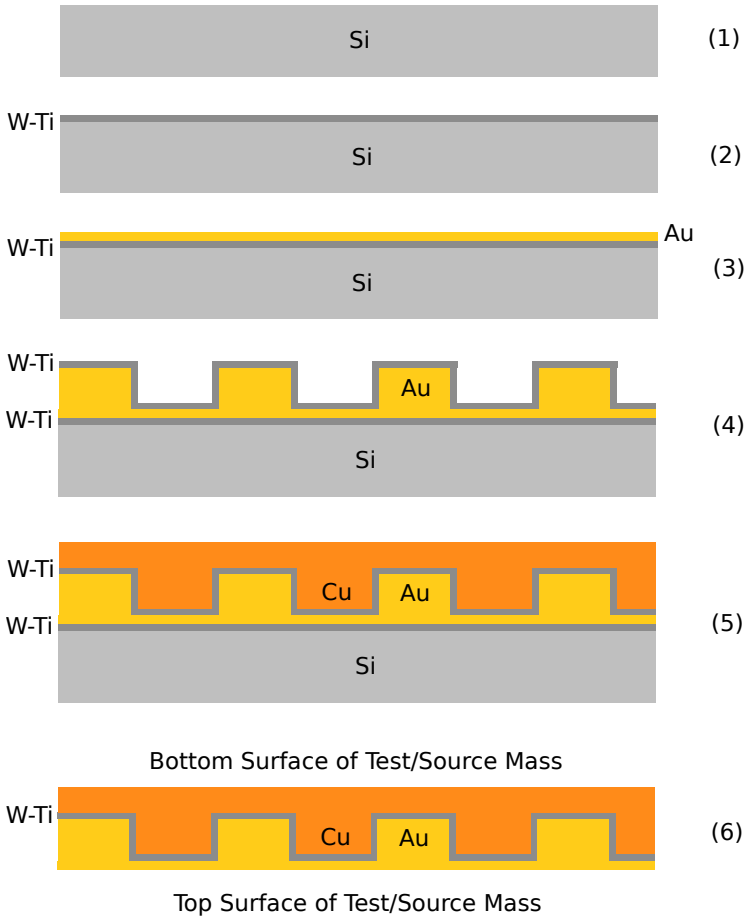

Figure 3.9: A graphic of the manufacturing process of the top surface foil of the source and test masses; not drawn to scale. (1) The masses will have an initial base layer of silicon substrate with a thickness of 0.700 mm. (2) The silicon will then be coated with a 5 nm barrier layer of tungsten-titanium to prevent interdiffusion with the material on top of it. (3) A 100 nm layer of gold will then be thermally deposited on top of this, followed by a 1 μm layer that will be electro-deposited. (4) Then a radial spoke pattern of stripes of photoresist coating will be placed on top of this gold layer, and gold will then be electro-deposited on top of this pattern to a depth of 10 μm. Another 5 nm barrier layer of tungsten-titanium will then be used to coat the gold, again to prevent interdiffusion. (5) Copper will then be electro-deposited into the empty spokes in the pattern, filling these gaps and then adding an extra 5 μm layer on top of the whole surface. (6) Finally, the silicon substrate and first titanium-tungsten layer will be etched away by chemical solutions, leaving the gold layer on the spoke pattern as the 'top' surface of the mass foils.

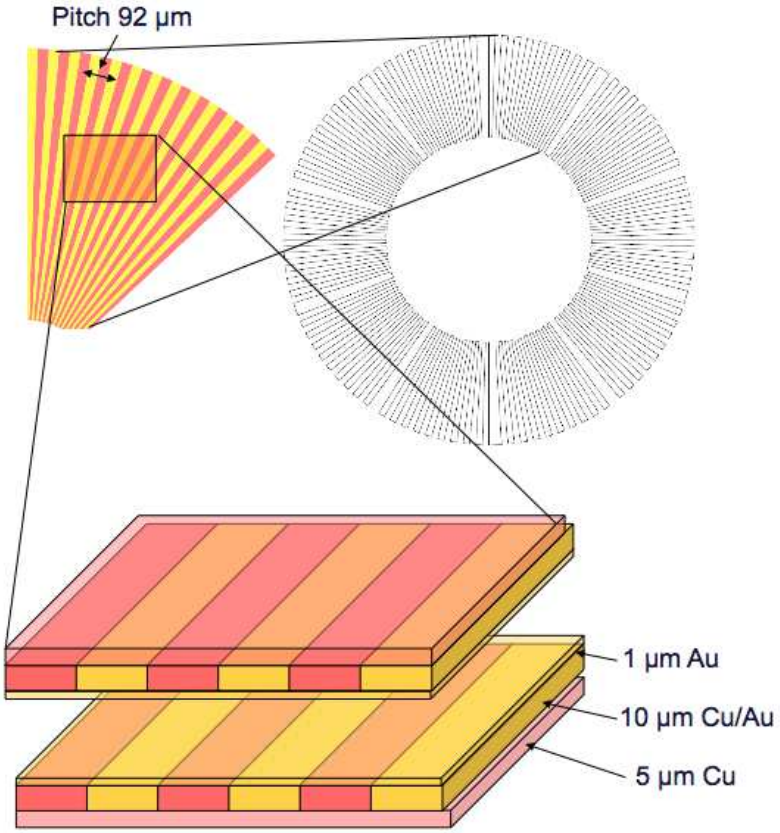

Figure 3.10: A graphic diagram showing the top layers of foil on the test and sources masses and how they will face each other. The graphic was designed by Collins [41]. This includes their thicknesses and the average pitch of the foil with the radial spoke pattern of 2048 pairs of gold and copper stripes.

as a balance between as large a density contrast and as well-matched a thermal contraction at 4.2 K as possible [33]. A graphic diagram highlighting this design and how the test and source masses would face each other is shown in Figure 3.10 [41]. The number and width of the spokes was critical for optimising the masses, as the greater the number of spokes the greater the gravitational torque induced on the test mass due to the greater amount of modulation of the different densities of material. However, the width of the spokes had to be greater than 2π times the target source and test mass separation ($\sim$14 μm) otherwise the gravitational torque would start to average out over the circumference of the disks. This led to the current design being used as it was a compromise between these two characteristics.

Both masses required a flatness across their entire surfaces of $\pm$ 1.5 μm at the most. A process for flattening the foils and keeping them taut is described in detail in [43, 44]. A summation of this process and the recent best flatness measurements of source mass test foils using this procedure are given here. The initial copper foil was cut using a computer aided water jet cutter. Once the final foil was prepared, it was glued onto a raised lip at the inner radius of an annulus shaped object called the source mass ring using a DotMaster machine, which could apply a uniform pattern of glue. The source mass ring was made of phosphor bronze with an outer diameter of 113 mm, an inner diameter of 93 mm, thickness 1.5 mm and a 2 mm wide raised inner lip creating a gluing area for the foil with an additional thickness of 0.5 mm. There were 12 evenly spaced screw holes across the circumference of the annulus. Prior to this gluing, the source mass ring was screwed on top of another annulus of the same outer diameter called the torsion jig. This was made of aluminium, with an inner diameter of 105.5 mm, a thickness of 5.5 mm and a 1 mm wide raised outer lip with an additional thickness of 0.5 mm. There were also 12 equally spaces screw holes in the torsion jig to match the source mass ring. Due to the position of the outer raised lip on the torsion jig, screwing the source mass ring in place caused it to tilt inwards toward the centre of the annuli. Once screwed in place the foil would be glued to the source mass ring's inner raised lip. The screws would then be removed, doing so would cause the source mass ring to tilt outward again, causing the foil to pulled taut around its entire circumference causing it to flatten. When screwing the source mass ring in place on the torsion jig, a torque driver was used to ensure equal force was applied to each screw and that the tension was constant across the surface of the foil. A typical torque used on the screws was 0.8 N·m and typically a tension of 6 N would be applied across a foil in this process [43, 44]. The glue used was Araldite 8545-1, and its associated hardener, as this was compatible for use at cryogenic temperatures, and the glued foils would be left to set for 24 hours on the source mass ring before loosening the ring from the torsion jig. A diagram showing this procedure is shown in Figure 3.11. Figure 3.12 shows a photograph of the torsion jig and a source mass ring with a test source mass foil in place after being glued and pulled taut using the aforementioned procedure.

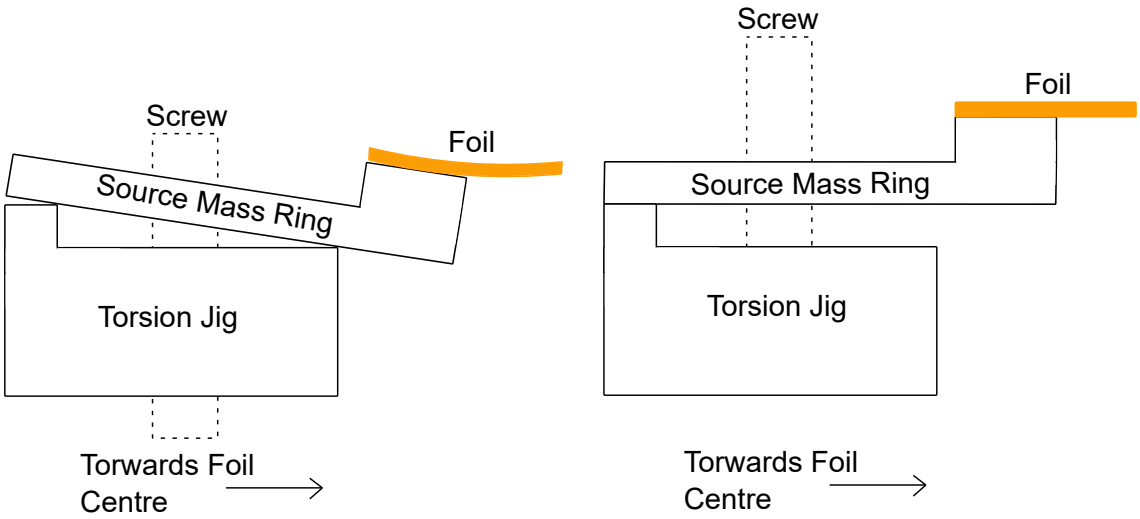

Figure 3.11: A graphic showing how, on the left side of the figure, the source mass ring can be screwed into the torsion jig to twist its inner radius toward the centre of the annuli. The source foil could then be glued to the source mass ring's inner raised lip. The right side of the figure shows how, once the source mass ring was unscrewed from the torsion jig, the foil would be pulled taut around its entire circumference causing it to flatten. Not drawn to scale.

The latest test foils flattened in [43, 44] achieved a flatness of $\pm$ 24 μm. This measurement was done using a SmartScope scanner. The requirement is $\pm$ 1.5 μm and so this needs to be improved by over an order of magnitude. This could be done through more analysis of the warping of the source mass rings after they are stressed by tightening and then releasing them with the screws on the torsion jig, by looking at alternative methods of gluing the foils to the source mass rings and by increasing the tension the foils are subjected to [43, 44].

3.1.3 Expected Signals and Noise Sources

Gravitational Torque Signal

Based on the geometries of the source and test masses that have been designed, and assuming the requirements of the flatness and the separation distance of the masses are achieved, the expected gravitational torque signal on the levitated test mass, from both the Newtonian potential as well as from a new Yukawa potential as described by Equation 1.1 in Section 1.2 of Chapter 1, can

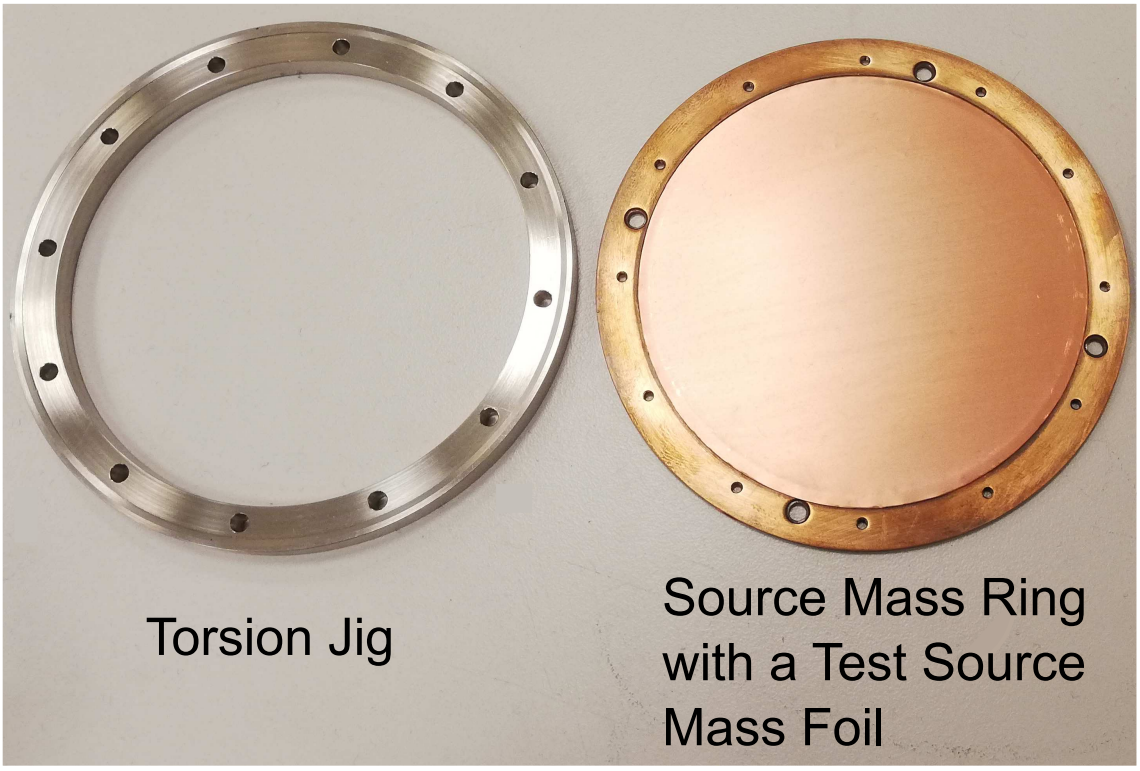

Figure 3.12: A photograph of the torsion jig and a source mass ring with a test source mass foil in place after being glued and pulled taut.

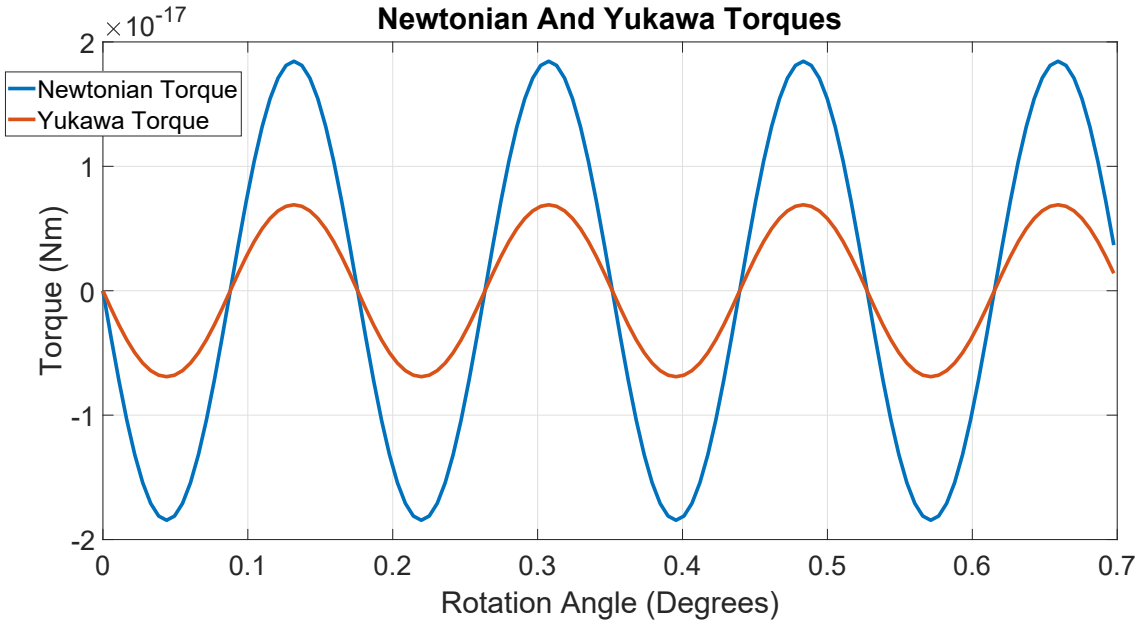

Figure 3.13: A graph of the modelled gravitational torque signal due to the Newtonian potential, as well as the Yukawa potential, on the levitated test mass due to the rotation of the source mass. This is assuming a mass separation of 15 μm and 2048 pairs of gold and copper stripes on the masses' radial spoke pattern with an average pitch of 92 μm. It is assumed, as stated in Section 1.2 of Chapter 1, that α and λ in Equation 1.1 are 1 and 14 μm respectively.

be modelled. Figure 3.13 shows the expected gravitational torque signal due to the Newtonian and Yukawa potentials on the levitated test mass due to the rotation of the source mass. This is assuming a mass separation of 15 μm and 2048 pairs of gold and copper stripes in the masses' radial spoke pattern with an average pitch of 92 μm, as described in Section 3.1.2. It is also assumed that α and λ, from Equation 1.1 in Section 1.2, are 1 and 14 μm respectively. It can be seen that the maximum Newtonian torque is 1.89×10^{-17} N·m. This is the minimum signal to which the Superconducting Torsion Balance must be sensitive to. The additional Yukawa potential gives a maximum torque of 0.65×10^{-17} N·m.

Torque Due to a Transverse Casimir Force

Although the foils in the test and source masses are designed to be flat at room temperature, and that gold and copper have similar thermal expansion coefficients; once cooled down to 4.2 K

the gold stripes would be 0.2 nm taller than the copper stripes due to this differential thermal expansion [33]. This modulation of the test and source mass separation across their surfaces would lead to a Casimir force that would act to align the taller gold stripes between the masses. This transverse Casimir force would lead to a torque on the levitated test mass which can be expressed as [33],

$$\Gamma_{Cas} = -\frac{\pi^3 \hbar c L A_c^2}{60 g_{\nu 0}^5} = -1.41 \times 10^{-21}\,(\mathrm{N}\cdot\mathrm{m})\,, \tag{3.1}$$

where A_c is the 0.2 nm height difference between the stripes, $g_{\nu 0}$ is the separation between the source and test masses which can be taken to be 15 μm and L is an effective area factor which takes into account the total length of the 2048 pairs of gold and copper stripes (each with a length of 4 cm) multiplied by the effective arm length of the strips of 2 cm to produce a torque. This gave a value of 1.64 m^2. The torque due to a transverse Casimir force calculated here is several orders of magnitude smaller than the Newtonian signal, and so is negligible.

Torque Due to Electrostatic Forces

Electrostatic forces due to the raised gold stripes in the masses would also produce a torque that would act to align the raised stripes, which can be described by [33],

$$\Gamma_{Elec} = -\frac{\epsilon_0 \pi L \Delta V^2 A_c^2}{g_{\nu 0}^3} = -5.41 \times 10^{-20}\,(\mathrm{N}\cdot\mathrm{m})\,, \tag{3.2}$$

where repeated symbols retain their previous definitions and ΔV is the potential difference between the source and test masses. A maximum variation between the masses of the order of 0.01 V for ΔV can be assumed [45]. Keeping the masses grounded reduces this difference significantly, with patch potentials being the main source of variation across the surfaces. Again, the torque due to a transverse electrostatic force is negligible compared to the Newtonian signal.

Torque Due to Contact Potentials

Contact potential differences, ΔV_{cp}, between the gold and copper stripes in the masses alone, without topological variations due to the differential thermal expansion between the materials, could lead to additional transverse forces. If ΔV_{cp} can be reduced to around 2 μV, the torque

produced by the voltage difference due to contact potentials is given by [33],

$$\Gamma_{cp} = -\frac{2\epsilon_0 \pi^2 L \Delta V_{cp}^2}{p \sinh\left(\frac{2\pi g_{\nu 0}}{p}\right)} = -1.03 \times 10^{-17}\,(\mathrm{N}\cdot\mathrm{m})\,, \tag{3.3}$$

where p is the average pitch of the gold and copper stripes, which was 92 μm. Without the 1 μm gold shield layer on the top surface of both masses, as described in Section 3.1.2, the torque due to contact potentials would be much larger, as ΔV_{cp} between different metals is of the order of 1 V. With the gold shield it would nominally be zero, but ultimately we need it to be less than 2 μV for the associated torque to be smaller than the Newtonian signal. Finally, there will be patch potentials but they should not be correlated with the spoke pattern and so they will induce some additional, but negligible, noise torque.

Torque Due to Magnetic Forces

Differences in the diamagnetic polarisation between the gold and copper stripes due to a constant magnetic field would produce a similar effect to the contact potentials and give a torque. This could be expressed as [33],

$$\Gamma_{Mag} = \frac{pL\Delta\chi^2 B^2}{\mu_0} e^{-\frac{2\pi g_{\nu 0}}{p}} \sinh^2\left(\frac{2\pi t}{p}\right) = -5.86 \times 10^{-18}\,(\mathrm{N}\cdot\mathrm{m})\,, \tag{3.4}$$

where $\Delta\chi$ is the difference between the magnetic susceptibilities of gold and copper which comes to -1$\times 10^{-5}$, B is the magnetic field of which 50 μT is a typical background level and t is the thickness of the gold and copper strips which, as stated in Section 3.1.2, is 10 μm. This torque is an order of magnitude smaller than the Newtonian signal, and could be made lower by shielding the experimental cavity from magnetic fields through the use of, for example, μ-metal [33].

Seismic Noise

The typical acceleration noise due to ground vibration, a_n, has been measured to be 0.5 $\mu\mathrm{m}\cdot\mathrm{s}^{-2}/\sqrt{\mathrm{Hz}}$ at the signal frequency of 0.1 Hz. If the mass, M, of the test mass is 31.3 g as mentioned in Section 3.1.2 (ignoring the float mass as this could change in future designs to be made as light as possible), and if the centre-of-mass to centre-of-buoyancy displacement of the test mass, x_{cb}, is of

the order 0.5 μm as a conservative estimate (the tuning of which is described in Chapter 2 and discussed at length in Chapter 5), then the torque noise of the test mass is

$$\Gamma_S = a_n M x_{cb} = 7.83 \times 10^{-15} \left(\frac{\mathrm{N \cdot m}}{\sqrt{\mathrm{Hz}}} \right). \tag{3.5}$$

Assuming a white seismic noise, with a days integration this becomes $\Gamma_{Seis} = 2.66 \times 10^{-17}$ N $\cdot$ m. This is approximately equal to the gravitational torque signal. This implies that a minimum integration time of a day is needed when taking measurements with the Superconducting Torsion Balance in order to achieve an acceptable signal-to-noise ratio. Of course this ignores complications due to microseismic variability over time, and so a days integration may be unrealistic in practice.

Summary

A summary of the modelled gravitational signal and the noise sources discussed in this section, and the magnitude of their associated torques acting on the test mass based on the parameters stated in their respective descriptions, is given in Table 3.1.

Table 3.1: A summary of the modelled gravitational signal, noise sources and the magnitudes of their calculated torques imparted onto the test mass, as described in this section.

Noise Source	Torque (N·m)
Transverse Casimir Force	1.41×10^{-21}
Electrostatic Forces	5.41×10^{-20}
Contact Potentials	1.03×10^{-17}
Magnetic Forces	5.86×10^{-18}
Seismic Noise	2.66×10^{-17}
Gravitational Signal	2.54×10^{-17}

Required Displacement Sensor Sensitivity

Taking the magnitudes of the torques in Table 3.1 into account, seismic noise will be the limiting factor, requiring measurements to be integrated for at least a day to achieve a signal-to-noise ratio

of 1. This noise value of 7.83×10^{-15} N $\cdot$ m/$\sqrt{\text{Hz}}$ from Equation 3.5 will then be the baseline sensitivity required for a displacement sensor for the float and test mass.

The moment of inertia, I, of the float and test mass based on their assumed overall mass and geometry has been calculated to be 2.51×10^{-5} kg$\cdot$m^2. If the target rotational period, P, is of the order 10 s, then the required rotational stiffness must be

$$k_\theta = \left(\frac{2\pi}{P}\right)^2 I = 9.91 \times 10^{-6} \left(\frac{\text{N} \cdot \text{m}}{\text{rad}}\right). \tag{3.6}$$

The rotational displacement noise due to ground vibrations is then

$$\theta_n = \frac{\Gamma_S}{k_\theta} \approx 8 \times 10^{-10} \left(\frac{\text{rad}}{\sqrt{\text{Hz}}}\right). \tag{3.7}$$

This is the maximum rotational sensitivity of the Superconducting Torsion Balance, assuming methods of seismic isolation are not employed, or if the centre-of-mass to centre-of-buoyancy displacement distance of the test mass can't be reduced below 0.5 μm through either precise machining or in-situ tuning. Any displacement sensor must be sensitive to this level.

Conventionally it is useful to have this required sensitivity in terms of a displacement noise (m/$\sqrt{\text{Hz}}$) for comparison with a detector's displacement sensitivity. As described in Section 3.1.1, a differential capacitive sensor was used as the displacement sensor for the float and test mass. The two capacitive electrodes in the transducer bridge were separated at their centres by a distance, s, of 40 mm. The required displacement sensitivity of the capacitive sensor was then,

$$\delta d = s\theta_n = 32 \left(\frac{p\text{m}}{\sqrt{\text{Hz}}}\right). \tag{3.8}$$

This value is compared to the capacitive sensor designs and noise measurements described in Chapter 4.

3.2 Experimental Work

My original contribution to the experimental setup of the Superconducting Torsion Balance is described in this section. It consisted of designing and implementing a capacitive displacement

sensor for the float (discussed in detail in Chapter 4), redesigning the float design to allow more precise vertical positioning via the use of three Attocube micro-positioners acting as a kinematic mount, re-wiring the heatswitches used to store, maintain and change the persistent currents in the superconducting lead coils in the bearing, designing a baseplate for the experiment to host heater resistors and level probe mounts, and calibrating the Allen Bradley resistors used to measure the temperature on the experimental cavity exterior.

3.2.1 Float Redesign

The original system for positioning the float vertically was a single Attocube micro-positioner that raised a lowered a small copper pillar based in the centre of the bearing. This is shown in Figure 3.14. The float then rested on this with a small rounded surface attached to the centre of its inner top surface, shown in Figure 3.15. While the curved surface would have prevented any significant tilting of the float, due to it's position at the centre of the bearing it was visually concealed and so the moment of contact with the float was hard to ascertain. As such it was difficult to know at what position it began to lift the float. Section 3.3 highlights the importance of knowing the height of the float with regards to being able to levitate it with the superconducting levitation coil and so a different system was envisioned.

A new method of lifting the float at three contact points with three different Attocube micro-positioners acting as a kinematic mount was decided upon. This would have the advantage of allowing visual confirmation of the points of contact with the float, hence allowing for a calibration for the separate Attocube positions at which the float would start to be lifted above the levitation coil in the bearing. This in turn would allow for a far more accurate knowledge of the height of the float at any given time once the experimental cavity was sealed. It would also allow for adjustments to the tilt of the float if it needed to be made more horizontal with respect to the ground. This involved designing an attachment to the float that would allow it to rest upon the three Attocubes that were placed exterior to the bearing. This attachment was designed in Autodesk Inventor, and is shown in Figures 3.16 and 3.17, along with a model of the float, where in the latter groves

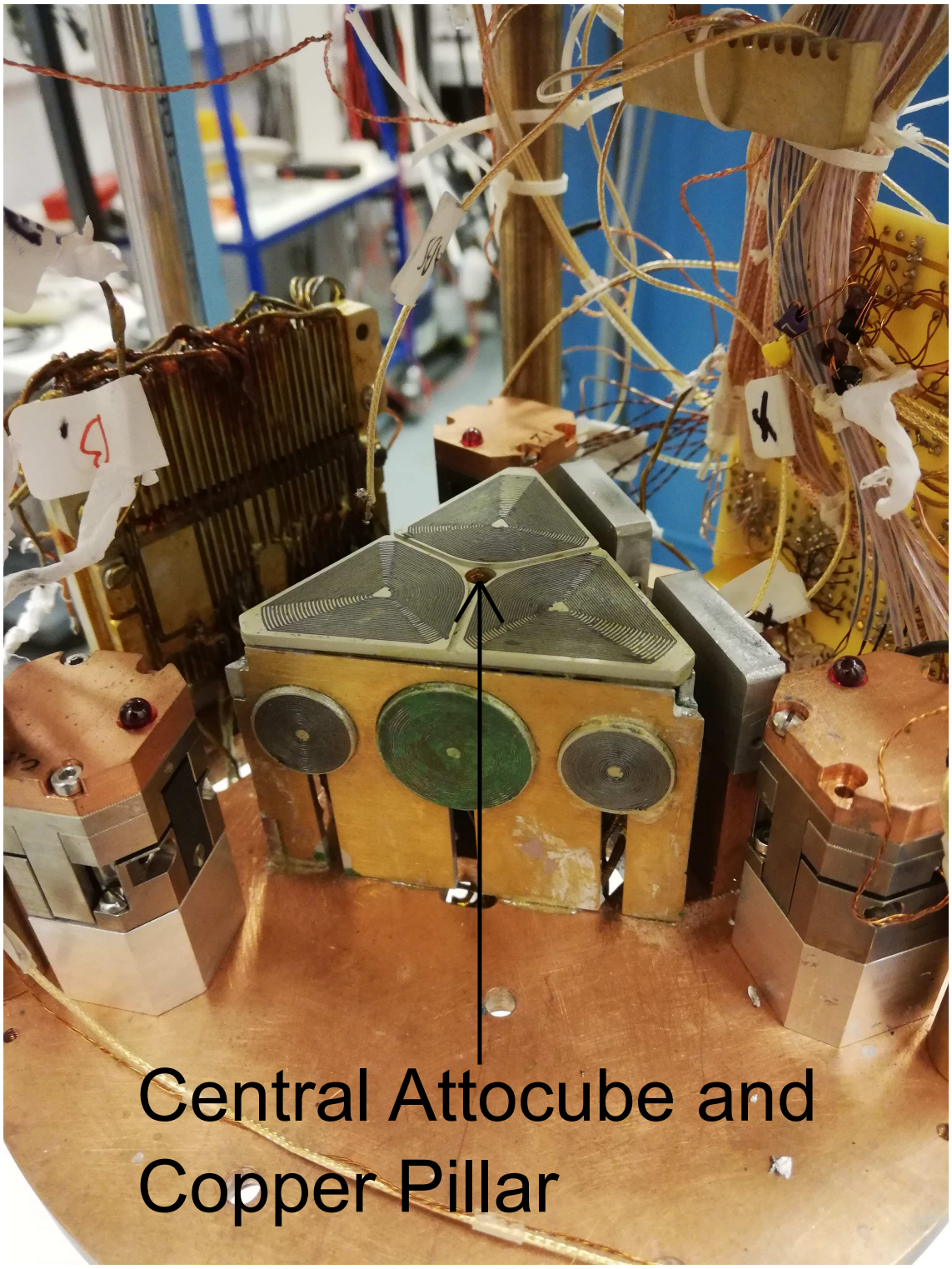

Figure 3.14: A photograph of the bearing highlighting the position of the old vertical positioning Attocube micro-positioner at the centre.

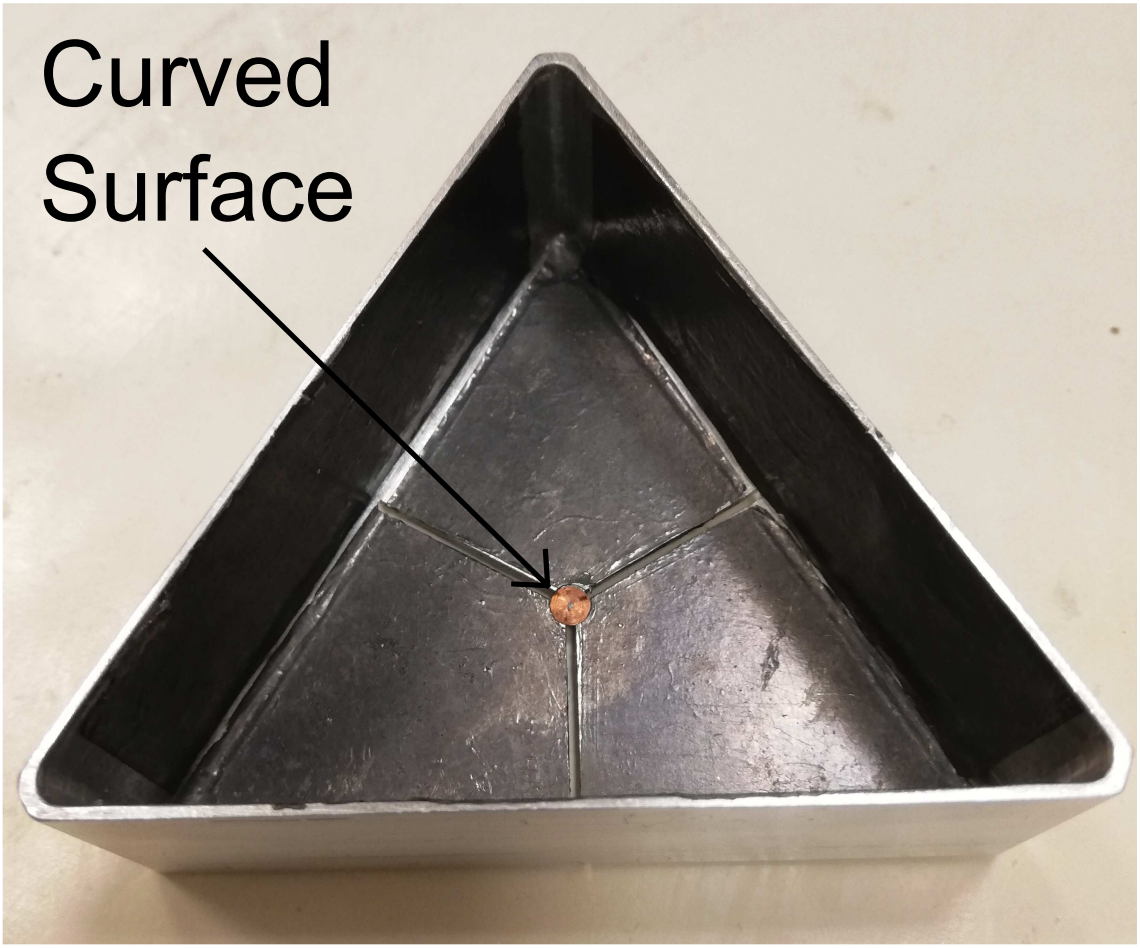

Figure 3.15: A photograph of an older version of the float showing the curved surface attached to the centre of its inner top surface with which it rested on the copper pillar on the Attocube micro-positioner at the centre of the bearing.

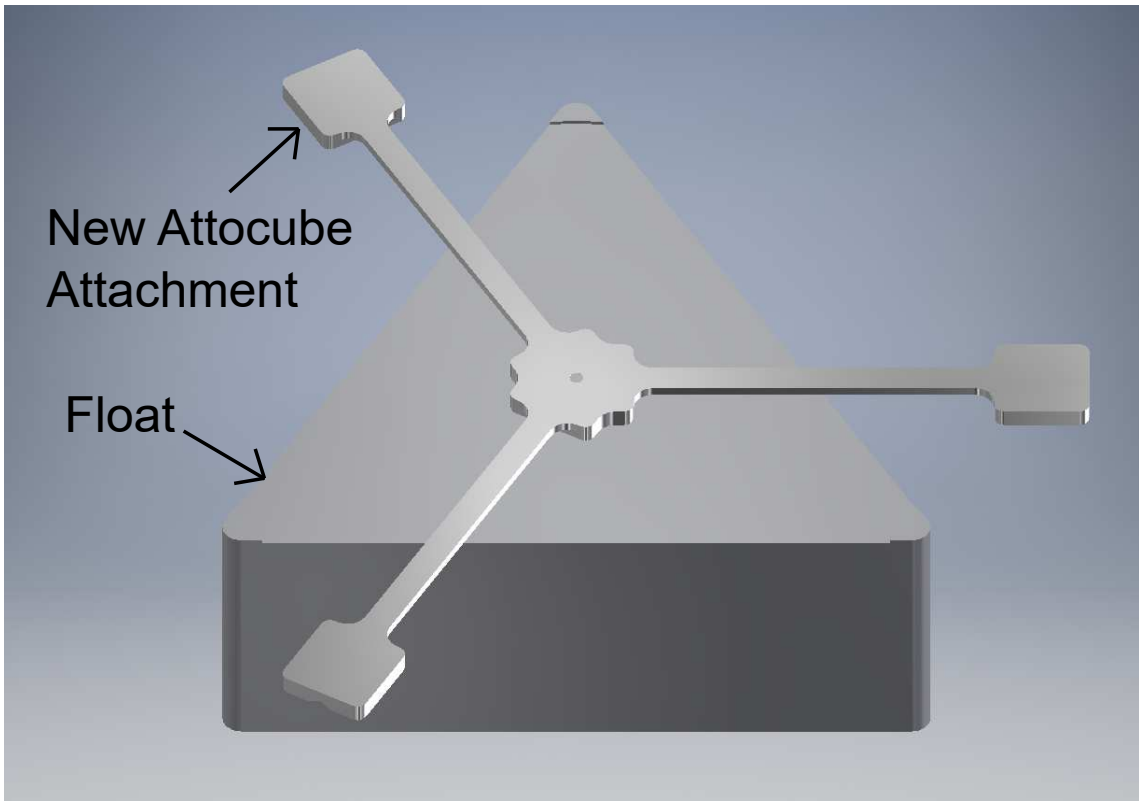

Figure 3.16: A top-down graphic of the design of the attachment to the float to allow it to rest upon three Attocube micro-positioners.

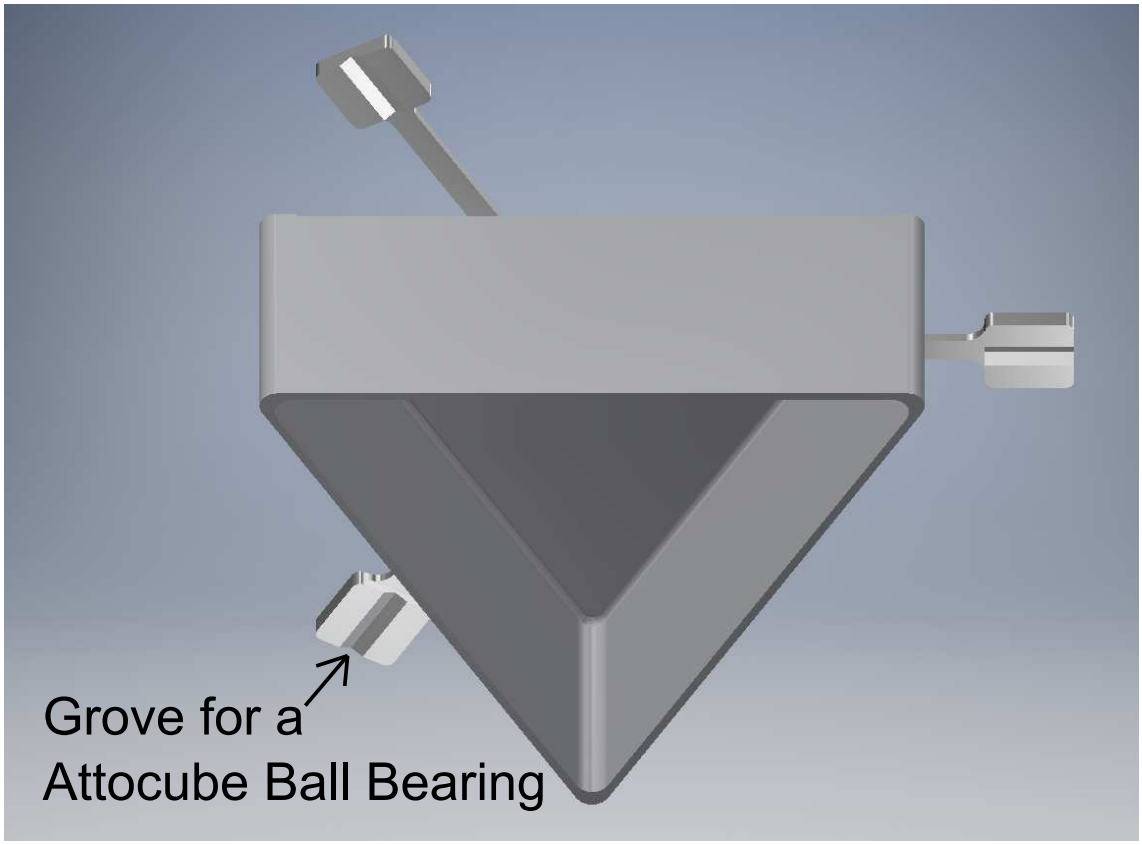

Figure 3.17: A bottum-up graphic of the design of the attachment to the float to allow it to rest upon three Attocube micro-positioners.

on the underside of this attachment show where it rests on the ball bearings atop the Attocubes. Figure 3.18 shows how this new setup looks in practice, with the float and the attachment able to be positioned vertically using the three separate Attocubes which were located in a equilateral triangle pattern to match the shape of the float, and centred on the bearing-float system.

3.2.2 Heatswitch Design

The heatswitches were essential for storing, maintaining and changing the persistent currents in the superconducting coils in the bearing. To minimise heat-leak along the wires from the environment, the 10 different coils had to be wound in series, across two different circuits, using lead wire. The heatswitches themselves were made from 50 μm diameter constantan wire and were physically wrapped around a small length (approximately 1 cm) of the lead wire connected to the coils in the bearing. The wire length of the constantan heatswitches was chosen to give a total resistance along them of 100 Ω. They were heat sunk to lead wires using GE varnish. The circuit called the 'Levitation Circuit' consisted of the top levitation coil and the 3 large side coils and their associated heatswitches. The circuit called the 'Stabilisation Circuit' consisted of the 6 small sides coils and their heatswitches. The designs for these circuits are shown in Figures 3.19 and 3.20 respectively.

These circuits, which were controlled via the experiment's LabVIEW software, worked by taking advantage of the properties of superconductors. The heatswitches were all on a separate circuit from the coils, and could be operated independently from one another. At 4.2 K, any current sent from the exterior electronics to the lead wire of the coils' circuit would simply bypass the coils, due to their impedance from the inductance of the coils themselves. If, however, prior to this a current was sent to a heatswitch to 'turn it on', this would heat up that small section of the lead wire and drive it normal. This would force any current along the lead wire to go through the associated coil. Then, while still driving a current through the coil, if the heatswitch was 'turned off' by stopping the current flowing through it, the relevant section of the lead wire would cool down and become superconducting again, completing a loop of persistent current with the coil. The drive current from the exterior electronics could then be stopped. To remove a persistent current from any of

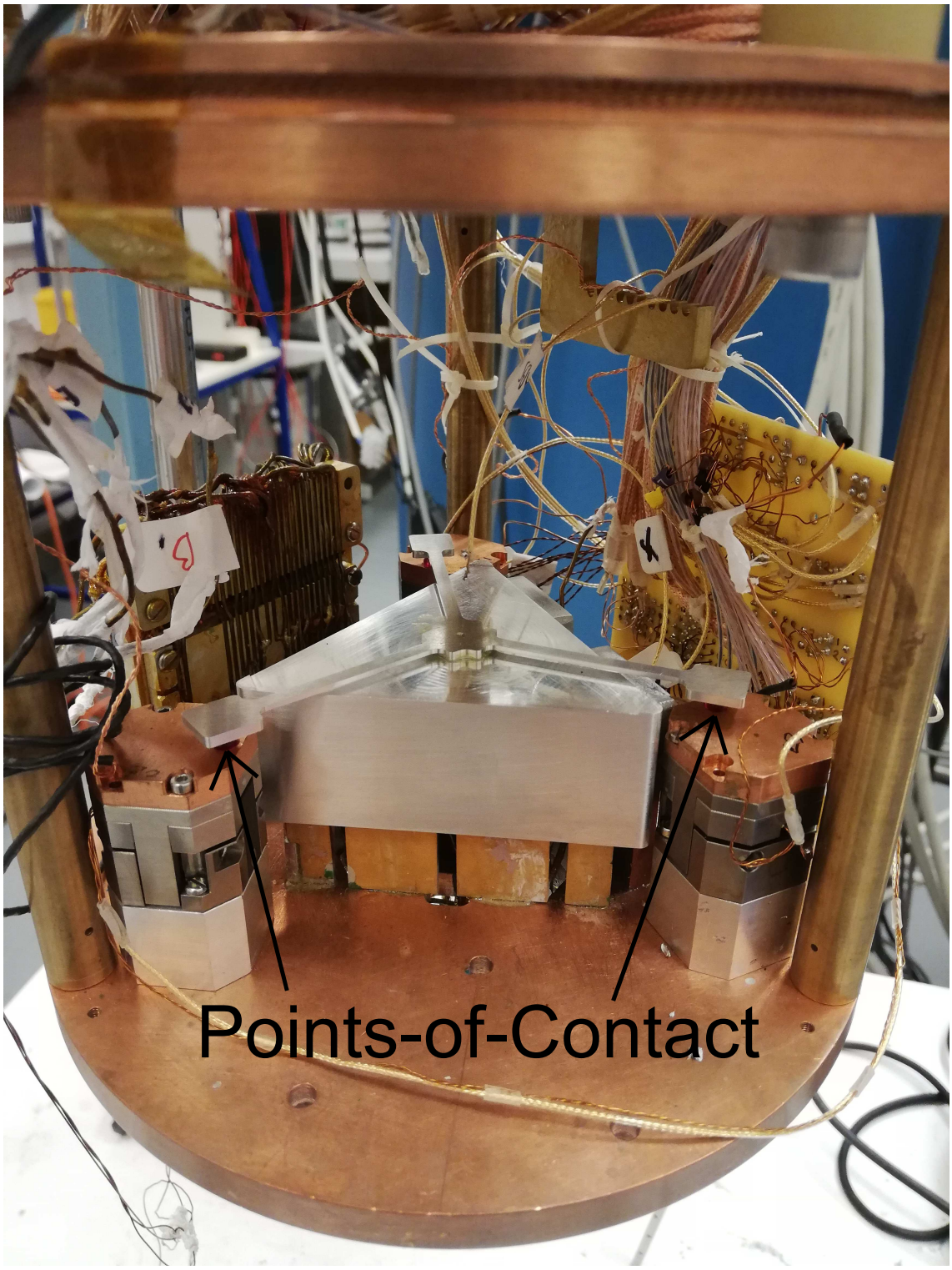

Figure 3.18: A photograph showing the float with the attachment allowing it to rest on top of the Attocubes.

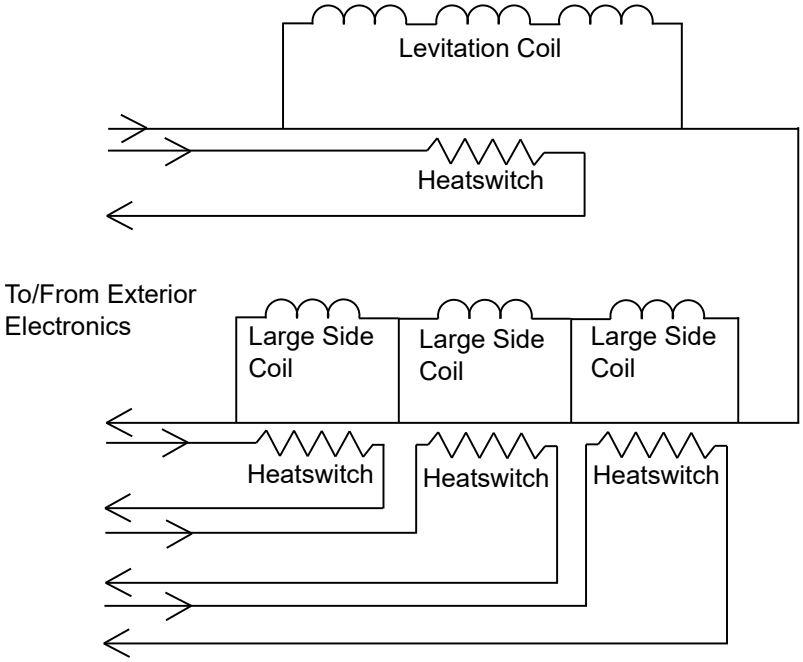

Figure 3.19: A circuit diagram of the Levitation Circuit.

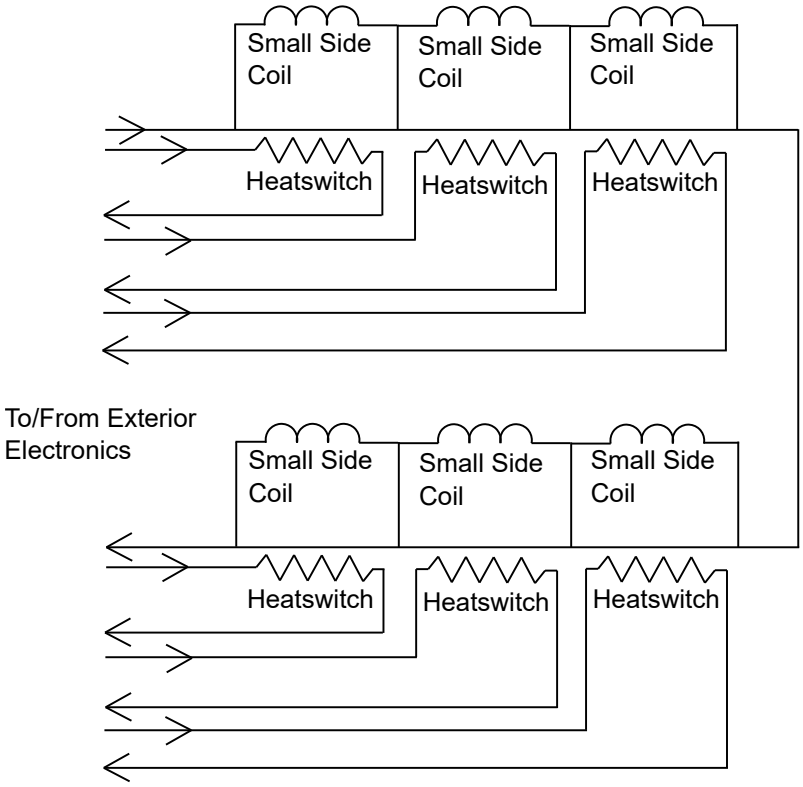

Figure 3.20: A circuit diagram of the Stabilisation Circuit

the coils, the relevant heatswitch could just be turned on to break the superconducting loop. The heatswitches were typically switched on using a 20 mA current for 1 second; while the current to the lead coil circuit would last for 3 seconds, starting 1 second before and stopping 1 second after the heatswitch current. In this way, a persistent current could be introduced to or removed from any of the 10 superconducting coils in the bearing, independently of the the other coils. The heatswitches were located at positions on the lead wire that were sufficiently isolated from other superconducting elements to eliminate the possibility of accidental heating. A photograph of some of the heatswitches, wrapped around the lead wire, is shown in Figure 3.21.

3.2.3 Baseplate, Heater Resistors and Level Probe Mounts

At the base of the experimental infrastructure, below the experimental cavity, there was a baseplate that was designed in Autodesk Inventor and implemented to house heater resistors and level probe mounts. Once the experiment was inside the cryogenic dewar the baseplate would be in contact the floor of the dewar. The baseplate was made of 2 mm thick aluminium and was connected to the bottom of the experimental cavity by 6 cm long stainless steel posts. The heater resistors, which consisted of 14 40 Ω power resistors wired in parallel and screwed in place onto the baseplate, were used to heat up the bottom of the cryogenic dewar, to boil off and remove any remaining liquid nitrogen prior to the introduction of liquid helium. This was done by running a current, typically around 5 A, through them when necessary. The stainless steel posts ensured minimum heat transfer between the baseplate and the experimental cavity. The baseplate also had through-holes to help prevent liquid nitrogen from pooling underneath it and becoming trapped. It also featured a circular cutaway on its edge to allow the attachment to the pipe for pumping out liquid nitrogen and pumping in liquid helium to get flush to the dewar floor.

To monitor the levels of liquid nitrogen and helium present in the cryogenic dewar containing the experiment, level probes were used. These were supported from below by mounts that were also designed in Autodesk Inventor to accommodate them specifically. These mounts were made of aluminium and were screwed into position on the baseplate. Another threaded hole on the side of

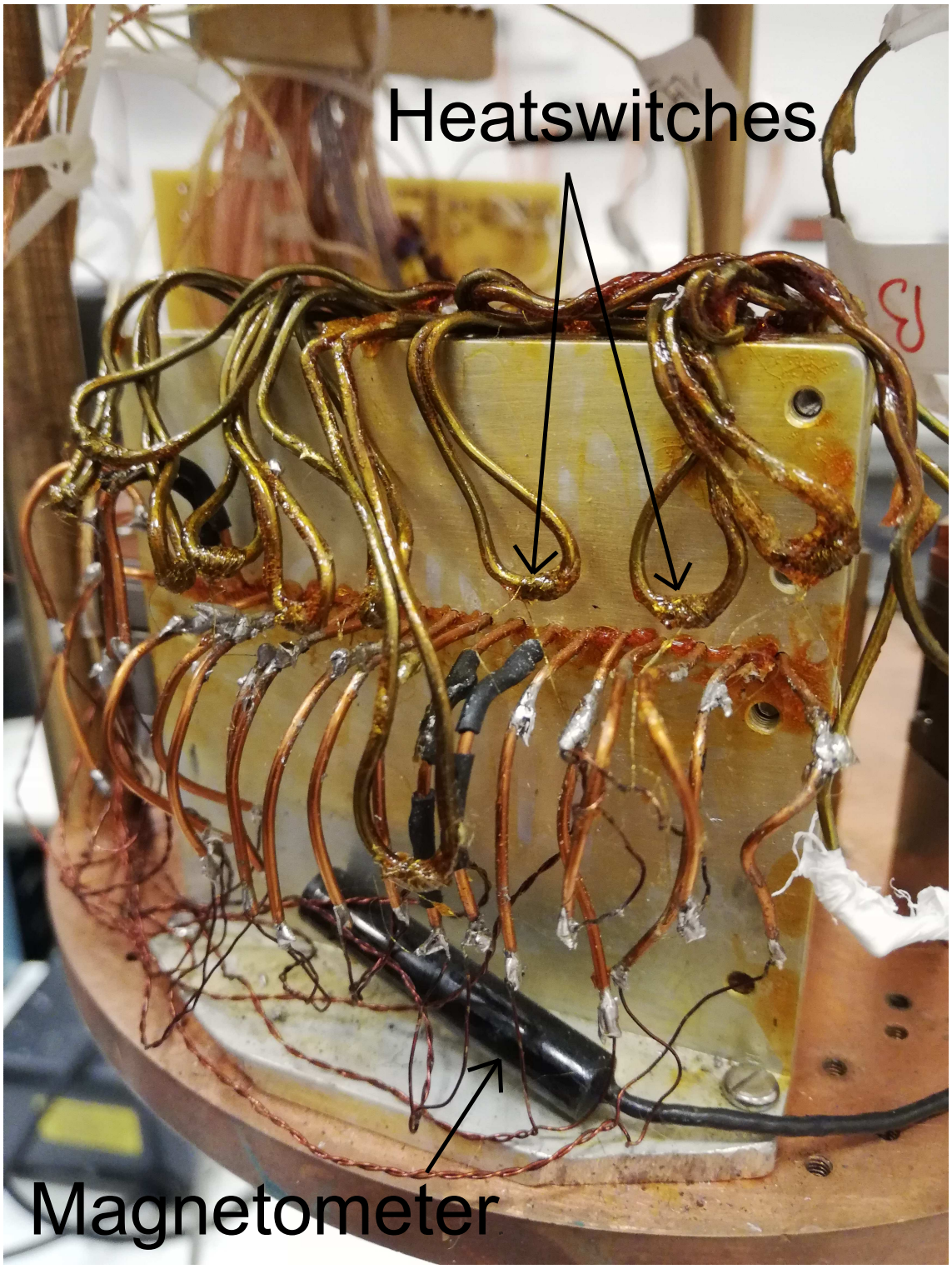

Figure 3.21: A photograph highlighting some of the heatswitches wrapped around the lead wire of the coils. The magnetometer used in the experiment is also shown.

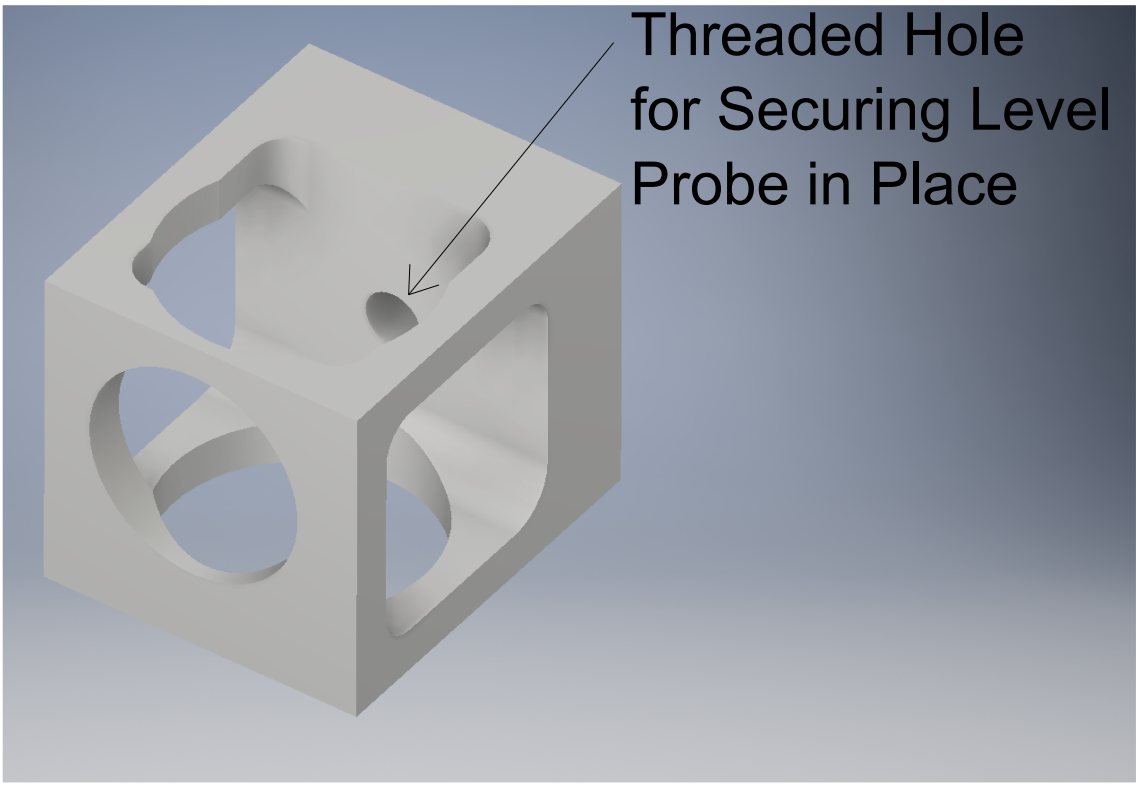

Figure 3.22: A graphic of the design of the level probe mounts used to secure the probes in place at the baseplate.

the mounts could be used to secure the bottom of the probes into the mounts. The design of the probe mounts is shown in Figure 3.22. The design of the baseplate, complete with the stainless steel posts and the probe mounts, is shown in Figure 3.23. A photograph of the baseplate in position, attached to the experimental cavity with the level probes and their mounts in place, is shown in Figure 3.24.

The experiment was designed such that the vertical struts connecting the experimental cavity and baseplate to the baffles above them, were slack in the vertical direction. This meant as the experiment was lowered into the cryogenic dewar using a crane the baseplate, and hence the experimental cavity itself, would always sit rigidly and stably on the floor of the cryogenic dewar as the struts would simply rise once the baseplate was in contact with the dewar floor. This allowed the experiment to be correctly and securely lowered into the cryogenic dewar every time.

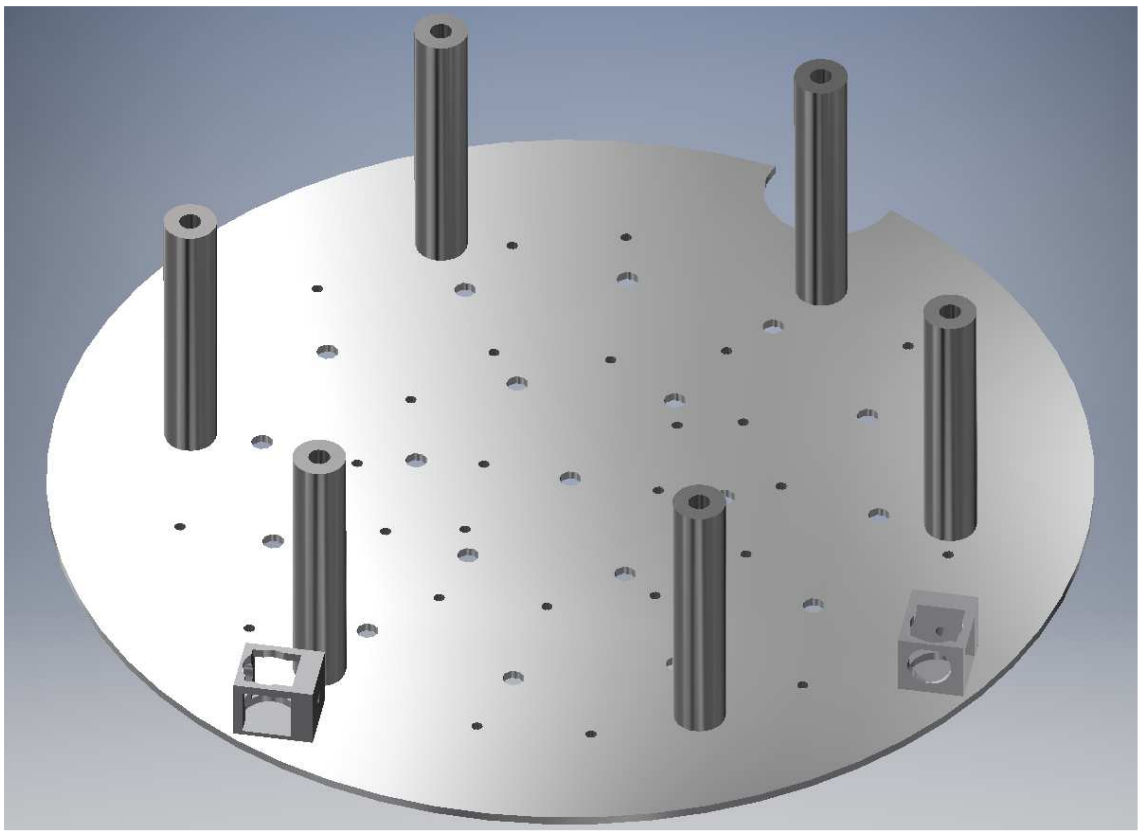

Figure 3.23: A graphic of the design of the baseplate, complete with the stainless steel posts used to connect it to the experimental cavity and the level probe mounts.

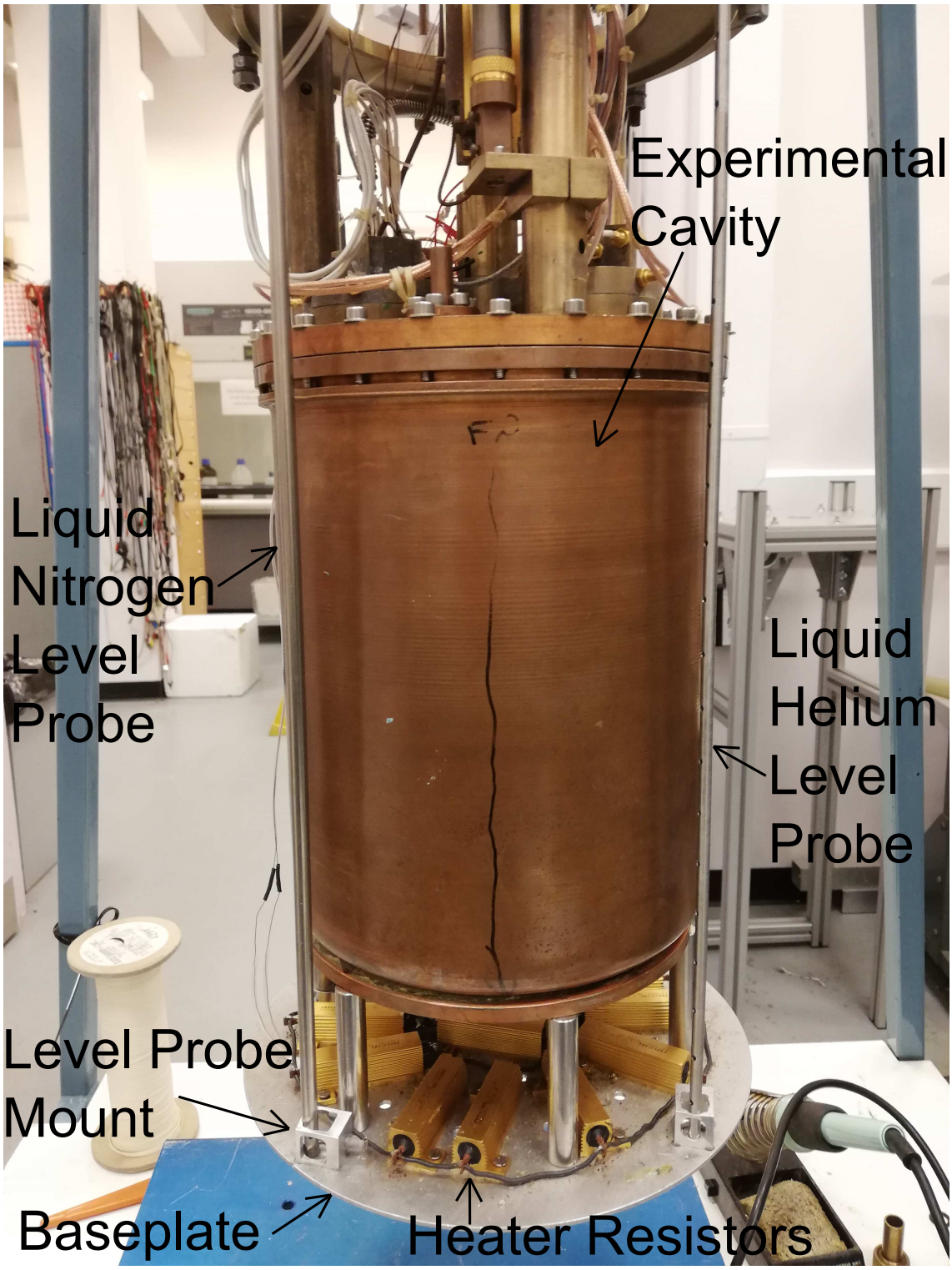

Figure 3.24: A photograph of the baseplate in position, attached to the experimental cavity, with the level probes and their mounts in place.

3.2.4 Allen Bradley Resistors Calibration

In addition to the experimental cavity interior and exterior silicon diodes used for temperature sensing, there were also 3 Allen Bradley resistors used on the exterior of the experimental cavity. These were located at different heights along the length of the experimental apparatus to aid in the cryogenic level diagnostics in the event that the liquid nitrogen and helium level probes failed during an experiment. One was located below the experimental cavity, one was located directly one top, and one was located approximately 15 cm above the cavity. As this temperature measurement was sensitive to changes in resistance over an extended cable length of several metres, the Allen Bradley resistances were monitored using four-terminal sensing with a Keithley 2000 multimeter. A diagram highlighting the wiring and location of these Allen Bradley resistors in relation to the experiment and the silicon diodes is shown in Figure 3.25.

The changing resistance of these resistors with temperature had to be calibrated. This was done by submerging them in liquid nitrogen and then liquid helium, while placed next to the pre-calibrated exterior silicon diode temperature sensor. This allowed their changing resistances to be compared to the local temperature as it decreased from room temperature down to 4.2 K. The results for this calibration are shown in Figure 3.26. A power law fit was then applied to the relation between resistance and temperature for each Allen Bradley resistor. The data was amended to take into account the transfer between liquid nitrogen and liquid helium, by removing the measurements over the period where it started to heat up in this interval. This explains some of the breaks in the data. The other anomalies in the measured data curves could be due to the non-uniform cooling at the location of the resistors due to the pooling of the cyrogens. The calibration was not required to a high accuracy; a precision of $\pm$ 1 K was sufficient as the Allen Bradley resistors were intended as a rough guide, and as the silicon diodes were more accurate and combined with the level probes, meant that an approximate reference from the Allen Bradley resistors was all that was needed. During cryogenic experiments these basic fits were found to be adequate for our needs.

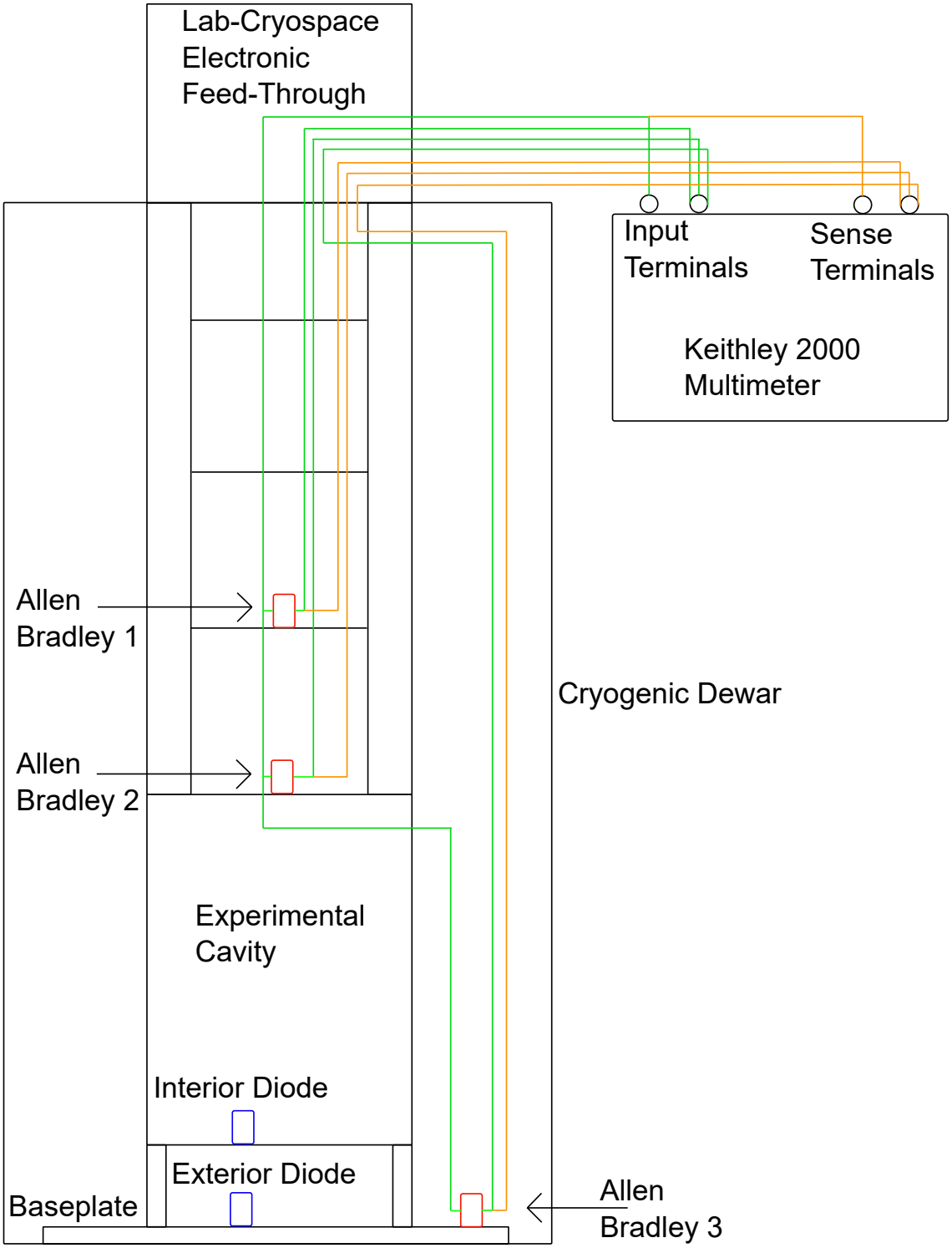

Figure 3.25: A diagram showing the position of the Allen Bradley resistors relative to the other main components in the experiment and how they are wired to an external Keithley 2000 multimeter. This diagram is not to scale.

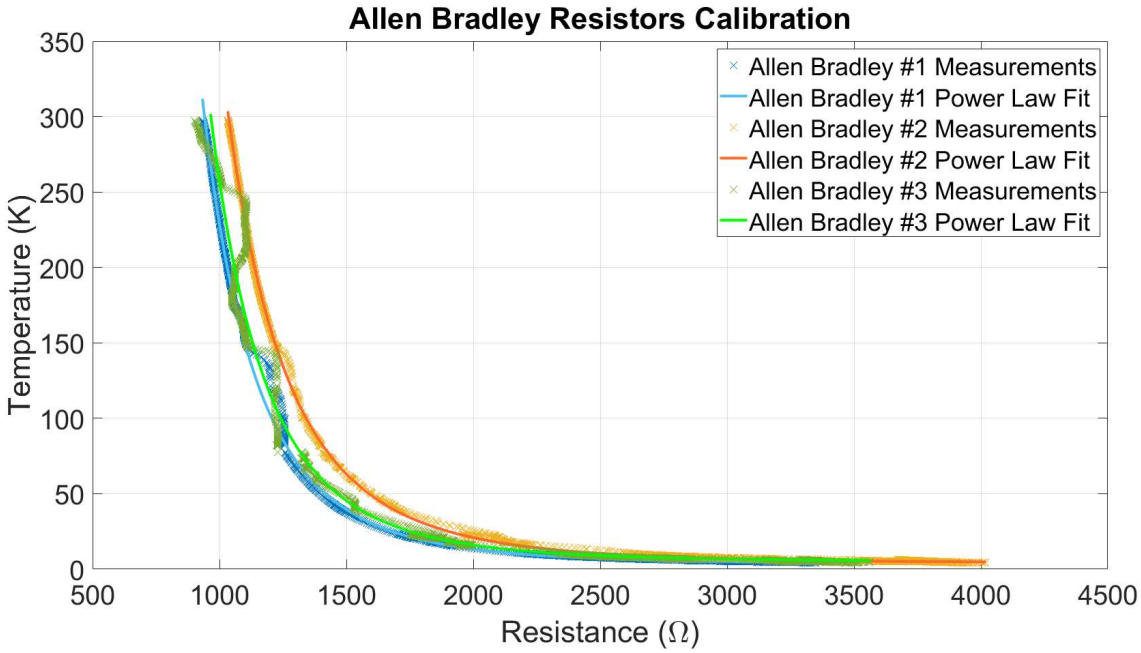

Figure 3.26: The results of the calibration of the Allen Bradley resistors, showing their resistance change from room temperate down to 4.2 K and their associated power law fits.

3.3 FEMM Modelling

I used finite element analysis software (FEMM, the details of which are found at this link: http://www.femm.info/wiki/HomePage) in order to predict the forces that would be applied to the float from the superconducting coils. Specifically, to predict the levitation height of the float above the top surface of the bearing by the levitation coil. This depended on the upward levitation force applied to the float from the coil. The maximum force at a given float height above the coil, z, could be described by [35],

$$F(z) = -\frac{\mathrm{d}E(z)}{\mathrm{d}z} = \frac{1}{2}\frac{\Phi_0^2}{L(z)^2}\frac{\mathrm{d}L(z)}{\mathrm{d}z} = \frac{1}{2}\frac{\mathrm{d}L(z)}{\mathrm{d}z} i_c^2(z), \tag{3.9}$$

where $E = \Phi_0^2/2L(z)$, and $\Phi_0 = L(z)\, i_c(z)$ and is a constant. It can be seen that it depends on the critical current of the coil, $i_c(z)$, and the rate of change of its inductance, $L(z)$, with respect to the float's height at z.

The critical current depends on the critical field and this relation is described by the Silsbee effect [46]. The critical field is defined as the maximum magnetic field strength at which a material

can remain superconducting and this is temperature dependent. Should the magnetic field exceed this maximum then it will drive the material normal and it would no longer exhibit zero resistance or the Meissner effect. The critical field is related to the critical temperature, which similarly is the maximum temperature at which a material can remain superconducting [46]. The critical field and temperature depend on the material in question; for the superconducting torsion balance the superconducting material used was lead.

Lead was chosen as its critical temperature, 7.193 K [47], was sufficiently larger than the boiling point of helium, 4.222 K. This meant liquid helium could be used as the cryogenic coolant for the experiment. An alternative material was niobium with its critical temperature of 9.500 K [47] but, as mentioned in Section 3.4, this material proved too difficult to work with. The theoretical critical field of lead at 0 K is 0.0803 T [47].

The relation between critical field and critical temperature for a given material can be described by the approximation [48],

$$B_c(T) \approx B_c(0)\left[1 - \left(\frac{T}{T_c}\right)^2\right], \tag{3.10}$$

where $B_c(T)$ is the critical field at temperature, T. $B_c(0)$ is the theoretical critical field at 0 K and T_c is the material's critical temperature. Using this relation, lead's critical field at 4.222 K was calculated to be 0.053 T.

Another important relation needed when determining the levitation force was the conservation of magnetic flux [36],

$$\Phi = L_0 I_0 = L_1 I_1, \tag{3.11}$$

where L_0 and I_0 are the inductance and persistent current respectively in the levitation coil at an initial time and L_1 and I_1 being at a later time. This is a consequence of persistent currents in superconducting circuits. If at a given time the levitation coil has an inductance associated with it and a persistent current is flowing in the coil, and then the inductance changes, the current must also change in order to compensate for the changing magnetic flux through Lenz's law. In the case of the float being lowered onto the superconducting coil, the inductance would decrease

with decreasing float height as it is proportional to the volume of the gap between the coil and float [30], as described in Chapter 2. So in addition to knowing the critical current, it is important to take into account how the persistent current in the levitation coil changes as the float is lowered to ensure it does not exceed the critical current.

The changing inductance with float height from Equation 3.9 could be estimated using FEMM and Equation 3.11. With FEMM a 2-dimensional model consisting of the levitation coil in the bearing and the float was created. FEMM was limited in what geometries it could model, and so in modelling the float and levitation coil they were represented as a circular surface and coil respectively. The circular version of the coil matched the area and the number of coil windings as one of the triangular kite-shaped sections of the levitation coil described in Section 3.1, and for the purposes of calculating the inductances and forces the values from FEMM were multiplied by 3 to then represent the whole coil and float. In the program these were drawn as a 2-dimensional slice from the centre to the edge along the radius of both, and FEMM would then assume cylindrical symmetry around the 'centre' on one edge to create a pseudo-3-dimensional model. A screenshot to demonstrate this model in FEMM is shown in Figure 3.27. In the model, the diameter of the lead wire in the coils was 250 μm, with a separation between the centres of each adjacent coil winding being 350 μm, for a total of 29 windings. This included the outer winding which was wired in an opposite direction to the inner windings, as mentioned in Section 3.1. The gap between the centre symmetry axis and the first coil winding was 1 mm, meaning the total radius of the coil and its holder was 11.15 mm. As only the bottom surface of the float facing the levitation coil was considered, its sides were ignored and in the model it was left to overhang the coil. The layer of lead foil on the bottom surface of the float was 25 μm. The vertical dimension of the aluminium parts of both the float and coil holder was 1 mm. These values were chosen to match the sizes of the real components as close as possible, within the limitations of the FEMM software, as mentioned in Sectiom 3.1. Figure 3.28 shows the FEMM software at work calculating the magnetic field and inductance across the model for a float-levitation coil gap of 100 μm. Figure 3.29 gives a close-up of this, focussing on the outside coil winding wired in the opposite direction to prevent magnetic field

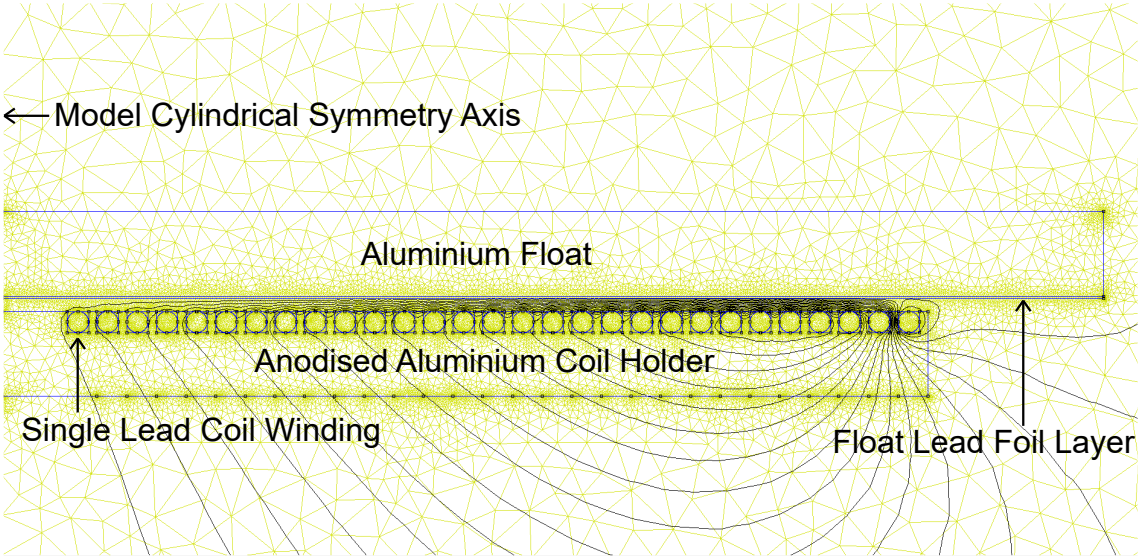

Figure 3.27: A screenshot of the FEMM software showing a slice across the radius of the coil and float. The cylindrical symmetry axis that the software used is highlighted, as are the different parts that were explicitly modelled.

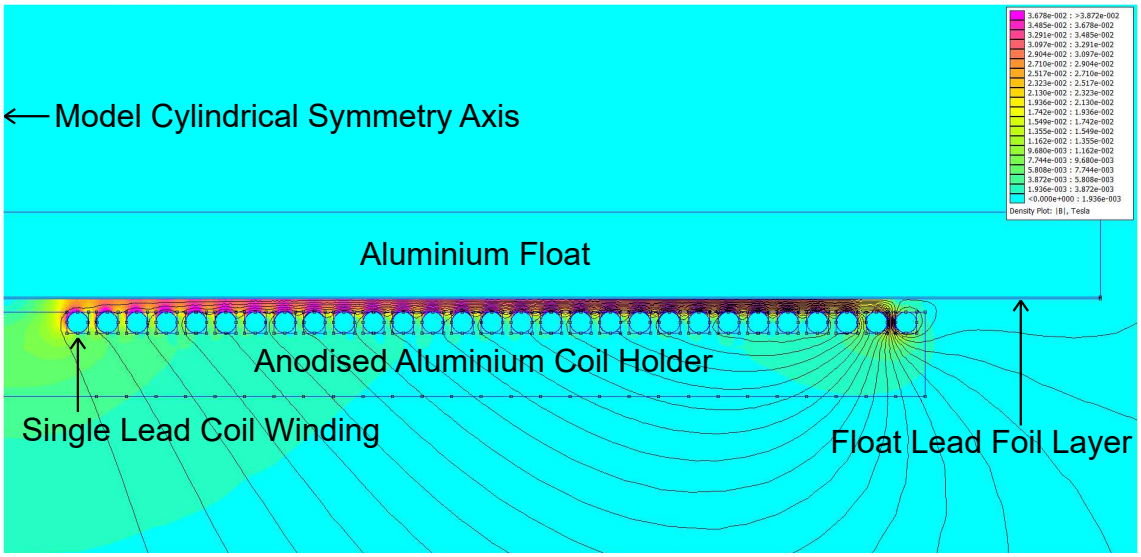

Figure 3.28: A screenshot of the FEMM software showing it calculating the magnetic field and inductance values across the model, in this case the gap between the float and levitation coil is 100 μm.

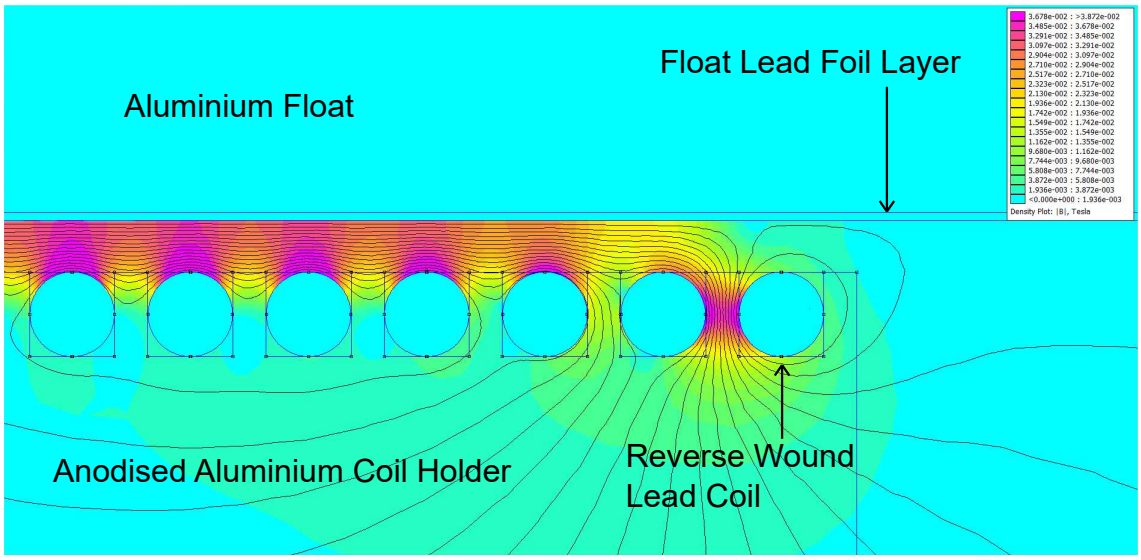

Figure 3.29: A close-up screenshot of the FEMM software focussing on the outside coil winding wired in the opposite direction to prevent magnetic field leakage, in this case the gap between the float and levitation coil is again 100 μm.

leakage. This shows that the outside coil winding successfully reduces the magnetic field leakage by lowering the magnitude of the magnetic field immediately outside the coil by at least a factor of 20 compared to the coil's interior.

The program was run with the float at an initial height of 250 μm and with a range of initial persistent currents in the levitation coil. FEMM would calculate the inductance of the coil, then float would be lowered by 10 μm and FEMM would calculate the inductance again. This would be repeated to a float height of 50 μm. At each float height stage, the magnetic field on the surface of the coil windings was also measured. By using these inductance values and initial currents with Equation 3.11, the changing persistent current in the coil could be calculated as well as the change of inductance with float height. It could also be noted at what current the magnetic field on the coil windings exceeded the critical field at a given float height, providing an estimation of the critical current for the levitation coil. These values could then be used with Equation 3.9 to calculate the maximum vertical lift force from the coil, as well as the minimum coil current needed in order to levitate the float based on its mass, at a given float height. The results of this simulation are shown

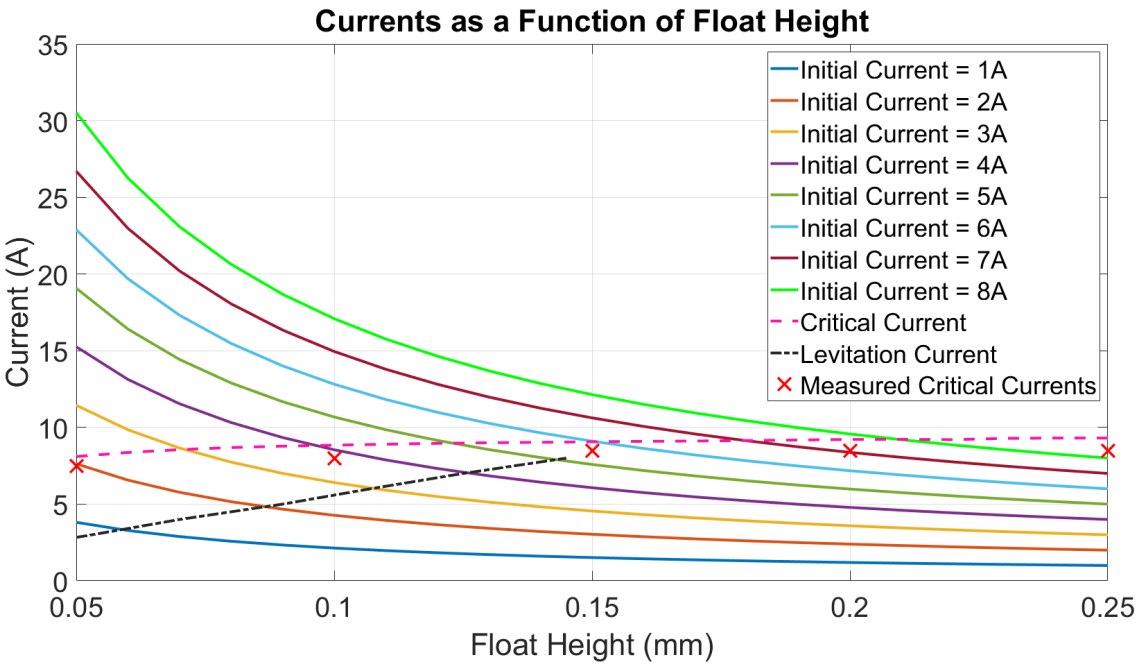

Figure 3.30: The results of the FEMM simulation of the changing persistent currents in the levitation coil as well the critical current as a function of float height. The measured critical currents and the current required for levitating the float as a function of float height are also shown. It can be seen that it should be possible to levitate the float without exceeding the measured critical currents.

in Figure 3.30. These results show how the persistent currents increased from an initial current as the float was lowered onto the bearing. The model critical current is also displayed. In addition, the measured critical current at different float heights is shown for comparison. These measured currents were determined by increasing the persistent current in the levitation coil in steps until the magnetic field measured by the magnetometer located near the bearing stopped increasing for a given increase in input current, while at 4.2 K. This was done at several different float heights as shown in Figure 3.30. Figure 3.31 gives an example of this critical current measurement. The persistent current stored was increased in steps, with a corresponding increase in the magnetic field's magnitude until a drive current of 8 A was used, which did not increase the magnitude of the field, implying that 7.5 A was the critical current at that particular float height of 0.05 mm.

The measured critical currents were lower than the predicted critical currents; by around 1 A at

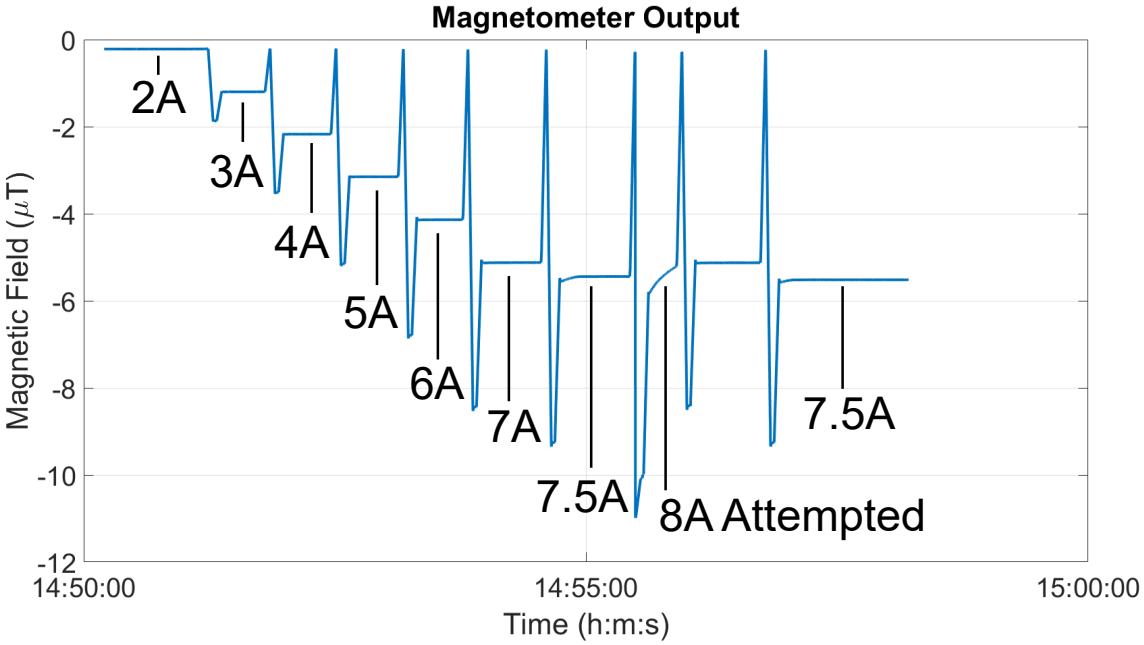

Figure 3.31: The magnetometer output from the experiment, showing the persistent current in the levitation coil being increased in steps before the correspondingly increasing magnetic field magnitude stops despite a larger drive current to the coil, indicating a critical current of 7.5 A had been reached. This was at a float height of 0.05 mm.

large float heights, and by around 0.5 A at smaller heights. This could be due to imperfections in the hand-wound lead coil. Should the lead wire be less than the specified 250 μm diameter at any point along the coil windings then the critical current would also be lower, as these values are proportionally related. The other large source of error here is the approximate geometries used in the FEMM software. A full 3-dimensional model with more accurate coil shapes using, for example, ANSYS Maxwell software would be a more accurate representation of the physical coils and float setup. Time constraints prevented the use of this software. Both the model and the measurements of the critical current in Figure 3.30 predict it decreasing slightly with decreasing float height. This would be due to the fact that the magnetic flux lines from the coil would be compressed into a smaller volume with the decreasing gap, resulting in larger fields for the same current and hence exceeding the critical field at lower currents. Finally, the current required to levitate the float at a given height based on the model's rate of change of inductance with float height is indicated in Figure 3.30. This shows that it should be possible to levitate the float, with its mass of approximately 30 g, without exceeding the measured critical current limit as well as at a reasonable height that is far enough away from the levitation coil such that risks of physical contact are negligible.

3.4 Experiment History and Current Experimental Status

The current Superconducting Torsion Balance experiment has undergone several iterations, with various pieces of hardware and equipment being modified or replaced as issues were identified and then corrected. What follows is a short chronological summary of these changes, focussing on the float design. The first float created for the experiment was made from silica, with the superconducting lining consisting of sputtered niobium panels [33]. This design, however, had a problem with the differential thermal expansion with the test mass foil attached to it which could not be resolved. A float made of sheet niobium was then designed. This version of the float was levitated, and preliminary measurements were taken which showed the rotational stiffness could be tuned in-situ [27]. The measurements contained significant noise however, and the niobium

material was difficult to work with and so the float could not be manufactured to within the required accuracy. Copper floats were then manufactured, with interior lead foil lining and exterior gold foil lining, to be used in conjuncture with an interferometric rotational detector. This interferometer based displacement sensor ultimately could not be reliably used due to issues with the cryogenic vacuum fibre-feed-through. There may also possibly have been issues with localised heating due to the laser. This, combined with the copper floats being close to the upper mass limit of what could be levitated, resulted in the current aluminium float and interior lead lining design which was lighter, and with a change to a capacitive displacement sensor which did not require a reflective surface on the float to operate.

The current experimental status of the Superconducting Torsion Balance is that all the infrastructure, with the exception of the source and test masses, is in place. The source and test mass design and manufacture process has already been tested. The required flatness of $\pm$ 1.5 μm across the surface foils of the masses has yet to be achieved, the current best flatness that has been obtained is $\pm$ 24 μm, but improving this value is conceivable with the aforementioned process in due time. The current float has yet to be levitated reliably. This could be due to a lack of sufficient magnetic field shielding leading to trapped flux in the lead foil on the float [49]. Introducing such shielding would be the next logical step. Another issue could be non-uniform cooling across the masses that could create thermal EMFs resulting in potentially high currents and associated magnetic fields being produced. This would present a similar issue to that due to trapped flux from a lack of magnetic field shielding, and so could be differentiated from that effect when shielding is in place. Issues with the FEMM modelling also remain. As stated in Section 3.3, the modelling of the levitation coil with a circular geometry and multiplying to scale the results up to match the actual three triangular kite-shaped sections of the coil is not ideal. There is also the fact that these three sections are wired in series in a single circuit, where it may be more beneficial to have them wired as their own distinct coil circuits, with regards to the stiffness in the tilting degree of freedom of the float. Preliminary results in FEMM suggested that the difference in tilt stiffness between these designs is negligible. A full, and more accurate, 3-dimensional model in ANSYS

Maxwell software however would help resolve these outstanding questions. Once the current float is levitated it would allow the dynamics and noise of the system to be characterised prior to any measurements of the inverse square law of gravity with the the source and test masses in place.

Chapter 4

The Capacitive Sensor

Reality is that which, when you stop believing in it, doesn't go away.

Philip K. Dick

The text and figures in this chapter are copied from the paper 'A Method for Reducing the Adverse Effects of Stray-Capacitance on Capacitive Sensor Circuits' [28], of which I was an author along with my supervisor Clive Speake. I contributed to the design, and then built, implemented and characterised the capacitive sensing pre-amp circuits described therein. Derivations of the some of the mathematical results in this chapter have been expanded upon in the appendices. The purpose of the work in this chapter was to develop a capacitive displacement sensor sensitive enough to be used on the Superconducting Torsion Balance described in Chapter 3.

In this chapter the increase in voltage noise in capacitive sensor circuits due to the stray-capacitance introduced by connecting cables is examined. The voltage noise of various standard circuits is measured and modelled, and their performance is compared against a benchmark circuit without stray-capacitance that is optimised to have a high signal-to-noise ratio (SNR) for our application. It is shown that a factor limiting sensitivity is the so-called noise gain, which is not easily avoided. In our application the capacitive sensor is located in a metallic vessel and is therefore shielded to some extent from ambient noise at radio frequencies. It is therefore possible to compromise

the shielding of the coaxial connecting cable by effectively electrically floating it. With a cable stray-capacitance of 1.8 nF and at a modulation frequency of 100 kHz, our circuit has an output voltage noise a factor of 3 larger than the benchmark.

4.1 Introduction

Capacitive sensors have a long history of use in scientific measurement [50], and are used extensively across various branches of science [51]. Applications include displacement transducers [52] or straightforward capacitance meters [53]. See the recent review article by Ramanathan *et al.* for further examples of capacitive sensors [54]. Capacitive displacement sensors are attractive devices as they have no Johnson noise and their sensitivity is therefore limited by the noise from the electronics that provides them with a measurable readout. However, for reasonable geometries and frequencies, capacitive sensors have large impedances, and this leads to them being sensitive to the stray-capacitances of coaxial cables that are often needed to connect them to a pre-amplifier. The literature often describes the problems associated with stray-capacitances in terms of the biases they create rather than with increases in noise. This chapter discusses the latter issue. As discussed below, the stray-capacitance can increase the noise gain and severely reduce the SNR. One way to mitigate the effects of stray-capacitance is to reduce the input impedance of the sensor by using a resonant circuit or an impedance matching transformer [55]. These techniques, however, necessarily introduce Johnson noise (although superconducting transformers could mitigate this increase in noise). Further, stray-capacitance associated with the required inductances, transformers, and circuit boards can shift the resonant frequency and make these strategies less robust and straightforward [56]. This chapter proposes an alternative viable method that limits the effect of stray-capacitance on the noise gain as explained below. This improvement comes with a large reduction in the effectiveness of the coaxial cable in shielding the device from ambient electromagnetic environmental interference (RFI). However in many sensitive applications the sensor is placed in a metallic vessel, such as a vacuum chamber or low temperature cryogenic dewar (our case), which can provide reasonable shielding from RFI and additional shielding from coaxial cables may

not be necessary. In such cases degradation of the SNR is avoidable. The optimum choice comes as a trade-off between required SNR and ambient noise.

Stray-capacitance can be a particular issue in cryogenic experimental set-ups where it is necessary to use long coaxial cables that have a small gauge in order to minimise their heat leak and where cryogenic pre-amplifiers and circuits are not suitable. However such fine coaxial cables have large capacitance per unit length. In practice lock-in amplifiers operating at specific frequencies can be used to avoid the effects of interference out of the demodulation band, which can typically be at around 100 kHz. This technique can be successfully employed provided the dynamic range of the pre-amplifier in the detection circuit is not exceeded by the RFI. Therefore, in addition to the noise performance, the effectiveness of the coaxial cable and the surrounding vessel in rejecting electromagnetic interference must be taken into consideration. We suggest below that, by making a minor adjustment to a typical transimpedance capacitive sensor circuit, a satisfactory compromise can be obtained between having a usable noise performance and an acceptable rejection of RFI. We present measurements taken in our laboratory to support this.

4.2 Noise Gain

Before we proceed to describe the details of the circuits that we have tested we will explicitly define the problem of the excess noise introduced by stray-capacitance at the input of an amplifier. Noise gain is a term used in the design of operational amplifiers and appears, from conversations with physicists and engineers, to be little appreciated. However for our purposes it has a definite simple meaning that is illustrated by Figures 4.1 and 4.2. In Figure 4.1 we show a simple diagram of a non-inverting amplifier were we have represented its voltage noise, V_n, in the usual way as a random voltage generator at the non-inverting input of the amplifier. It is clear that the output voltage noise is [57],

$$V_o = GV_n, \tag{4.1}$$

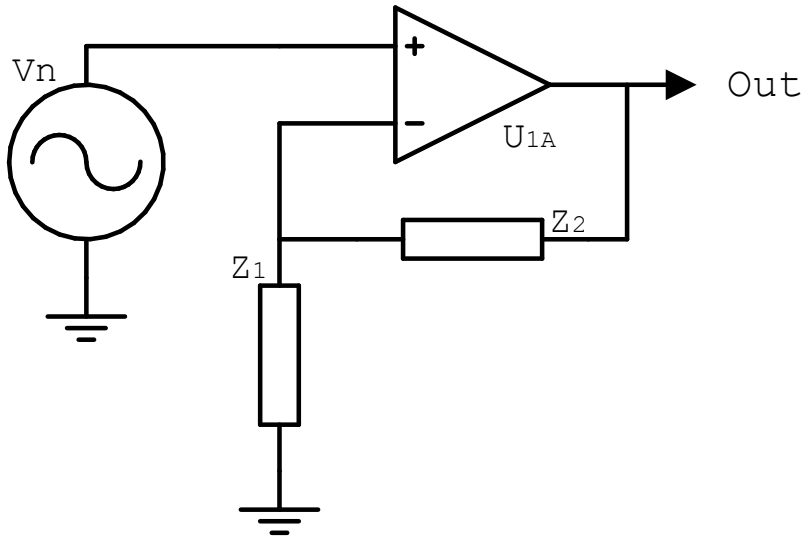

Figure 4.1: A diagram of a typical non-inverting amplifier where the voltage noise of the amplifier is represented by a voltage generator at the non-inverting input.

where

$$G = 1 + \frac{Z_2}{Z_1}. \tag{4.2}$$

G here is the noise gain but it is easily seen to also be the non-inverting signal gain of the amplifier in the infinite gain bandwidth approximation. Now if we examine Figure 4.2 where we have redrawn the amplifier in a transimpedance mode with a high impedance current source, I_1, with impedance, Z_1, connected to its inverting input. It is clear that the output voltage noise from the op-amp is again given by Equation 4.1. It is also clear that the presence of a low impedance to ground, such as that due to stray cable capacitance, at the inverting input of the amplifier can introduce significant output voltage noise.

4.3 Circuit Tests

In this section we present the noise measurements of various capacitive sensor pre-amplifier circuits. The exact circuit used in each case is presented where relevant but the general schematic diagram for all measurements is shown in Figure 4.3, where the signal path to and from the spectrum analyser used to measure the noise is shown.

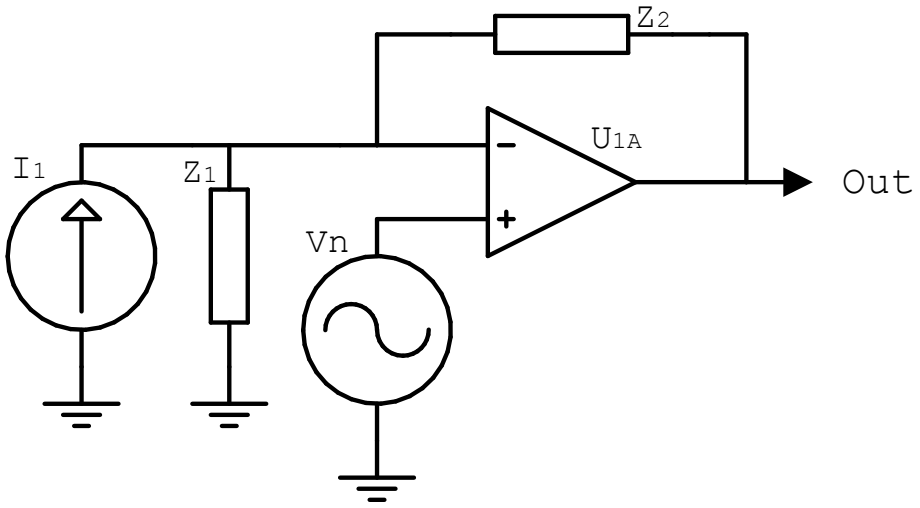

Figure 4.2: A diagram of a typical transimpedance circuit: taking a current input signal I_1 and converting this to a voltage output signal by the op-amp labelled U_{1A}.

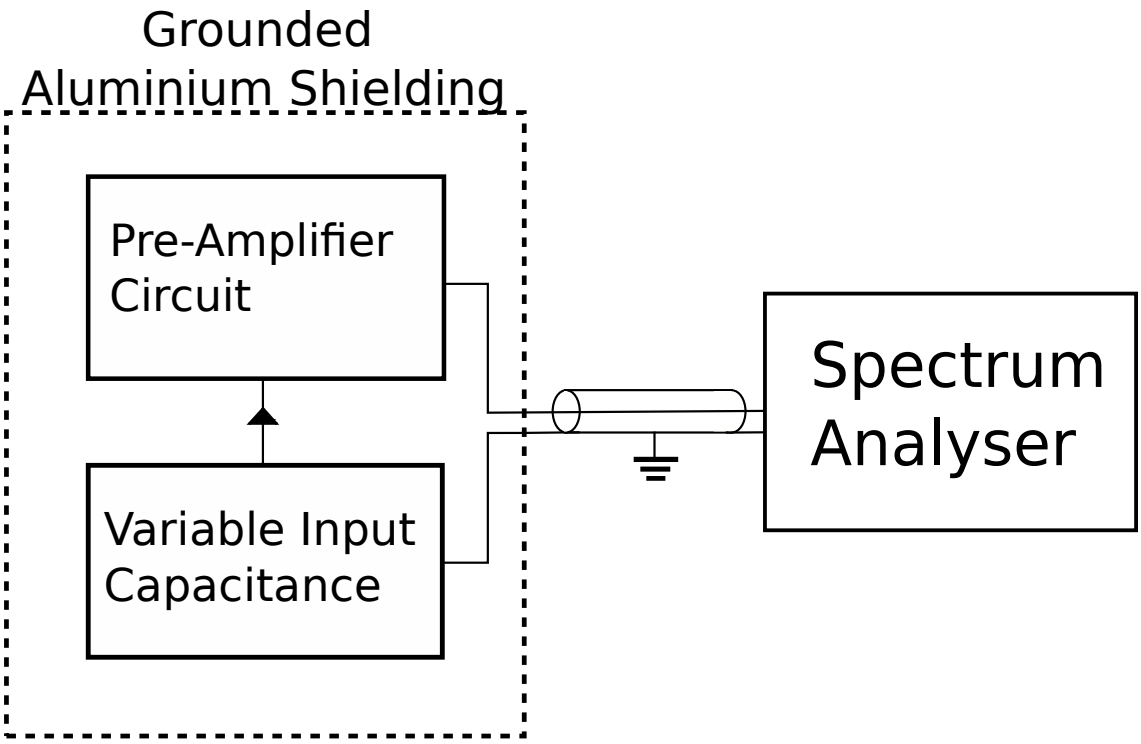

Figure 4.3: A schematic diagram of the measurement set-up for the circuit noise measurements.

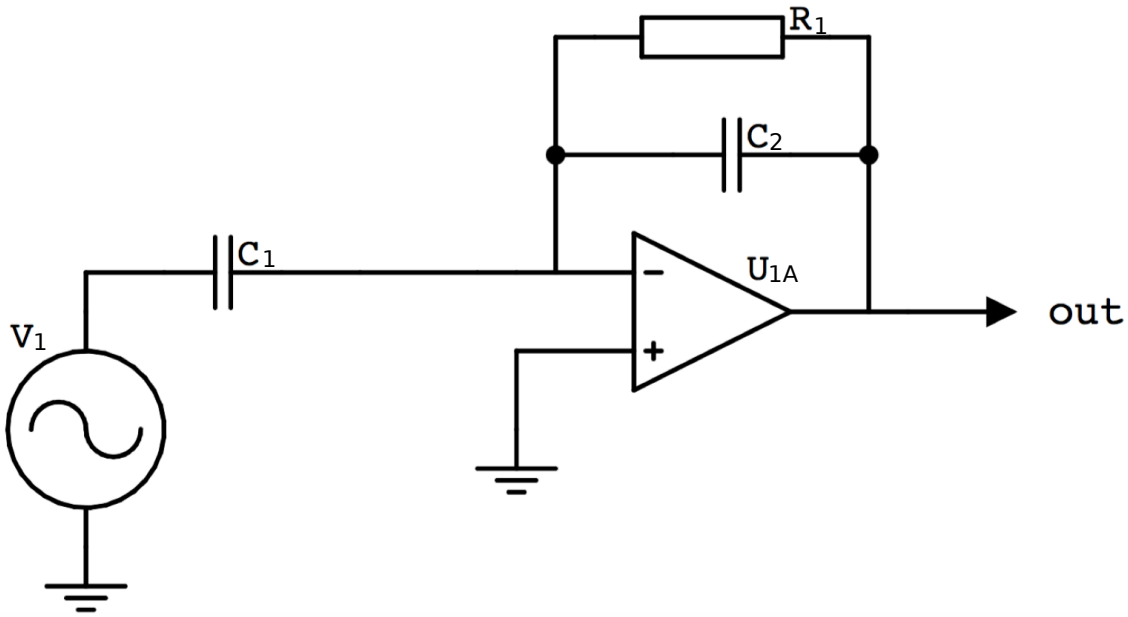

Figure 4.4: A diagram of the benchmark transimpedance circuit: taking a current input signal from the changing capacitance labelled C_1 that is driven by a voltage generator V_1. This is converted to a voltage output signal by the op-amp labelled U_{1A}.

In this section the variable input capacitance and pre-amplifier circuits are located on the same circuit board and within the same aluminium shielding. In Section 4.4, however, these two parts are separated as described in that section.

4.3.1 Benchmark Circuit

A standard transimpedance circuit acting as a capacitive sensor is shown in Figure 4.4 where the voltage generator, V_1, connected to a changing capacitance C_1, produces a current input signal for the op-amp U_{1A}. The absence of stray-capacitance means that this circuit can be considered to be a benchmark in terms of noise. The feedback network consists of a resistor R_1 and capacitor C_2 in parallel.

The output voltage noise from this circuit can be modelled by taking into consideration the main sources of noise present. These are the thermal noise from the feedback resistor R_1, V_{R1}, the current noise density of the op-amp being used, I_n, and the op-amp's voltage noise density, V_n,

which is multiplied by the noise gain of the circuit, G.

Noise gain in general can be changed without modifying signal gain. The noise gain for this benchmark circuit is described by the following equation

$$G = \frac{i\omega C_1 R_1}{1 + i\omega C_2 R_1} + 1, \tag{4.3}$$

where as usual i is $\sqrt{(-1)}$. A derivation of this equation is given in Appendix B. The total output voltage noise, V_T ($\mathrm{V}/\sqrt{\mathrm{Hz}}$), is then given by the equation [57],

$$V_T = \sqrt{(V_{R1}F)^2 + (I_n R_1)^2 + (V_n G)^2}, \tag{4.4}$$

where the amplitude spectral density of Johnson noise in the feedback resistor R_1 is given by the usual expression [58],

$$V_{R1} = \sqrt{4k_B T R_1}. \tag{4.5}$$

F is a one-pole low-pass filter term created by resistor R_1 and capacitor C_2 which acts to attenuate the Johnson noise produced by resistor R_1 and any signal at frequencies above the pole of the filter $(1/2\pi R_1 C_2)$ with an attenuation equal to $1/\sqrt{1 + (\omega R_1 C_2)^2}$. In our measurements C_2 was chosen to be 1.8 pF, but in practice the capacitance measured across R_1 varied between 3 pF and 4.5 pF due to the capacitances present on the circuit board used, leading to the reduction in measured noises at higher frequencies. The models used in this chapter reflect these measured values. This simple analysis ignores the effects of the finite bandwidth of the op-amp, where the open-loop gain reduction at high frequencies must be taken into account. This, however, is acceptable in this case as the noise gain here is not affected by the smaller open-loop gain at high frequencies [59].

The analytical expression for the voltage noise of this circuit in Equation 4.4 was compared to a direct measurement. In the voltage noise measurement, and all other noise measurements described in this chapter, a Hewlett-Packard 35665A Dynamic Signal Analyser was used to measure the voltage noise directly from the output of the circuits. It had a measurement sensitivity down to ~ 20 $n\mathrm{V}/\sqrt{\mathrm{Hz}}$. In order to eliminate as far as possible environmental background noise, the circuits under test were contained in aluminium boxes of wall thickness's of approximately $5mm$

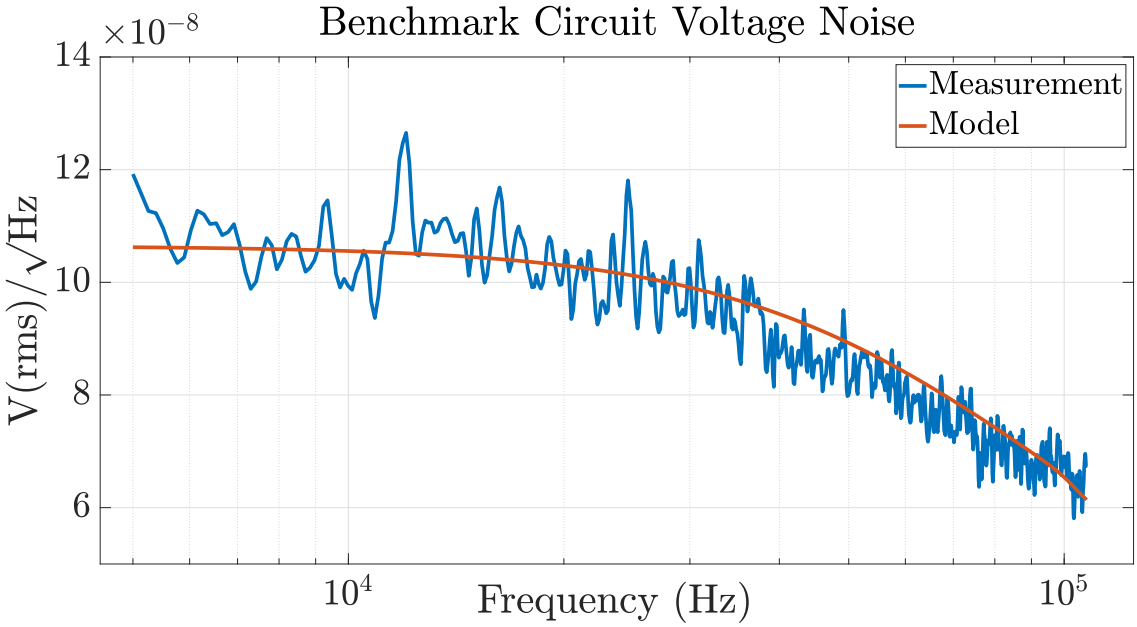

Figure 4.5: The voltage noise measurement of the benchmark circuit in Figure 4.4 and associated analytical noise model from Equations 4.3 and 4.4 using the same components as the measurement.

and were powered by batteries. The circuit was designed to optimise the noise performance for our displacement transducer ignoring the effects of any stray-capacitances [33]. This leads to a design with low current noise and therefore large values of feedback resistance R_1. The following component values were chosen for the benchmark circuit: capacitor C_1 was 3.5 pF, C_2 was 1.8 pF, the resistor R_1 was 620 $k\Omega$ and the op-amp used for U_{1A} was a LTC6244HV. This op-amp was chosen due to its low noise, large gain bandwidth and fast slew rate. These values approximately match those that will be used in the detection circuitry for the capacitive sensor in the experiment where the modulation frequency is set to 100 kHz [33]. The measurement and model are compared in Figure 4.5. At 100 kHz the voltage noise is approximately 67.9 $n\text{V}/\sqrt{\text{Hz}}$.

It is interesting to note that there is a peak in the noise plot in both Figure 4.5, and later in Figure 4.13, at about 12 kHz and must be due to some residual leakage of RFI into the set-up shown in Figure 4.3. Our models only look at the voltage noise inherent in the circuits alone as the Equations 4.3 - 4.5 suggest, and so we are not expecting to be able to predict and model the local interference in our laboratory. Despite this, the simple analytical model describes the noise

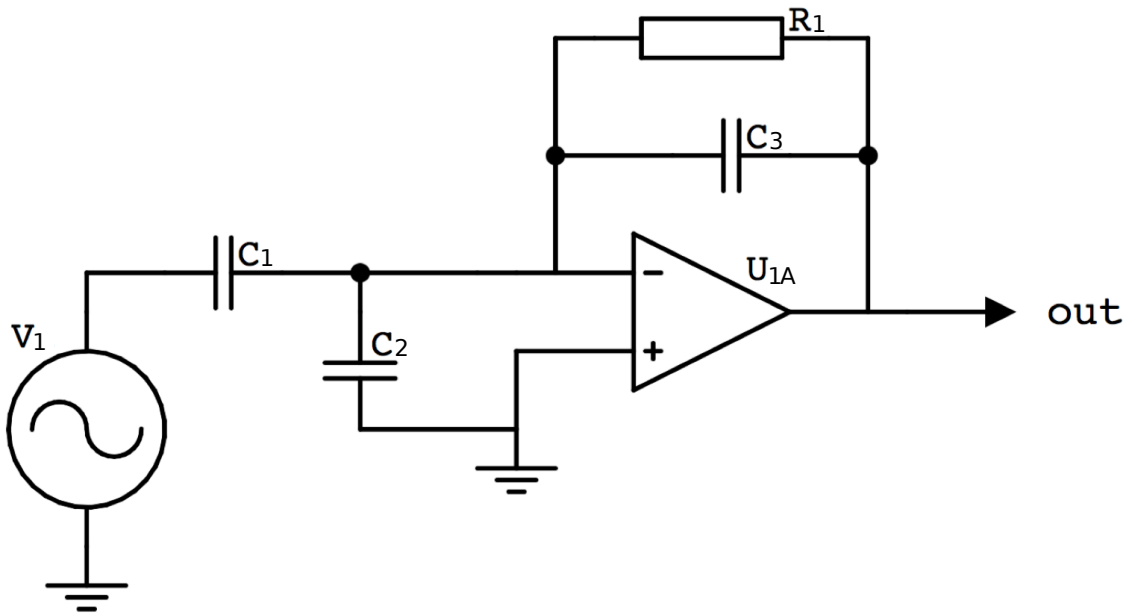

Figure 4.6: A diagram of a circuit (circuit B) which models a stray-capacitance through the capacitor labelled C_2.

well.

4.3.2 Stray-Capacitance Circuit

As a first attempt to model the effect of the stray-capacitance due to a cable we use a capacitor, labelled C_2, which is connected to ground as shown in Figure 4.6. We refer to this circuit as circuit B. The noise gain for circuit B is altered from that of the circuit in Figure 4.4 as the input impedance now comes from capacitors C_1 and C_2 in *parallel*. An equivalent noise circuit for the noise gain in Figure 4.6 is shown in Figure 4.7.

The noise gain for the circuit in Figure 4.6 is given by the following

$$G = \frac{i\omega R_1(C_1 + C_2)}{1 + i\omega C_3 R_1} + 1. \tag{4.6}$$

A derivation of this equation is given in Appendix B. In general $C_2 >> C_1$ and this leads to a large increase in noise gain. Inserting this new noise gain into Equation 4.4 gives an analytical expression for the voltage noise for circuit B. Unlike the case of the benchmark circuit in Figure 4.4, the finite bandwidth of the op-amp was taken into account here [59]. This predicted noise was

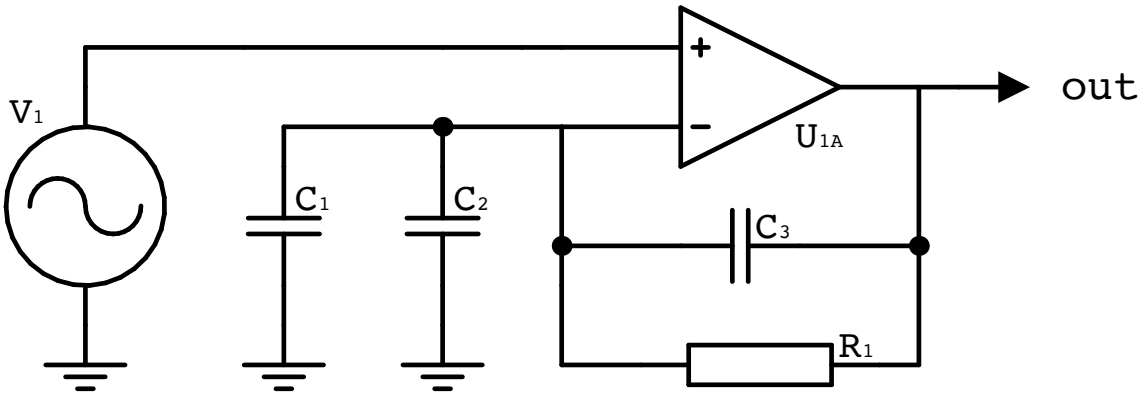

Figure 4.7: A diagram of the equivalent noise circuit from Figure 4.6, where the numbered components remain the same.

compared to direct measurement using the method mentioned previously. In measuring the noise of circuit B, repeated components from Figure 4.4 were kept the same and C_2 was 1.8 nF which matched approximately the stray-capacitance of coaxial cable of the type used in our experiment at a length of 3.5 m. The measurement and model are compared in Figure 4.8. At 100 kHz the voltage noise is approximately 3.8 $\mu\text{V}/\sqrt{\text{Hz}}$. The simple analytical model describes the noise well.

4.3.3 Buffer Op-Amp Feedback Circuit

A common method for reducing the effects of stray-capacitance is shown by the circuit in Figure 4.9 labelled circuit C [60, 61]. In this situation a buffer op-amp, labelled U_{2A}, is used in a feedback loop to drive both sides of the capacitor, C_2, to the same voltage. In principle this should remove the effects of stray-capacitance. While this method has been shown to eliminate the bias capacitance due to the cable and the instability in circuits with large stray-capacitances, depending on the choice of op-amps used [62, 63], it does not improve noise performance.

The output noise of circuit C was measured using the method mentioned previously; the component values and types were identical to those in Figure 4.6. The buffer op-amp U_{2A} was initially chosen to be an OP07. An analytical model for the voltage noise at the output of this circuit can be derived by considering the noise introduced across capacitor C_2 from the op-amp U_{2A} in Figure 4.9. The

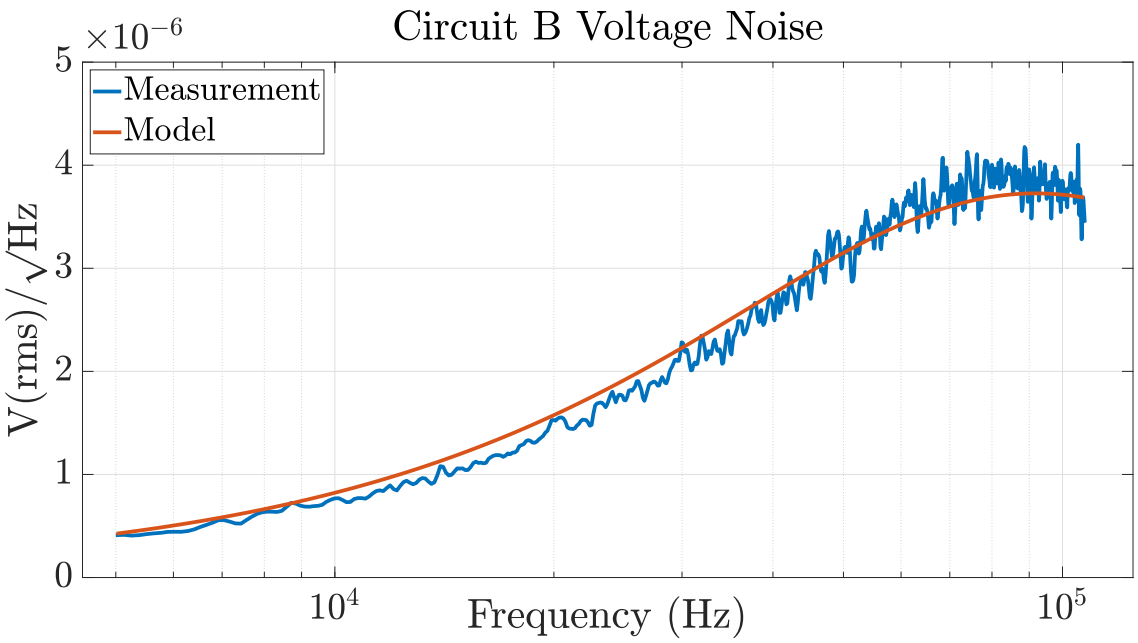

Figure 4.8: The voltage noise measurement of the stray-capacitance modelling circuit (circuit B) in Figure 4.6 and associated analytical noise model from Equations 4.4 and 4.6 using the same components as the measurement.

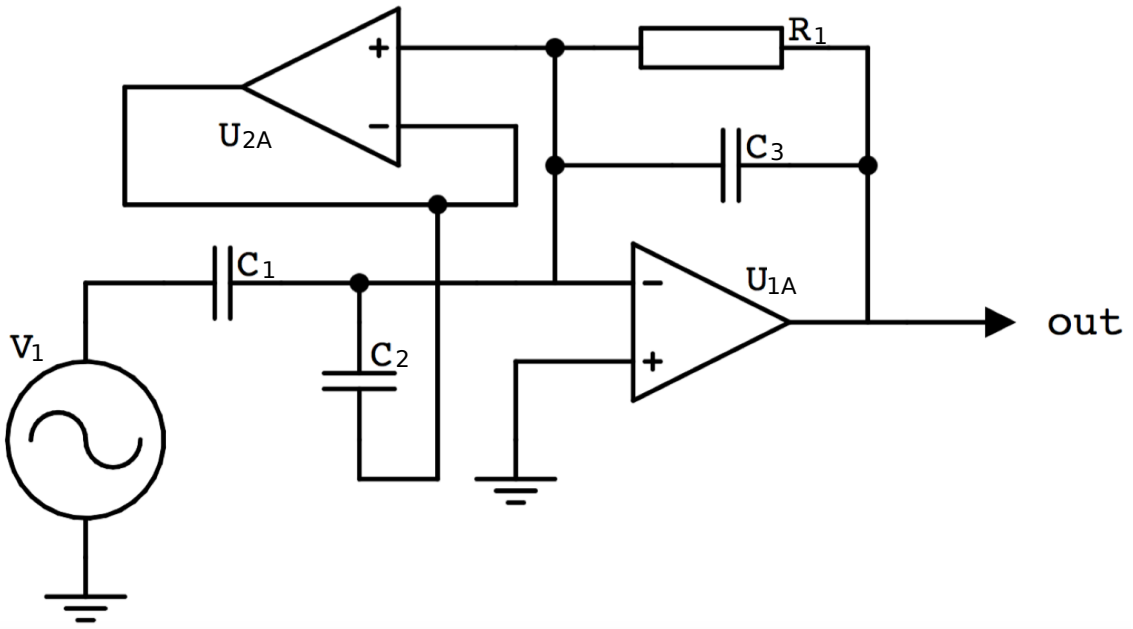

Figure 4.9: A diagram of a circuit (circuit C) using the common feedback technique of a buffer op-amp, for reducing the effects of stray-capacitance from the capacitor C_2.

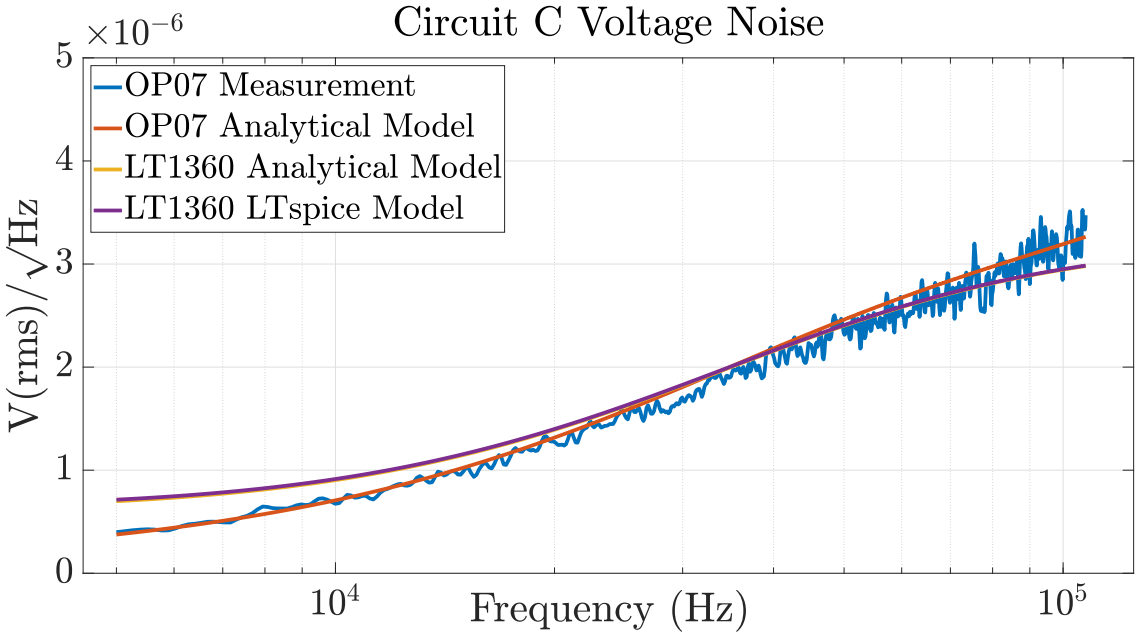

Figure 4.10: The voltage noise measurement of circuit C in Figure 4.9 and the associated noise model from Equation 4.7. Also included are analytical and LTspice models using a LT1360 op-amp rather than the OP07, where these curves completely overlap over the given frequency range.

total voltage noise, V_{2T} $(\mathrm{V}/\sqrt{\mathrm{Hz}})$, introduced is given by the equation

$$V_{2T} = \frac{V_{2n} R_1 F}{Z_s} \tag{4.7}$$

where V_{2n} is the buffer op-amp's voltage noise in units of $(\mathrm{V}/\sqrt{\mathrm{Hz}})$, and Z_s is the impedance of capacitor C_2. R_1 is the resistance value in the circuit and F is the low-pass filter term from Equation 4.4 which at 100 kHz is 0.55. In practice the pole of F would be at higher frequencies where it would not attenuate any signal.

The voltage noise measurement and model are shown in Figure 4.10. At 100 kHz the voltage noise is approximately 3.0 $\mu\mathrm{V}/\sqrt{\mathrm{Hz}}$. Also shown in Figure 4.10 is the analytical model and LTspice result for the LT1360, as U_{2A}, which is an operational amplifier with a faster slew rate and lower voltage noise density than the OP07. The LT1360 analytical and LTspice model curves completely overlap over the given frequency range. Using this op-amp the voltage noise is reduced to approximately 2.9 $\mu\mathrm{V}/\sqrt{\mathrm{Hz}}$ at 100 kHz. The analytical model describes both the measured and LTspice predicted noise spectra well.

This analysis shows that the presence of the buffer op-amp U_{2A} can contribute a significant amount of output voltage noise to the circuit, as the stray-capacitance, C_2, will couple the noise to the signal carrying core [64]. It also suggests that the similarity between the noise measurements in Figures 4.8 and 4.10 is coincidental. Where for Figure 4.8 the increased noise comes from the op-amp voltage noise being multiplied by the large noise gain, and for Figure 4.10 it arises from the feedback op-amp voltage noise being introduced across the stray-capacitance.

4.3.4 Proposed Noise Gain Modification Method

Figure 4.10 shows clearly that the conventional solution to the problem of stray-capacitance, which although allows a circuit to operate in a stable and accurate manner, gives an increased voltage noise. The goal is then to reduce the effects of stray-capacitance on the stable operation of a transimpedance circuit, while maintaining as low a circuit noise as possible compared to the benchmark circuit.

One way to do this is to reduce the noise gain of the circuit. This can be done by using the set-up shown in Figure 4.11, whose equivalent noise circuit for the noise gain is shown in Figure 4.12. In this circuit, labelled circuit D, the signal gain is the same as for the benchmark circuit in Figure 4.4, but now the noise gain is altered from Equation 4.6 to the following

$$G = \frac{i\omega R_1(C_1(C_2+C_3)+C_2C_3)}{(1+i\omega C_4R_1)(C_2+C_3)} + 1. \tag{4.8}$$

A derivation of this equation is given in Appendix B. This change is due to the introduction of the capacitor labelled C_3, which is in *series* with the stray-capacitance C_2. If $C_3 << C_2$, then Equation 4.8 reduces to Equation 4.3 which is the benchmark best-case scenario.

When this new noise gain is used with the general noise formula given in Equation 4.4, we obtain an expression for the voltage noise of this new circuit. The noise of circuit D was measured using the method mentioned previously. Repeated components from Figure 4.6 were as before and C_3 was 1.8 pF. The measurement and model are compared in Figure 4.13. At 100 kHz the voltage noise is approximately 68.8 $n\text{V}/\sqrt{\text{Hz}}$. As with the previous noise measurements, the model matches the

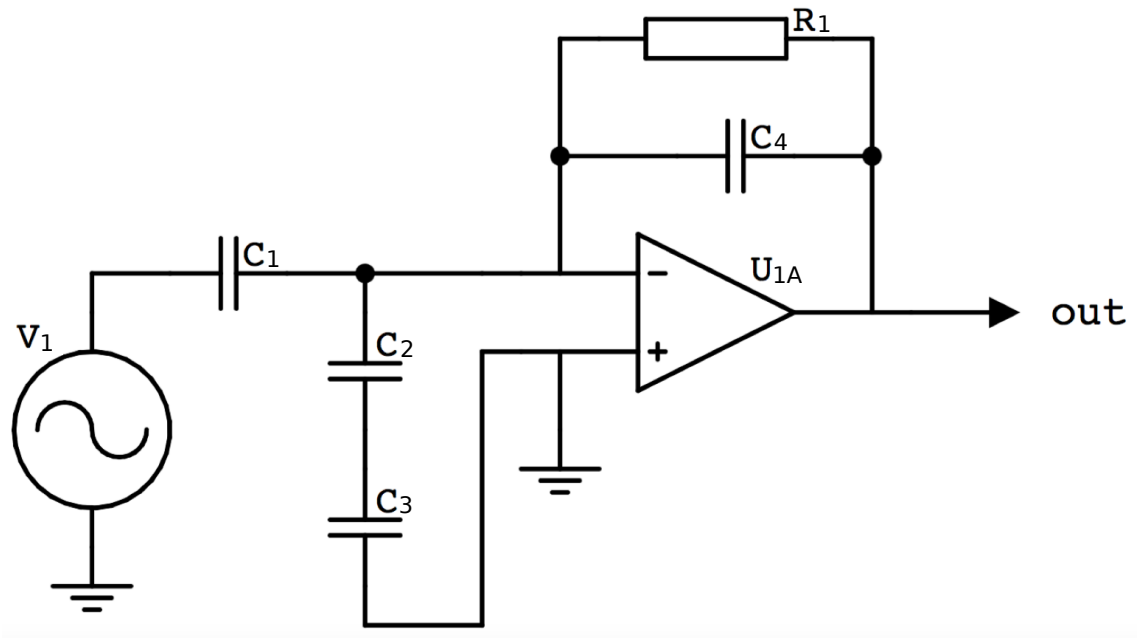

Figure 4.11: A diagram of a test circuit (circuit D) which modifies the noise gain to offset the effects of the stray-capacitance from capacitor C_2.

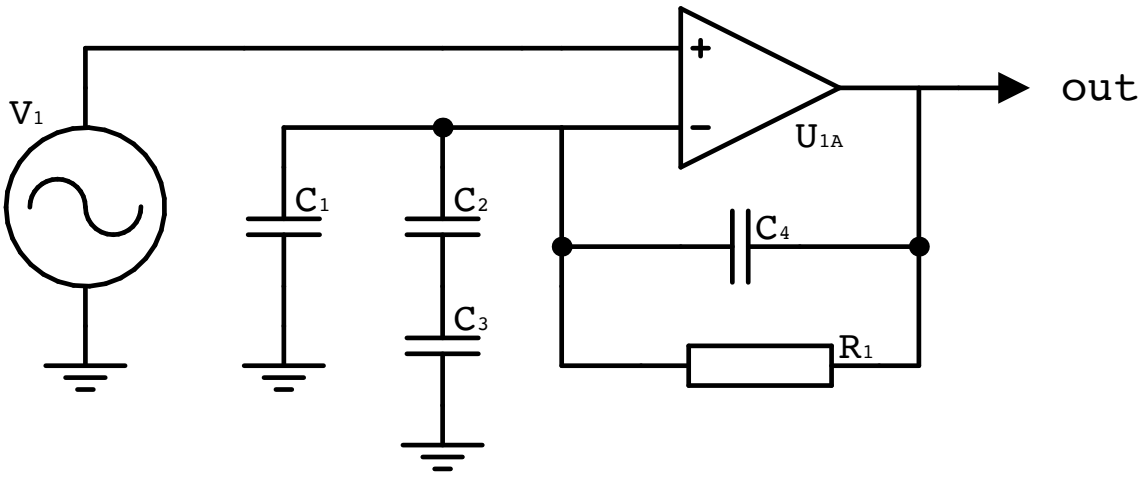

Figure 4.12: A diagram of the equivalent noise circuit from Figure 4.11, where the numbered components remain the same.

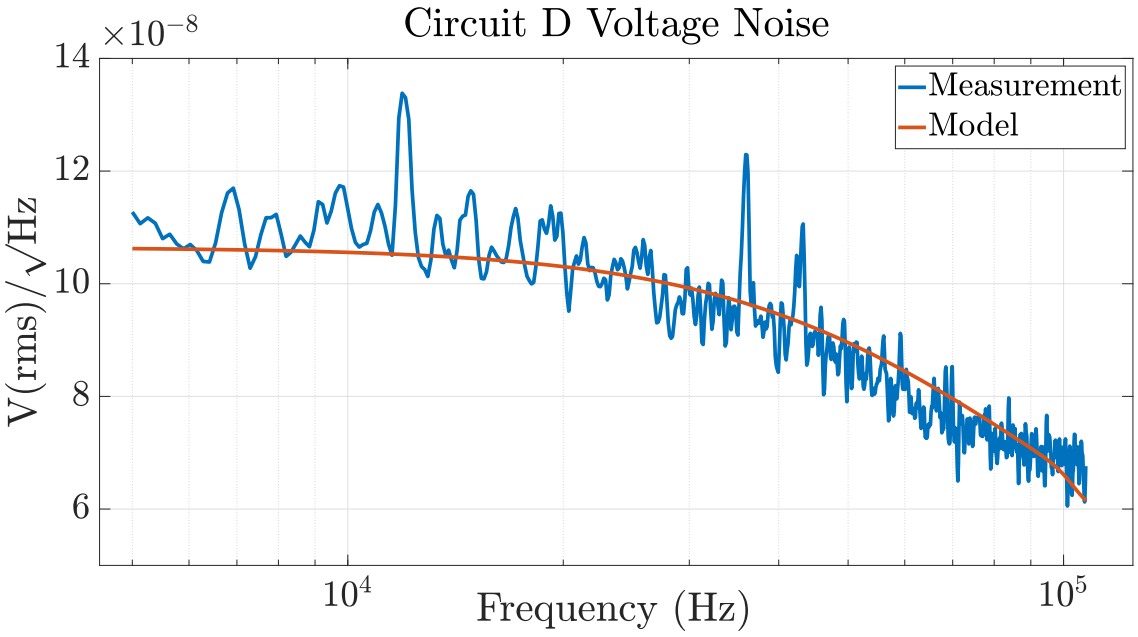

Figure 4.13: The measured voltage noise of the circuit where the noise gain has been modified as shown in Figure 4.11 (circuit D). This is compared to the predicted noise from Equations 4.4 and 4.8 using the same component values as the measurement. Notice that this is nominally the same as Figure 4.5.

measured voltage noise well.

4.4 Shield Effectiveness

For our candidate circuits it was important to quantify the effectiveness of the coaxial cable in shielding the signal carrying wire from environmental electromagnetic interference. This was done using circuits B and D, as circuit B is the typical shielded scenario and circuit D represents our method where the shield is now floating with respect to ground and as such is less effective. For circuit D the shield was floated at one end of the cable only, adjacent to the pre-amplifier circuit itself, the rest of the shield was not electrically connected to any other point. The in-situ cables in our experiment were attached to the inputs of these two circuits whilst they were located in our laboratory. This allowed a direct comparison of the output noise to be made under lab conditions. A measurement was also made with the benchmark circuit but with an unshielded cable at the input to the op-amp, to give a reference noise for the background interference. A very important feature to note here is that the majority of the length of cables involved were inside a large metallic cryogenic dewar (which was electrically floating with respect to the circuits under test through a 1.8 pF capacitor to ground) which would have provided extra shielding regardless of whether the coaxial shield was floated or not. This is typical for any cryogenic experiment and so is a fair comparison.

These measurements, along with the test measurement of circuit D from Figure 4.13 for comparison, are shown in Figure 4.14. This figure shows that although there are significant interference noise peaks at certain frequencies for the in-situ circuit D, overall there is a much lower noise floor compared to the in-situ circuit B implying that the lowering of noise gain is worth the reduction in electromagnetic interference shielding. Also the no-shield scenario is shown to be a non-viable alternative to the problem of parasitic capacitance from shields. At 100 kHz the in-situ circuit D noise is approximately 3.1 times larger than the test circuit D case. Aside from interference, additional noise creating this disparity between scenarios could arise from unaccounted for parasitic capacitances within the experimental set-up. As already stated, our set-up of course benefited

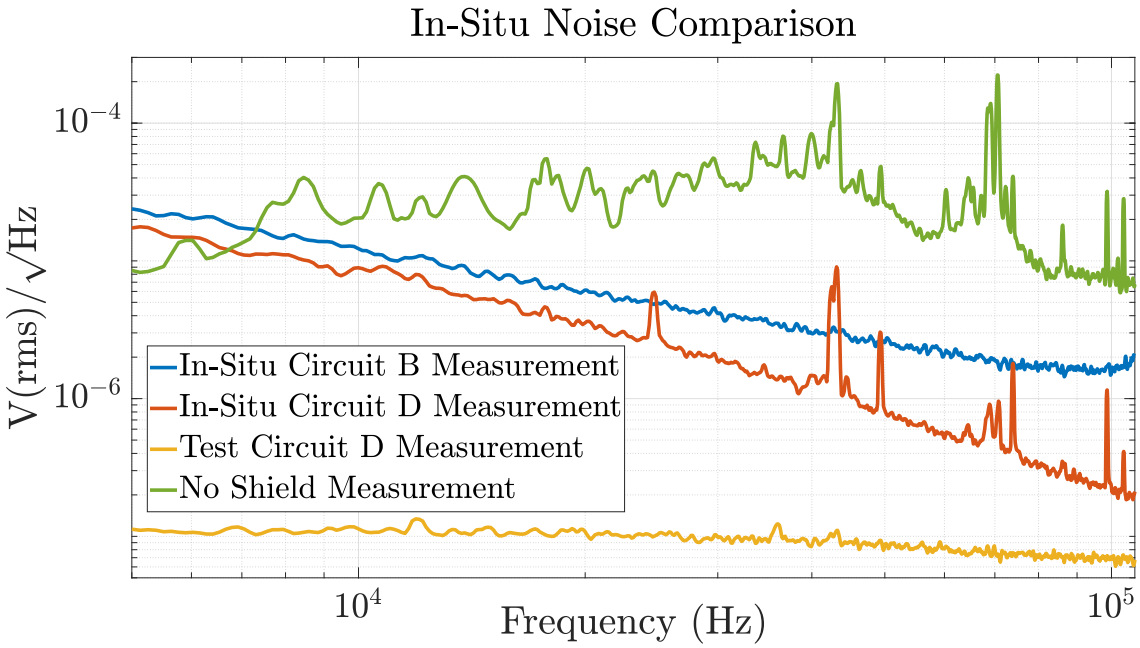

Figure 4.14: Real coaxial cable voltage noise measurements of circuits B and D compared to an unshielded cable benchmark circuit and the test circuit D noise measurement.

from the fact that for the in-situ measurements, the majority of the cabling was contained inside a cryogenic dewar, which would have provided additional shielding.

4.5 Summary

A summary of the voltage noises at 100 kHz for the benchmark circuit, and circuits B, C and D from Figures 4.4, 4.6, 4.9 and 4.11 respectively, is listed in Table 4.1. The same is done for the in-situ circuits B and D as well as the no-shield circuit from Figure 4.14 for comparison.

These noise values have been converted into displacement noises in the table for comparison to the required displacement sensitivity for the Superconducting Torsion Balance of 32 $p\text{m}/\sqrt{\text{Hz}}$ from Equation 3.8 in Section 3.1.3. This is to highlight the projected physical sensitivities of these circuits based on the specifications of our experiment. The conversion from voltage noise to displacement noise is described in Appendix C.

A comparison between the analytical noise models of circuits B and D, from Equations 4.6 and 4.8,

Table 4.1: A summary of the voltage noise results at 100 kHz for the benchmark circuit, and circuits B, C, D. The in-situ measurements are also included.

Circuit	Voltage Noise ($n\mathrm{V}/\sqrt{\mathrm{Hz}}$)	Disp. Noise ($p\mathrm{m}/\sqrt{\mathrm{Hz}}$)
Benchmark Circuit	67.9	6.6
Circuit B	3767.0	364.1
Circuit C OP07	3048.0	294.6
Circuit C LT1360	2940.0	284.2
Circuit D	68.8	6.6
In-Situ Circuit B	1665.0	160.9
In-Situ Circuit D	214.8	20.8
In-Situ No-Shield	8059.0	778.9

and Figures 4.8 and 4.13 respectively, with LTspice noise models of the same circuits using the same components is shown in Figure 4.15. These circuits were chosen for the comparison as they display the largest difference in voltage noise for the given circuit configurations described in the text, and as the circuit C noise measurement and models shown in Figure 4.10 already has a comparison with a LTspice model. It can be seen in Figure 4.15 that both sets of models agree very well with one another over the given frequency range, and as such they both agree well with the respective noise measurements.

4.6 Discussion

The voltage noise from a variety of pre-amplifier circuits for non-resonant capacitive sensors has been measured and modelled in order to explore the negative effects of large stray-capacitances at their inputs. Five different test circuits were compared: one was a standard pre-amplifier that was optimised for our application with no stray-capacitance (Benchmark circuit); one was the standard pre-amplifier but now with stray-capacitance (circuit B); another two employed active feedback to

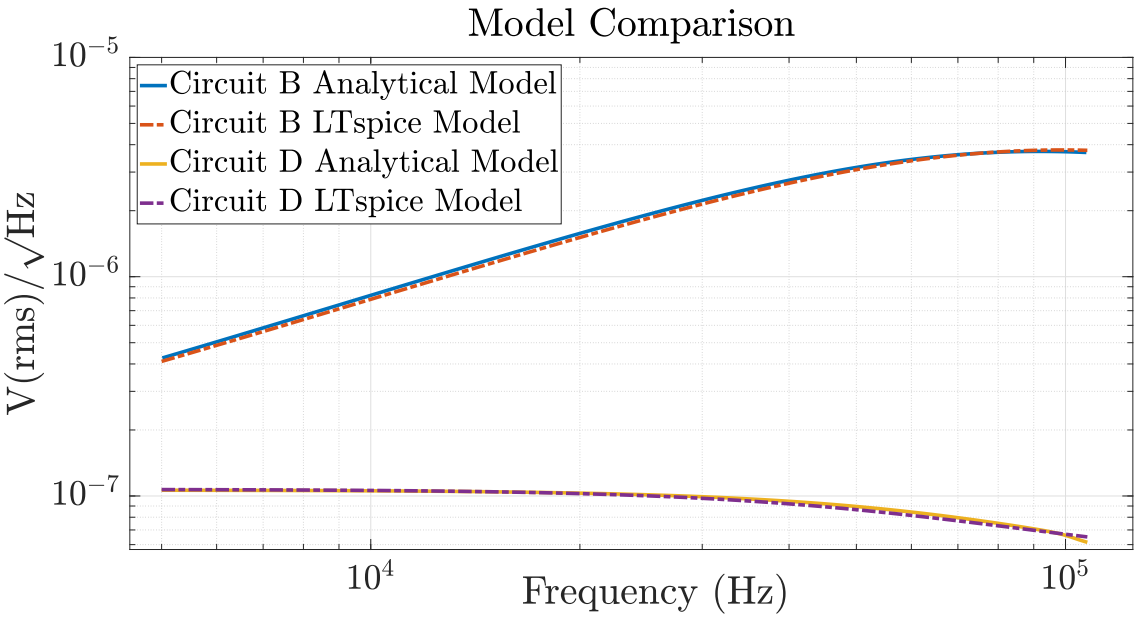

Figure 4.15: A comparison of the analytical noise models of circuits B and D, from Figures 4.8 and 4.13 respectively, with LTspice noise models of the same circuits using the same components.

maintain the cable shield at the voltage of the input to the op-amp (circuit C using two different amplifiers for the active feedback). Finally, a novel circuit (circuit D) was tested. A summary of the noise characteristics of these circuits is shown in Table 4.1. Circuit D had the best noise characteristics, along with the benchmark circuit, and is shown in Figure 4.11. The addition of a simple small capacitance, C_3, connecting the shield to the non-inverting input of the pre-amplifier reduces the noise gain that is produced by the low impedance of the shield. The voltage noise for this circuit is shown in Figure 4.13.

In-situ results indicate a modest increase in noise, by a factor of 3, due to environmental interference and the non-static capacitances present in our actual set-up. This increase is, however, still acceptable at the signal modulation frequency of 100 kHz. This indicates environmental interference is relatively benign in this situation and so the reduced shield effectiveness is not significant in this case. In our experiment this is due to the fact that the signal carrying coaxial cable is mostly inside a cryogenic dewar which is effectively a Faraday cage and a shield against high frequency magnetic fields. Clearly standard modulation/demodulation schemes can mitigate against low fre-

quency interference if it does not overwhelm the pre-amplifier. The degradation in the measured shielding effectiveness is not equivalent to there being no shield at all, as shown in Figure 4.14.

The required sensitivity of the Superconducting Torsion Balance was 32 $p\mathrm{m}/\sqrt{\mathrm{Hz}}$. From Table 4.1 it can be seen that the in-situ circuit D, the proposed design used in the experimental setup, has the required sensitivity at 20.8 $p\mathrm{m}/\sqrt{\mathrm{Hz}}$.

4.7 Conclusion

The proposed circuit is a trivial extension of the usual methods of designing a capacitive sensor circuit. However, as far as we are aware, it has not been proposed previously most likely due to the perception that it is incapable of providing shielding from environmental interference. The proposed technique could be successfully employed in many applications in addition to cryogenic experiments. For example, vacuum systems are employed in many sensitive experiments and would provide electromagnetic shielding from external noise sources. In general, however, there may be situations were interference is a dominant factor that determines a capacitive sensor's sensitivity. A particularly important case is when an unshielded drive signal at the input of a bridge circuit (V_1 in Figures 4.4, 4.6, 4.9 and 4.11) can couple directly to the pre-amplifier. In such cases a method for which the shield effectiveness is preserved should be employed.

One way to balance the benefits of a decrease in noise gain with the negatives of a reduction in shield effectiveness may be to make capacitor C_3 from Figure 4.11 a variable capacitor. This could allow the trade-off to be fine-tuned for more general applications, and may be a more general solution to the problem of stray-capacitance when external interference cannot be ignored and where fine cables are required to minimise the heat leak in a cryogenic experiment. In our case, placing the pre-amplifier circuit near the point where the coaxial cable leaves the cryogenic dewar further reduced interference and drove the voltage noise closer to the ideal value.

Finally, it may be useful to the reader if we compare the performance of the capacitive sensor presented here with, for example, a resonant capacitive sensor [55]. In general, the sensitivity

of capacitive sensors is proportional to the bias AC drive voltage applied to the electrodes, and inversely proportional to the equilibrium separation distance between the two sensing electrodes. For the resonant bridge transducer these parameters are 2.1 V_{pp} and 0.25 mm respectively [55]. Other factors such as capacitance plate area and drive frequency are important but strongly depend on each individual case as to what is practical. From Table I, the in-situ circuit D sensor has a displacement noise of 20.8 $p\mathrm{m}/\sqrt{\mathrm{Hz}}$ that would be expected to be about 15.0 $p\mathrm{m}/\sqrt{\mathrm{Hz}}$ after coherent demodulation, whereas the resonant bridge transducer has a noise floor of approximately 1.0 $p\mathrm{m}/\sqrt{\mathrm{Hz}}$ above 1 Hz [55]. We can estimate an approximate sensitivity of our detector if we employed the same gap and drive voltage as that for the resonant sensor. These parameters can be easily modified in our design. We then find that our device would be a factor of about 7 less sensitive. Nevertheless we believe the simplicity of the transimpedance scheme that we have presented here has its merits. Further our device has been demonstrated in a cryogenic setting and has sufficient sensitivity for our application [33].

Chapter 5

The Air Bearing

Blessed are the legend-makers with their rhyme, of things not found within recorded time.

J. R. R. Tolkien

The text and figures of this chapter are copied from the paper 'An Air Suspension to Demonstrate the Properties of Torsion Balances with Fibres of Zero Length' [29], of which I was an author along with my supervisor Clive Speake. I took all the measurements reported in the paper, and Clive developed the model of the statics of the air suspension setup described therein. Derivations of some of the mathematical results in this chapter have been expanded upon in the appendices.

In this chapter the design and characterisation of an air-bearing suspension that has been constructed to highlight the properties of torsion balances with fibres of zero length is reported on, as described in Chapter 2. A float was levitated on this suspension and its rotational and translational motion in the horizontal plane of the laboratory was controlled using magnetic actuators. The in-situ electromagnetic tuning of the float's centre-of-buoyancy to an accuracy of $\pm$ 0.3 mm is demonstrated, which was limited by the noise in the air bearing. The rotational stiffness of the float, which was approximately zero by design, is also measured. The observed behaviour of the float is compared with the predictions of a detailed model of the statics of the float-actuator

system. Finally, the application of these ideas and results to the construction of sensitive devices for the measurement of weak forces with short ranges is discussed.

5.1 Introduction

As stated in Chapter 1 torsion balances have a long history in experimental science, stretching back to the time of Cavendish [1], and that in modern physics torsion balances are used extensively in tests of the inverse square law of gravity [4, 5], as well as for Casimir force measurements [65] and tests of the weak equivalence principle [66]. The advantage of the torsion balance is that well-manufactured fibres have very low rotational stiffness giving a high sensitivity, and well-designed balances can be made such that, to some degree, tilt or horizontal acceleration due to seismic noise will not couple to rotational motion of the suspended mass (or bob) [67]. Despite these advantages the traditional torsion balance design has some limitations, particularly when it is employed to detect forces within sub-millimetre ranges. Due to the vertical distance of the centre-of-mass from the point of attachment, horizontal accelerations, due to micro-seismic motion for example, can couple strongly to the simple pendulum mode. This makes control of the torsion bob difficult. Also at some level there will always be some coupling of tilt to rotational motion [68]. Issues also face low-frequency torsion pendulum experiments where ground vibration and other sources of Newtonian noise become increasingly problematic [69, 70]. Tilt-rotational mode coupling is also a concern for seismic inertial sensors [71]. In addition to weak-force measurements, the co-location of the centres-of-mass and buoyancy of a suspended mass is a crucial feature of horizontal accelerometers and tiltmeters [72, 73]. This is currently achieved only by the adjustment of small masses such as lockable screws.

The goal then is to create a device that shares the advantages of the torsion balance, but is not limited by the drawbacks mentioned above, where necessary adjustments to the centre-of-buoyancy can be achieved accurately and remotely irrespective of the device's environment. In a previous paper [27], it was shown how the stiffness of the actuators acting on a levitated object (referred to as a float) could be tuned in-situ in such a way that the centre-of-buoyancy of the levitation

system could be altered to lie at the centre-of-mass of the float, and that the rotational stiffness could be tuned, ideally, to zero. This could all be achieved whilst simultaneously controlling the translational degrees of freedom. The centre-of-mass is the point where inertial forces act, whereas the centre-of-buoyancy is the location of the resultant of the forces that are applied to levitate the float. In the general case the centre-of-mass will not lie at the centre-of-buoyancy due to manufacturing imperfections and non-uniform densities of engineering materials and so horizontal accelerations and tilts will couple to the rotational mode of the device. The classical torsion balance has an in-built low sensitivity to tilt and horizontal acceleration as the centre-of-buoyancy of the torsion bob can lie to a good approximation on the rotational axis. In the previous paper [27], some initial results of measurements of the tuning of the period of oscillation of a float suspended by perfect diamagnetism (superconductivity) were presented. In this chapter the focus is on the demonstration of the precise tuning of the centre-of-buoyancy of a float.

We have constructed an air suspension, referred to here as the air bearing [74], that levitates the float. The float is then controlled in the horizontal plane of the laboratory by magnetic actuators which consist of coil-magnet pairs. By changing the currents in the coils we can tune the centre-of-buoyancy of the float. We present measurements which support this concept, suggesting that torsion balances with fibres of zero length can indeed be tuned in-situ to be rotationally decoupled from ground tilt and horizontal accelerations. The actuators were designed such that the rotational stiffness of the float was nominally zero. Without further tuning the magnitude of the rotational stiffness was experimentally found to be lower than that of the torsion balance used in a recent determination of Newton's constant of gravitation [75].

5.2 Theory

In our previous publication we derived expressions for the rotational stiffness and centre-of-buoyancy shift for superconducting and electrostatic suspensions [27]. Here we give the corresponding expressions for a system that uses electromagnetic actuators.

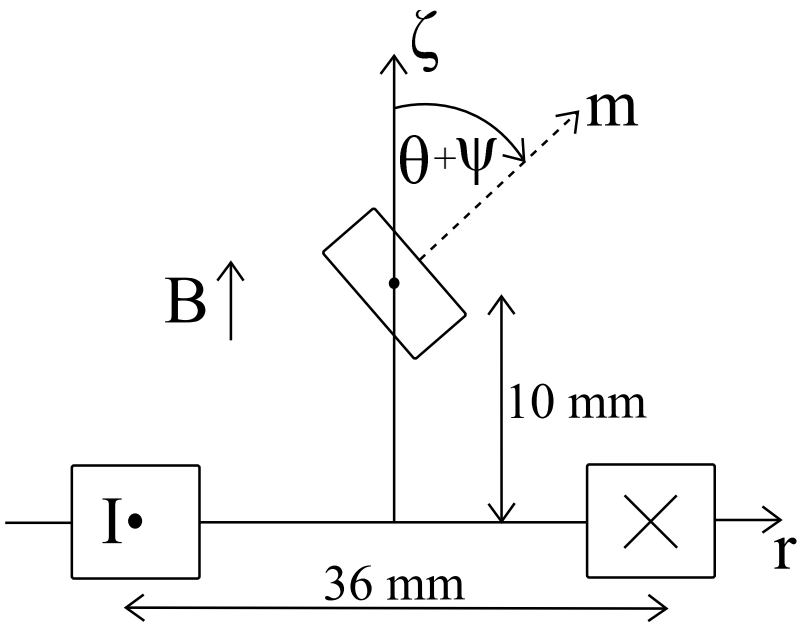

Figure 5.1: A schematic diagram of a magnet with a magnetic dipole moment, m, at an angle, $\theta + \psi$, to a magnetic field, B, produced by a coil with current I. The coil has a cross-sectional area of 7.2×10^{-5} m^2.

Consider Figure 5.1, where a magnet with dipole moment, m, lies in a magnetic field produced by a coil with current I. The magnetic field on the axis of a coil of negligible cross-section can be described by the following [76],

$$B_\zeta = \frac{\mu_0 R^2 I}{2(R^2 + \zeta^2)^{\frac{3}{2}}}, \tag{5.1}$$

where μ_0 is the vacuum permeability constant, R is the radius of the coil and ζ is the axial distance between the coil and magnet centres, as described by the coordinates in Figure 5.1. We can integrate this expression over the dimensions of the real coils to find the field and its derivatives. If we assume that the magnetic field is uniform over the dimensions of the magnet, we can write its potential energy in terms of its magnetic dipole moment,

$$U = -\vec{m} \cdot \vec{B} = -mB_\zeta \cos(\theta + \psi), \tag{5.2}$$

where θ is a fixed angle between the dipole moment and the ζ- axis and ψ is a small angle whose mean is zero, as indicated in Figure 5.1. We ignore changes in the axial force due to small radial displacements and rotations of the magnet. For $\psi = 0$ the force on the magnetic moment is given

by

$$F = -\frac{\partial U}{\partial \zeta} = m\frac{\partial B_\zeta}{\partial \zeta}\cos\theta. \tag{5.3}$$

Taking the magnetic field to be a maximum at the centre of the coil, $\partial B_\zeta/\partial\zeta$ is negative, so for a magnetic moment that is aligned with the field the force will be attractive and reach a maximum negative value at some axial distance. The stiffness in the ζ direction is given by

$$k_{\zeta\zeta} = -\frac{\partial F}{\partial \zeta} = -m\frac{\partial^2 B_\zeta}{\partial \zeta^2}\cos\theta. \tag{5.4}$$

In order for this stiffness to be positive, leading to a passively stable system, we need the product of the cosine term and $\partial^2 B_\zeta/\partial\zeta^2$ to be negative. At the peak force $\partial^2 B_\zeta/\partial\zeta^2$ is zero, so in principle, we can choose the sign of the linear stiffness by selecting the axial location of the magnet. If the magnet is closer to the coil than the location of the peak force (where $\partial^2 B_\zeta/\partial\zeta^2 < 0$) and $\theta = 0$, we can achieve a stable system. Equally we can achieve a stable system by selecting a position of the magnet that is further away from the coil than the peak force position and $\theta = \pi$. Now consider the angular stiffness given as, again in the case where $\psi = 0$,

$$k_{\theta\theta} = \frac{\partial^2 U}{\partial \theta^2} = mB_\zeta\cos\theta. \tag{5.5}$$

Clearly here the choice of θ will also determine the stability of the system. We will see below, where we consider the stiffness of the float given by the actuators that control it, that it is advantageous to make the angular stiffness negative and we therefore select $\theta = \pi$. If we desire a system that is stable for linear motion, according to Equation 5.4, we therefore need to position the magnets further from the coils than the position of maximum force. This is turn implies that the force between the magnet and coil is repulsive. We should note that any unstable system can be servo-controlled, however in practice servo control is more easily achieved with an intrinsically stable system.

Now we consider our experimental setup with 8 such coil-magnet pairs arranged around the float as shown in Figure 5.2. (with a new global coordinate system). We can now define the potential energy of a single magnet/coil pair in terms of the coordinates and angles given in Figure 5.2, say for magnet 5 and coil e. We define the separation of the magnet from its opposing coil that is due

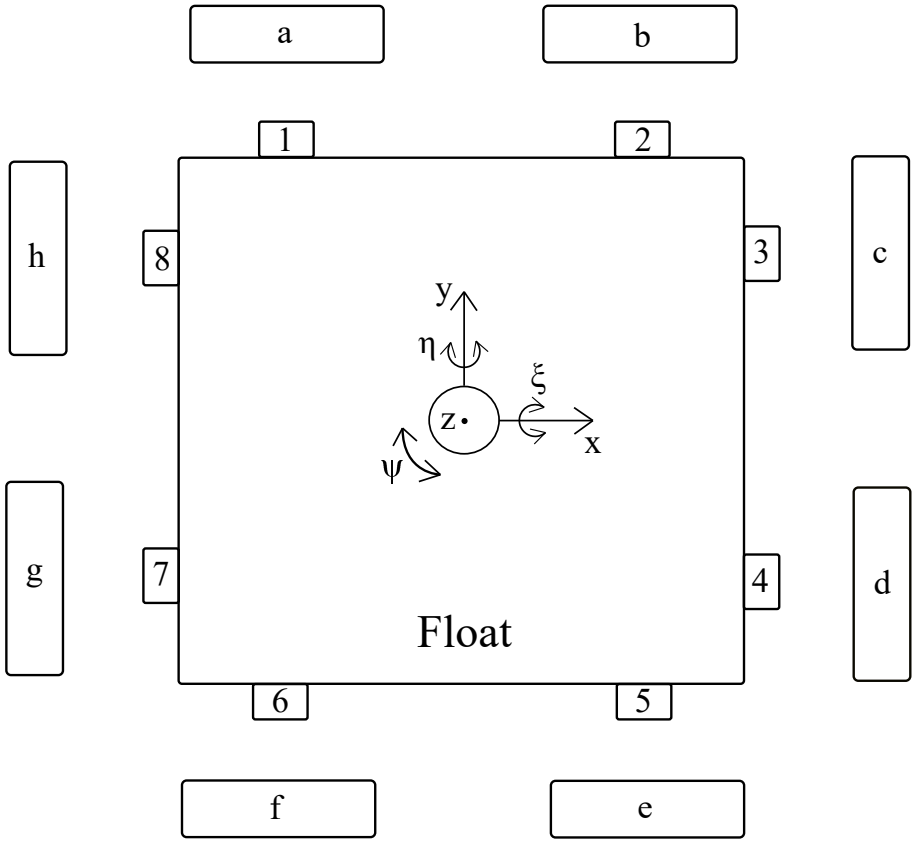

Figure 5.2: A plan view schematic drawing showing the float, coils 1-8 and magnets a-h. New global coordinates centred on the float are defined: the x and y axes in the horizontal plane, and the z-axis normal to this plane, with rotation around these axes.

to the rotation of the float, ψ, as $f(\psi)$. The separation due to its simple translation is defined as y, which is along the y-axis in Figure 5.2. Figure 5.3 highlights the changing separation of this magnet and coil and the relevant geometric terms. We can therefore define

$$\zeta = f(\psi) + y, \tag{5.6}$$

for this magnet/coil pair, and it can be easily shown from Figure 5.3 that

$$f(\psi) = b - a\cos\psi + x_0 \sin\psi. \tag{5.7}$$

The potential energy of the magnet/coil pair can then be written,

$$U = -mB\left(f(\psi) + y\right)\cos\left(\theta + \psi\right), \tag{5.8}$$

where we have dropped the subscript ζ on the magnetic field. This can be applied to any magnet/coil pair with a suitable change in coordinates. We have used a similar nomenclature as in [27] and, on comparing Equation 5.6 with Equation 16 for $g(\psi)$ in [27], we note that the magnetic/coil actuators are qualitatively different from the superconducting and electrostatic actuators previously discussed. This is because the points of application of the forces to the float (the magnets) by the coils now move with the rotation of the float rather than being defined by the fixed location of the coils. It is convenient to express the magnetic field as a Taylor series around the equilibrium position where we define the equilibrium spacing between the magnet and coil as g_0. The magnetic field can then be written,

$$B = B_0 + \left(\frac{\mathrm{d}B}{\mathrm{d}\zeta}\right)_{g_0} \cdot \left(f(\psi) + y - g_0\right) + \frac{1}{2}\left(\frac{\mathrm{d}^2 B}{\mathrm{d}\zeta^2}\right)_{g_0} \cdot \left(f(\psi) + y - g_0\right)^2. \tag{5.9}$$

By substituting this into Equation 5.8 and setting $y = 0$ we can find the contribution to the total rotational stiffness of the float from one (the i^{th}) coil,

$$K^i_{\psi\psi} = \frac{\mathrm{d}^2 U}{\mathrm{d}\psi^2} = m\left(\frac{\mathrm{d}^2 B}{\mathrm{d}\zeta^2}x_0^2 + \frac{\mathrm{d}B}{\mathrm{d}\zeta}a - B_0\right), \tag{5.10}$$

where we have assumed again that the magnet is anti-aligned with the coil field. A derivation of this equation is given in Appendix D. The upper case notation for the stiffness constant refers to the complete float rather than an individual coil/magnet pair (as compared to Equations 5.4 and 5.5).

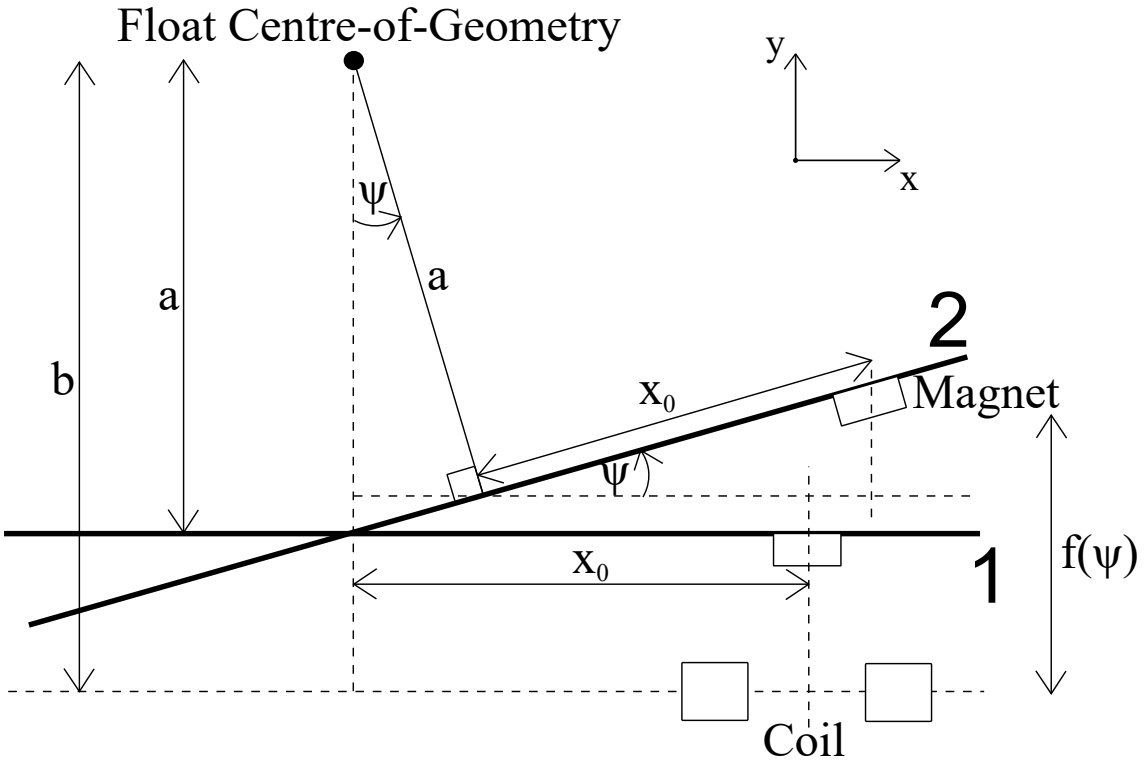

Figure 5.3: A diagram highlighting the geometry of the changing separation between magnet 5 and coil e (from Figure 5.2) as described in Equation 5.7. As the float rotates around its geometric centre from position 1 to position 2, the separation between the magnet and coil, $f(\psi)$, is a function of the amount of rotation, ψ. This is independent of any separation change due to simple translation, y, along the y-axis as described in Equation 5.6. The amount of rotation shown here is exaggerated for clarity, and as before we assume radial displacements along the x-axis are comparatively small and can be ignored. Here we have used a similar nomenclature as in [27].

We can see that in order to create a zero stiffness configuration we require that the quantities in the bracket sum to zero. Noting that in our configuration the second and third terms are both negative (see the discussion above regarding the signs of the derivatives of the magnetic field), in principle this is possible. However we did not pursue this in the work described here but chose a value of x_0 and the positions of the magnets relative to the coils in order to achieve a nominally zero stiffness. The total rotational stiffness is given as the sum of the terms in Equation 5.10 from all the actuators, which approximately multiplies it by a factor of eight. In Section 5.4 we compare measurements of float's rotational stiffness with this prediction.

We define the nominal centre-of-buoyancy (NCB) as the point in the horizontal plane where the moments of the all the forces acting on the float are zero when the coils carry their nominal currents. If we consider the x direction, the position of the centre-of-buoyancy with respect to the NCB of the float, x_{cb}, can be modified by changing the stiffnesses of some actuators relative to others. For example, using Equation 12 from [27] we have

$$x_{cb} = \frac{K_{y\psi}}{K_{yy}}. \tag{5.11}$$

The term in the denominator is the sum of the linear stiffnesses which are given for each coil by Equation 5.4. The term in the numerator is a cross-term from the stiffness matrix describing the static behaviour of the float and in the symmetrical case is zero. We can compute the individual contributions from each coil/magnet pair to this cross-term with the help of Equations 5.8, 5.7 and 5.9 to find

$$k_{y\psi} = x_0 m \frac{\mathrm{d}^2 B}{\mathrm{d}y^2}. \tag{5.12}$$

The change in centre-of-buoyancy in the x direction is then,

$$x_{cb} = \frac{K^a_{y\psi} + K^b_{y\psi} + K^e_{y\psi} + K^f_{y\psi}}{K^a_{yy} + K^b_{yy} + K^e_{yy} + K^f_{yy}}, \tag{5.13}$$

or

$$x_{cb} \approx x_0 \frac{\left(I^b + I^e - I^a - I^f\right)}{4I}, \tag{5.14}$$

where I is the average bias current in the coils labelled a, b, e and f in Figure 5.2 and clearly x_{cb} is proportional to the difference in the currents flowing in the respective coils. A derivation of this

equation is given in Appendix D. This implies the theoretical maximum accuracy to which the centre-of-buoyancy can be tuned in the case presented here depends on the precision with which the actuators' strength can be changed, which in turn depends on the current noise of the coil drivers.

When the bearing is tilted by an angle, ξ, from the horizontal, the total torque acting on the float from the actuators in order to maintain its position against the gravitational force component can be described by the following,

$$\Gamma = \kappa \frac{\Delta I}{4I} + Mg\xi \left(x_0 \frac{\Delta I}{4I} + x_{cm} \right), \tag{5.15}$$

where the first term in the brackets corresponds to x_{cb} as given in Equation 5.14, M is the mass of the float, g is the acceleration due to gravity and x_{cm} is the position of the float's centre-of-mass with respect to the NCB. Here κ represents the torque due to any asymmetry of the magnetic actuators and their positions around the float. In the ideal case the process we employ for changing the bias currents to tune the centre-of-buoyancy should not apply a torque, but in any real system such a term does exist. Any instability in the currents applied to the float to achieve a centre-of-buoyancy tuning will introduce noise into the actual measurement via the κ parameter, so clearly it is desirable to reduce its magnitude as much as possible. A similar expression to Equation 5.15 describes the centre of mass tuning in the y direction.

In order to measure the κ parameter and to check how the current tuning shifts the centre-of-buoyancy we need to eliminate x_{cm} from equation 5.15. We do this by adjusting the physical centre-of-mass using balance weights, as described below, until it coincides with the NCB. Then, dividing by the current ratio, we find

$$\tau = \Gamma / \frac{\Delta I}{4I} = \kappa + Mg\xi x_0. \tag{5.16}$$

This equation states that, if the torque on the float is measured over a range of tilt angles for a given set of bias currents in the coils, the torque due to the actuator asymmetry can be calculated at $\xi = 0$. Furthermore, it predicts a linear response of τ to the tilt angle. This gradient allows the change in centre-of-buoyancy described in Equation 5.14 to be experimentally determined. This

comparison was verified by experiment.

5.3 Experimental Setup

Our experimental setup consisted of 8 coil-magnet pairs; two on each side of the square shaped float as shown in Figure 5.2. The float and bearing were made of aluminium alloy. The coils themselves were based on the OSEM coils that have been developed for LIGO [77] and each consisted of 500 turns of copper wire and had a mean radius of 18 mm. The magnets used were grade N38 neodymium iron boron magnets with a magnetic dipole moment of 0.775 N·m/T and were cylindrical with a radius and depth of 5 mm. They were attached to the float using contact adhesive. The bearing's flat top surface consisted of 0.5 mm diameter holes in a 10 mm grid under the entire bottom surface of the float through which compressed air was pumped at a constant pressure to provide a lift force to the float.

Figure 5.2 gives a schematic drawing of the float, coils and magnets, with a coordinate system centred on the float. A summary of the dimensions of all the relevant components is given in Table 5.1, where the stated measurement uncertainty is used to propagate through to the uncertainties on all measured torques and stiffnesses in Section 5.4. The rotation of the float was measured with an optical lever arrangement with a laser reflecting off a small mirror attached to the centre of the float and a position sensitive photodiode. This diode and its associated electronic circuit was then connected to a computer via an ADC. The computer was connected to the coils through a DAC. This allowed the coil currents to be actively controlled via a PID control loop in LabVIEW software and hence the float was kept stable relative to a reference null position on the photodiode. A general diagram of this setup is shown in Figure 5.4.

A photograph of the float, bearing, micrometers, mirror, compressed air input, coils and magnets is shown in Figure 5.5. Figure 5.6 gives a schematic drawing of how the bearing can be tilted from the horizontal; where this can be done along the float's x and y axes in the horizontal plane. Tilt in the y-axis by a known tilt angle, ξ, is depicted in the figure.

Table 5.1: A summary of the various dimensions of the float, bearing and magnetic actuator setup. The dimension label corresponding to the equations in Section 5.2 is stated where applicable.

Parameter	Length (mm) $\pm$ 0.5 mm
Coil-Magnet Axial Distance (ζ)	10.0
Coil Mean Radius (R)	18.0
Coil-Magnet Radial Distance (r)	0.0
Coil Cross-Section Length	8.0
Coil Cross-Section Width	9.0
Actuator Arm Length (x_0)	42.0
Magnet Radius and Depth	5.0
Float Side Length	115.0
Float Depth	10.0
Bearing Tilt Length	190.0
Photodiode-Mirror Distance	70.0

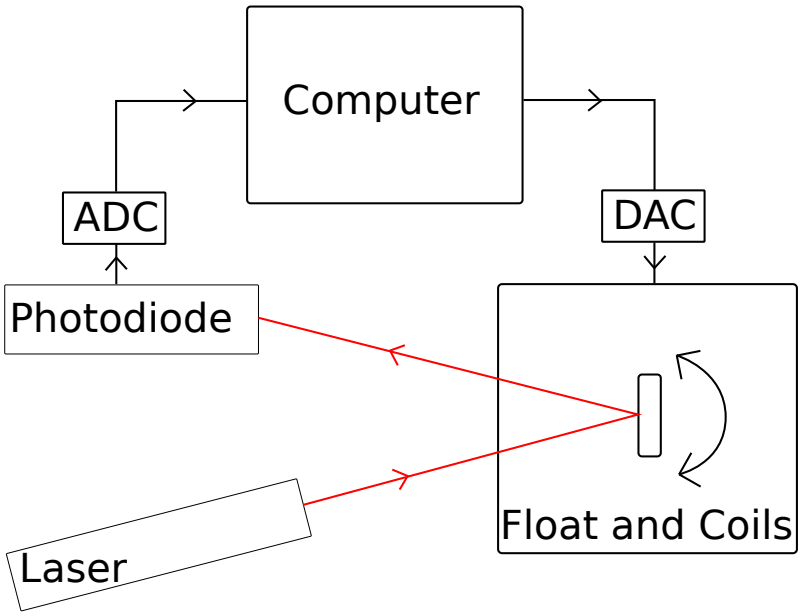

Figure 5.4: A general diagram of the full experimental setup.

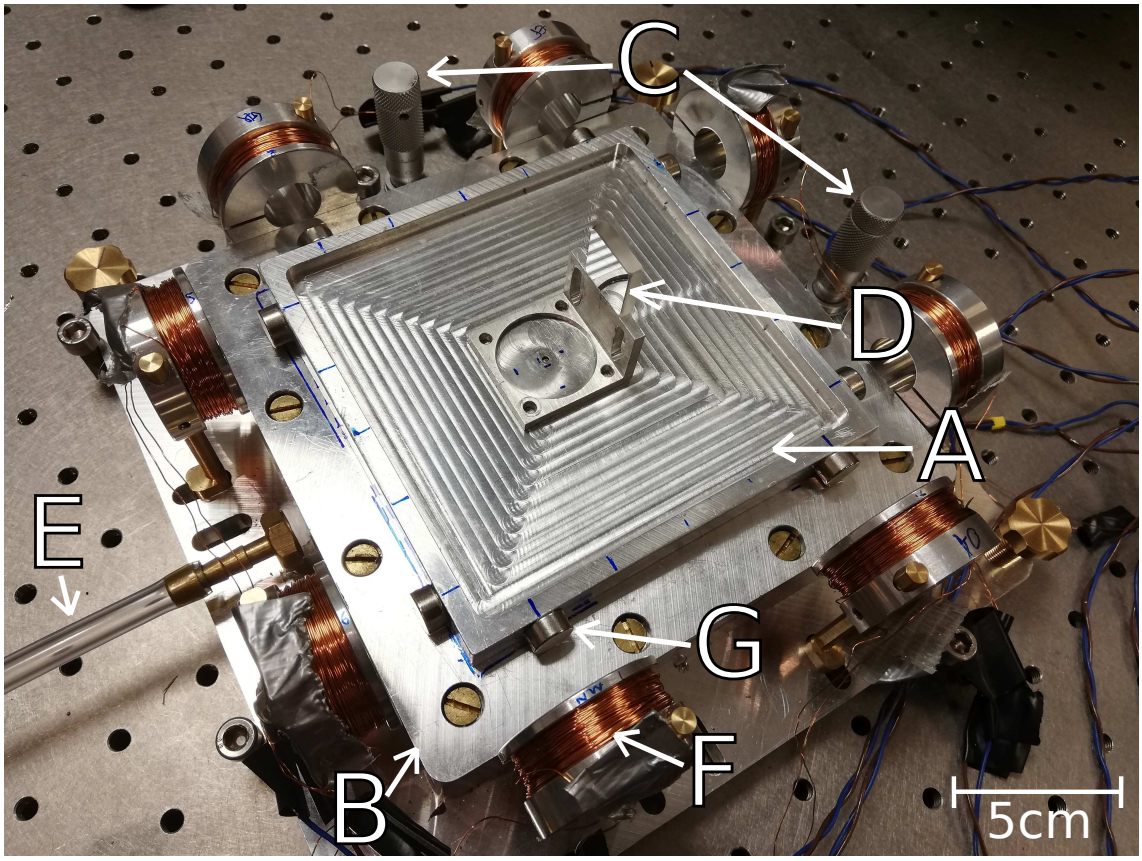

Figure 5.5: A photograph of the setup; showing: A - float, B - bearing, C - micrometers, D - mirror, E - compressed air input, F - a coil and G - a magnet.

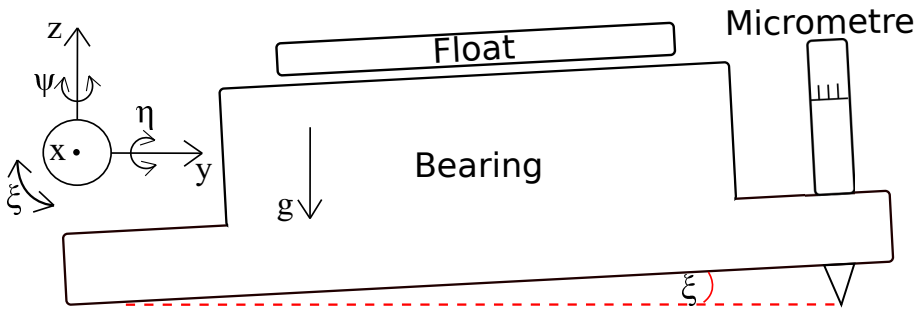

Figure 5.6: A side-on schematic drawing showing the float, bearing and the micrometre used to tilt the whole apparatus by an amount, ξ, around the x-axis from the horizontal where $\xi = 0$. The vertical is defined as the direction of the free-fall acceleration due to gravity, g. Positive and negative values of ξ correspond to raising or lowering the setup from the horizontal respectively. The global coordinate system defined in Figure 5.2 is shown again here. The coils have been omitted for clarity.

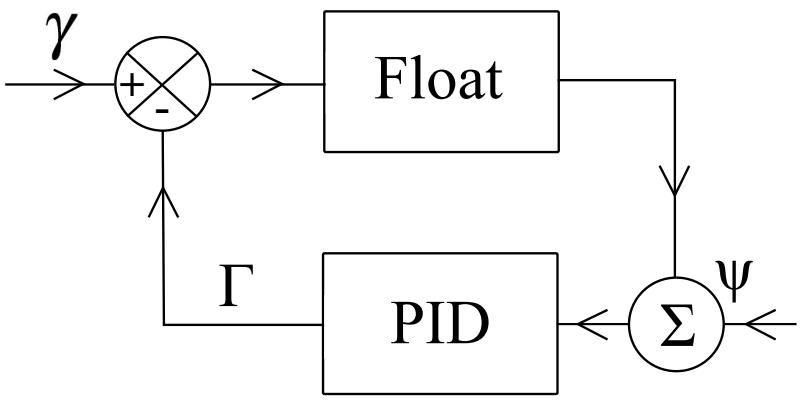

Figure 5.7: A block diagram showing the PID servo control. The PID introduces a torque, Γ, to the float after a known offset angle, ψ, is added to the controller input. There will also be additional noise torques, γ, acting on the float.

5.4 Results

The torque acting on the float could be measured from the PID servo output, whose control loop is shown in Figure 5.7. The PID servo applied a torque, Γ, to the float by adding or subtracting from the bias currents in the appropriate coils. All eight coils were used for this purpose, and the bias currents are those described in Equations 5.14, 5.15 and 5.16. The magnitude of this change in current from the bias currents could then be used in conjunction with Equation 5.3 multiplied by the actuator arm length term, x_0, from Table 5.1 to give

$$\Gamma = -8x_0 m \frac{\partial B_\zeta}{\partial \zeta}, \tag{5.17}$$

for eight coils. This measured torque is assumed to be equal to that described by Equation 5.15. The rotational stiffness could be measured by recording the change in torque, $\Delta\Gamma$, from Equation 5.17 applied by the PID servo to the float after an offset equivalent to a known angle, $\Delta\psi$, was added to the input of the controller. The rotational stiffness would then be given by

$$K_{\psi\psi} = -\frac{\Delta\Gamma}{\Delta\psi}, \tag{5.18}$$

where this rotational stiffness is assumed to be equal to that described by Equation 5.10 once it had been summed over all the coils. The linear transverse stiffness of the float in the x and y-axis of the horizontal plane as described in Figure 5.2 could be calculated using Equation 5.4

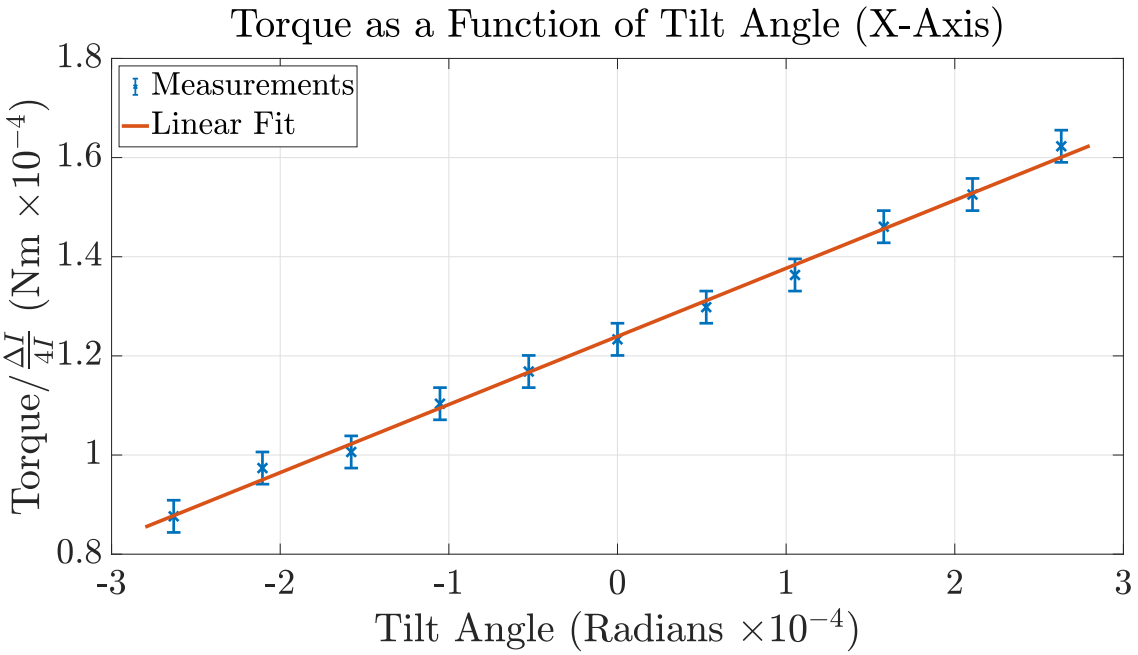

Figure 5.8: The torque, divided by the currents ratio term, acting on the float over a range of tilt angles from the horizontal in the x-axis.

summed over the bias currents of the four coils in each respective axis. As stated in Section 5.2, the positioning of the magnets was chosen to give $\theta = \pi$.

Before torque measurements could be made the float's centre-of-mass displacement from its NCB, x_{cm} from Equation 5.15, had to be made zero. This was done by placing small masses on the float in precise positions such that when tilting it from the horizontal the PID servo torque did not change within the limit of the servo readout noise. Doing this, while keeping the bias currents in all the coils equal such that ΔI was zero in Equation 5.15, implied that x_{cm} was equal to zero.

The PID servo torque on the float was then measured over a range of tilt angles from the horizontal, for a given set of bias currents. This was done in both the x and y-axis of the float as shown in Figure 5.2. The measurements in these axes are shown in Figures 5.8 and 5.9 respectively.

The total mass of the float, with the additional small masses used for minimising x_{cm}, was 338.66 g. This, along with the value of x_0 of (42.0 $\pm$ 0.5) mm from Table 5.1, implied the expected gradient of the plots from Equation 5.16 should be (0.139 $\pm$ 0.003) N·m/rad. The gradients from

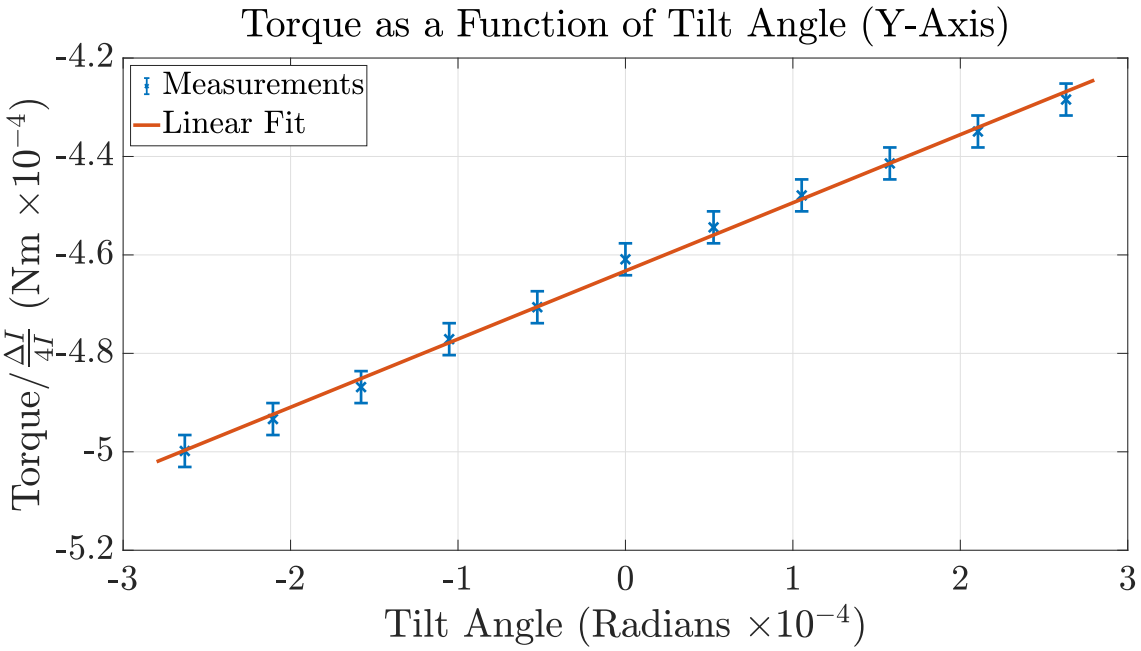

Figure 5.9: The torque, divided by the currents ratio term, acting on the float over a range of tilt angles from the horizontal in the y-axis.

Figures 5.8 and 5.9 are (0.137 ± 0.006) N·m/rad and (0.138 ± 0.006) N·m/rad respectively. With the bias currents used and Equation 5.14, the expected change of the centre-of-buoyancy of the float in both the x and y-axis was (7.00 ± 0.17) mm. Using the gradients from Figures 5.8 and 5.9, in conjunction with Equations 5.14 and 5.16, the measured changes in the centre-of-buoyancy in the x and y-axis were calculated to be (6.90 ± 0.32) mm and (6.95 ± 0.32) mm respectively. This shows that we had succeeded in tuning the float's centre-of-buoyancy to an accuracy of ± 0.3 mm.

With the bias currents in all coils set to 0.075 mA, and Equation 5.10 summed over all eight coils, the float's rotational stiffness was calculated to be (-14.73 ± 0.41) μN·m/rad. Using Equation 5.18 it was measured to be (-15.11 ± 2.05) μN·m/rad. With these bias currents, the float's transverse stiffness in each horizontal axis, using Equation 5.4 summed over the four coils in each axis, was calculated to be (1.11 ± 0.16) N/m. This gave a natural oscillation frequency in each axis of (0.29 ± 0.04) Hz. All the results are summarised in Table 5.2.

Table 5.2: A summary of the measurement results.

Attribute	Result
Plot Gradients	
Float x-Axis	(0.137 ± 0.006) N·m/rad
Float y-Axis	(0.138 ± 0.006) N·m/rad
Equation 5.16 Prediction	(0.139 ± 0.003) N·m/rad
Centre-of-Buoyancy Change	
Float x-Axis	(6.90 ± 0.32) mm
Float y-Axis	(6.95 ± 0.32) mm
Equation 5.14 Prediction	(7.00 ± 0.17) mm
Float Rotational Stiffness	
Measurement	(-15.11 ± 2.05) μN·m/rad
Equation 5.10 Prediction	(-14.73 ± 0.41) μN·m/rad
Float Transverse Stiffness and Frequencies	
Equation 5.4 x and y-Axis Calculation	(1.11 ± 0.16) N/m
Oscillation Frequency x and y-Axis	(0.29 ± 0.04) Hz

5.5 Discussion

The measurements in Figures 5.8 and 5.9 change linearly with tilt angle as expected from Equation 5.16. The gradients of these plots were expected to be 0.139 N·m/rad and the measured gradients all lie within 1.5% of this value and within their uncertainty ranges. The calculated and measured changes in the centre-of-buoyancy displacement of the float from Figures 5.8 and 5.9 were also within 1.5% of each other and within each others uncertainty ranges. Thus all the results are in excellent agreement with the theory. Crucially this demonstrates that it is possible to tune in-situ the centre-of-buoyancy of a suspended object and hence also possible to decouple its rotational motion from ground tilt and horizontal accelerations.

The measured and calculated rotational stiffnesses of the float were within 2.5% of each other and within their respective uncertainty bounds. The moduli of these values is an order of magnitude lower than the rotational stiffness of a torsion balance used in a recent determination of Newton's constant of gravitation, which had a stiffness of approximately 218 μN·m/rad [75]. Additional actuators could increase the float's transverse stiffness from the calculated values to make the float more transversely stable, and also allow the adjustment of its rotational stiffness. Preliminary measurements with this setup show that this is possible [27]. The natural oscillation frequencies of the float in the transverse plane were calculated. With the float being levitated through an air bearing, it can be assumed that its motion was highly damped. As such in this case there was no risk of the oscillations significantly affecting the float's motion.

The design could be improved to allow greater precision in the placement and adjustment of the different components to give more accurate results. The noise from the electronics of the positional photodiode was measured to be 8.4×10^{-7} N·m/$\sqrt{\text{Hz}}$, while the total noise of the air bearing system was measured to be 2.7×10^{-6} N·m/$\sqrt{\text{Hz}}$. This excess noise was most likely due to environmental air currents and fluctuations in the pressurised air supply to the air bearing. This was the largest contribution to the data point uncertainties in Figures 5.8 and 5.9. This gave an error on the gradients of these plots, which was then propagated onto the experimental estimation of x_{cb} from

Equation 5.14. No attempt was made to put the device in a protective enclosure or shield the photodiode from environmental light sources. As such the error on x_{cb} of $\pm$ 0.3 mm could be reduced by lowering the noise of the air bearing. This could be done by using a different method of levitation other than a pressurised-air suspension, such as an electrostatic or superconducting suspension [27]. From Equation 5.14, the theoretical maximum accuracy of centre-of-buoyancy tuning that could be attained with the setup presented here, taking into account the current noise from the coil drivers of the magnetic actuators averaged over a second, is $\pm$ 1.6×10^{-8} m. This corresponds to a possible improvement in accuracy of a factor of over 18000.

5.6 Conclusion

An air bearing suspension that levitates a float, with its motion in the horizontal plane of the laboratory controlled using magnetic actuators, was constructed. The observed behaviour of the float was compared to the predictions of a detailed model of the statics of the float-actuator system and they were found to be consistent. The results from Figures 5.8 and 5.9 demonstrate the in-situ electromagnetic tuning of the float's centre-of-buoyancy to an accuracy of $\pm$ 0.3 mm. This result implies it is practical to decouple the rotational mode of a suspended object from tilt and horizontal accelerations due to seismic noise, by tuning its centre-of-buoyancy to lie at its nominal centre-of-buoyancy (NCB).

This result paves the way for other, more sensitive, experiments to be designed with a view to performing weak-force measurements at sub-millimetre ranges. Work is ongoing on a superconducting torsion balance [27, 33]. The aim here is to develop an instrument which exhibits the same advantages as the air bearing where it can be tuned in-situ to be rotationally decoupled from ground tilt, in addition to allowing the in-situ tuning of its rotational stiffness. This combined with a transverse stiffness provided by the superconducting magnetic actuators should allow measurements of the inverse square law of gravity down to mass separations of the order of 10 μm. The Newtonian torque signal, given a days integration, requires a fundamental noise level of less than 1×10^{-14} N·m/$\sqrt{\text{Hz}}$. Given a typical seismic noise acceleration spectral density of 5×10^{-7}

$\mathrm{m/s^2}\sqrt{\mathrm{Hz}}$ and a suspended mass of 338.66 g, we would need to match the centre-of-buoyancy and mass to an accuracy of about 1×10^{-7} m. So an improvement in tuning accuracy of a factor of around a thousand would be required compared with what is achieved here. The uncertainty on the matching of the centres-of-mass and buoyancy is limited by the overall noise in the air bearing system, so this goal may be achievable with a superconducting or other type of suspension. We should also mention that a possible downside of this technique is the way that the actuation system can introduce noise into the measurement through its asymmetries (the κ parameter introduced in Equation 5.15). Any strategy of reducing this factor would include making such asymmetries as small as possible in the first instance, thus ensuring that the actuation torques themselves are as small as possible.

Chapter 6

Summary and Outlook

For a' that, an' a' that, it's coming yet for a' that, that Man to Man, the world o'er, shall brothers be for a' that.

Robert Burns

Torsion balances remain important tools in short-scale gravitational and weak-force physics. At the forefront of this area in modern physics, however, their drawbacks present serious barriers to progress. Despite their low rotational stiffness and having some degree of immunity to tilt, as well as to horizontal accelerations due to seismic noise, coupling into the rotational mode of the suspended mass, the vertical distance of its centre-of-mass from the point of attachment means horizontal accelerations can couple strongly to the simple pendulum mode. This makes control of the torsion bob difficult. Additionally, at some level there will always be some coupling to rotational motion. This means measurements of forces with mass separations of the order of 10 μm become excessively challenging with the conventional torsion balance design. Investigating experimental methods to circumvent these issues using novel techniques and redesigns of the traditional torsion balance is the central theme of this thesis.

Chapter 1 presented an introduction to some of the biggest problems facing modern physics: the hierarchy problem, the cosmological constant problem and issues related to formulating a theory

of quantum gravity. These provide the motivation for measuring the inverse square law of gravity at small mass separations, as deviations to Newtonian gravity at small scales due to the presence of large extra spatial dimensions could help provide solutions to these issues. The concept of large extra dimensions originates from String Theory [13, 14]. An overview of the experimental challenges that these measurements pose, as well as of the current landscape of instrumentation for these types of experiments, was then given. Their successes as well as their limitations are discussed therein.

Chapter 2 discussed the theory behind the motivations for redesigning the traditional torsion balance. This work was done in an attempt to overcome the challenges experienced in weak-force measurement experiments described in Chapter 1. The theory focussed on the use of external actuators acting on a levitated torsion bob, whose stiffnesses could be tuned in-situ, to allow in turn the in-situ tuning of both the rotational stiffness and centre-of-buoyancy of the torsion bob itself [27]. The former would allow the rotational stiffness of the torsion balance to be made nominally as close to zero as possible, while keeping the translational and tilt degrees-of-freedom at a greater stiffness. This would not be possible with a traditional torsion balance suspended by a long thin fibre. The latter could in principle allow the centre-of-buoyancy of the torsion bob to be tuned to lie at its centre-of-mass and hence decouple horizontal forces due to seismic noise and tilt from its rotational mode. A lower rotational stiffness would allow for weaker gravitational signal torques to be measured while the retention of a greater stiffness in the translational and tilt degrees-of-freedom would allow for a smaller test and source mass separation. The decoupling of the rotational mode from seismic noise would further improve the instrument's sensitivity. In addition to these, the actuators would provide a transverse stiffness to the torsion bob which would dampen the simple pendulum mode. These features in a torsion balance would allow for far more reliable measurements of weak forces at sub-millimetre mass separations than what has been achieved previously.

In Chapter 3 the Superconducting Torsion Balance experiment was described in detail. Its main components were highlighted including the source and test masses and their manufacturing proce-

dure, and the float and bearing for levitating and controlling the test mass, as well as the details of the superconducting lead coil actuators in the bearing. The expected gravitational torque signal and sources of noise were also discussed. My contribution to the experiment was highlighted. This included redesigning the float to allow it to be more accurately positioned above the bearing using three Attocube micro-positioners acting as a kinematic mount, rewiring the heatswitches on the experiment which were needed to store persistent currents in the superconducting lead coils, designing a baseplate for the experiment in order to host various pieces of diagnostic hardware and calibrating Allen Bradley resistors as temperature sensors to aid in the cryogenic level detection. The magnetic forces from the levitation coil in the bearing for levitating the float and test mass were modelled using finite element analysis software (FEMM) and the results of this were presented. These indicate that the float should be able to be levitated by the lift forces produced by the levitation coil. Finally, the current status of the experiment is stated along with the necessary work yet to be done.

In Chapter 4 the work on the Superconducting Torsion Balance's capacitive sensor that was described in the paper [28] was reproduced in full. This work was done to circumvent the issue of stray-capacitance which is inherent in the long and thin wires typical of cryogenic experiments. The stray-capacitance between the core and shield of signal-carrying cables can introduce, in addition to various instabilities such as oscillations, a large noise-gain into pre-amplifier circuits. The method presented here to overcome this issue was to float the shield with respect to ground; in this case with a 1.8 pF capacitor. This effectively removed the increase in noise gain from the pre-amplifier circuit. The caveat with is method is that it reduced the effectiveness of the shield. The voltage noise of this proposed circuit was modelled, measured and compared to various other circuits, both in test formats as well as in-situ in the experiment. It was shown that this method, when used in the detection circuitry of the experiment, could give a signal-to-noise ratio greater than 1 for an expected signal of 2×10^{-17} N·m on the test mass if modulated at a frequency of 100 kHz.

In Chapter 5 the work on the Air Bearing experiment that was described in the paper [29] was also

reproduced in full. This experiment was designed to demonstrate the centre-of-buoyancy tuning described in Chapter 2. In this experiment a float was levitated using compressed air, and was controlled in the horizontal plane of the laboratory by coil-magnet actuators. Its statics were modelled and compared to measurements which were consistent to within 1.5% of each other, where the in-situ centre-of-buoyancy tuning was demonstrated to a precision of $\pm$ 0.3 mm. Its rotational stiffness was also measured and compared to that of a torsion balance used in a recent determination of Newton's constant of gravitation [75], and its modulus was found to be lower by an order of magnitude.

The Superconducting Torsion Balance is still incomplete. The float in the experiment has yet to be reliably levitated. One possible reason for this is expected to be trapped flux in the lead foil of the float [49]. The easiest way to remove this would be to shield the experimental cavity with, for example, μ-metal, or by degaussing the superconducting elements in the experiment through a localised heating method. Once the float can be levitated consistently and reliably, measuring the noise of the system and characterising the in-situ rotational stiffness and centre-of-buoyancy tuning of the float as outlined in Chapter 2 would be the next step. Improving the flatness of the source and test mass foils to $\pm$ 1.5 μm across their surfaces is also required before measurements of the inverse square law of gravity can take place at mass separations of 15 μm. This could be done through more analysis of the warping of the mass rings after they are stressed by tightening and then releasing them with the screws on the torsion jig, by looking at alternative methods of gluing the foils to the mass rings and by increasing the tension the foils are subjected to [43, 44]. If these requirements are met, the source and test masses could be put in place on the experiment to allow gravitational inverse square law measurements to be made.

The results from the Air Bearing experiment in Chapter 5 raise the proposition of a room temperature analogue to the Superconducting Torsion Balance. This would have the advantage of not having to operate in cryogenic conditions and as such could be mechanically much simpler and easier to operate from a technical point of view. As stated in Chapter 5, the centre-of-buoyancy tuning would need to be improved by a factor of around a thousand for this to be viable. The

Air Bearing was limited by the noise of the compressed air suspension and so using a different set-up could make this possible, specifically a different method of levitation other than from a compressed air supply such as an electrostatic or magnetic suspension. A way to tune in-situ the rotational stiffness would also need to be included as this was absent in that experiment. One way forward with this idea is to suspend the float and test mass with three fibres, as opposed to one as in the typical torsion balance. This would increase the stiffness in the simple pendulum mode, while the corresponding increase in rotational stiffness could be offset through the in-situ rotational stiffness tuning from external actuators. The actuators could then also perform the in-situ centre-of-buoyancy tuning to further improve the sensitivity. In this scenario electrostatic actuators would be an ideal choice, assuming the noise associated with the large voltage power supplies needed for the actuators is sufficiently small.

Appendix A

Cryogenic Cooling Method

This is the procedure for cooling the Superconducting Torsion Balance in Chapter 3 from room temperature down to 4.2 K using liquid nitrogen and then liquid helium.

1. Run all necessary electronic/hardware checks to ensure the equipment is working properly at room temperature and then leak test the experimental cavity, which contains the superconducting suspension experiment, with helium gas once it is sealed with indium wire.

2. Introduce helium exchange gas into the experimental cavity. The air in the attached lines is pumped out first using a turbo-pump and then the helium gas cannister is used to carefully introduce small volumes of helium gas into the experimental cavity. Aim for approximately 40 mbar at room temperature, which gives around 10 mbar at 77.3 K and 1 mbar at 4.2 K. This set-up is shown in Figure A.1.

3. Once these initial steps are complete pre-cool the cryogenic dewar with liquid nitrogen. This is then left for at least two days to ensure the super-insulation material in the dewar is sufficiently cooled. This will require approximately 120 L of liquid nitrogen. Once left for around two days, rerun the electronic/hardware checks to ensure the equipment is working properly at 77.3 K.

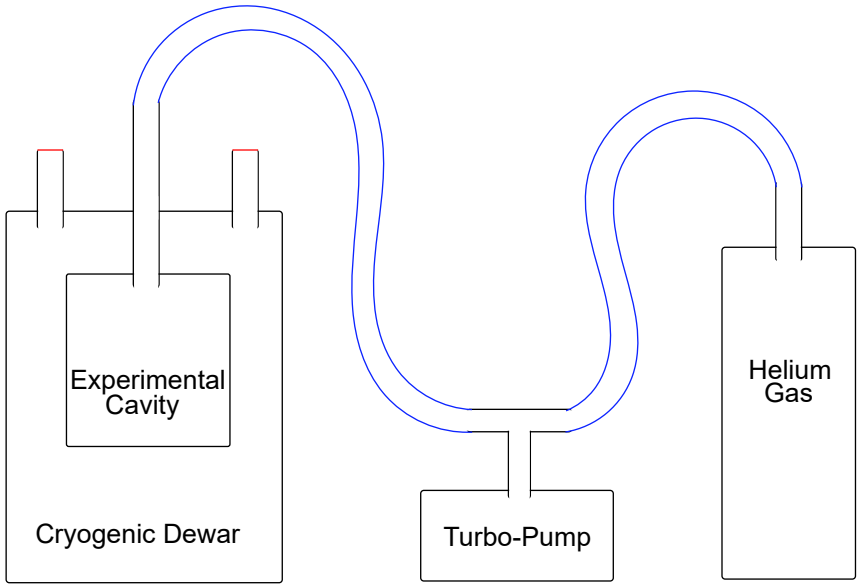

Figure A.1: The required set-up to introduce helium exchange gas into the experimental cavity.

4. Nitrogen gas is then used to force the remaining liquid nitrogen from the pre-cooling out of the cryogenic dewar prior to the introduction of liquid helium. Excess liquid nitrogen from the cryogenic dewar is returned to a liquid nitrogen dewar. This set-up is shown in Figure A.2.

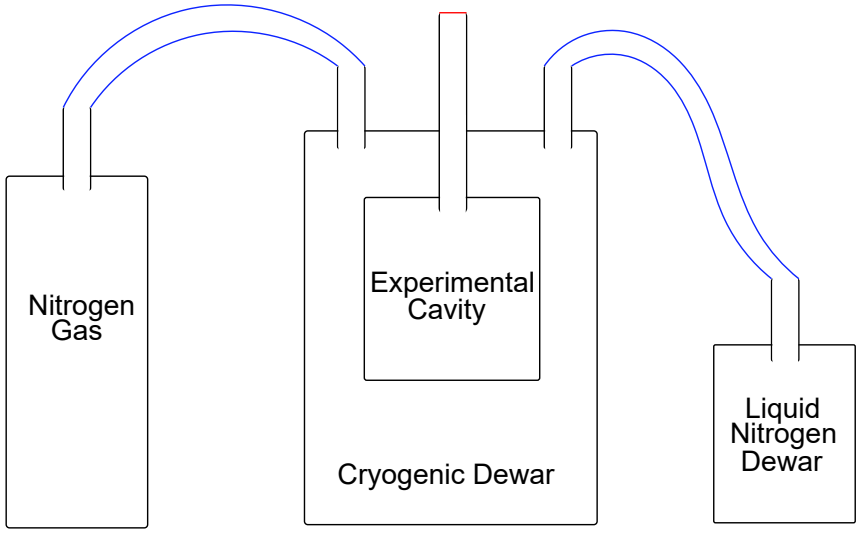

Figure A.2: The required set-up to remove any remaining liquid nitrogen from the cryogenic dewar using nitrogen gas.

5. The cryogenic dewar should then be evacuated using a backing pump to remove any remaining nitrogen gas, along with running a heater consisting of power resistors in the bottom of the dewar to ensure all liquid nitrogen has been evaporated off. The Allen Bradley resistor temperatures at the bottom of the dewar should drop briefly drop below 77.3 K due to this evacuation, and will start to rise above 77.3 K when all the remaining liquid nitrogen is removed. The Allen Bradleys, silicon diodes, and liquid nitrogen level detector can all be used to monitor the removal of liquid nitrogen. A pressure gauge can also be used to help guide the process, a reading of around -70 PSI indicates that nitrogen gas has been evacuated to a sufficient level. This set-up (which also contains components for the next step but with the line to the helium gas and helium return line closed) is shown in Figure A.3.

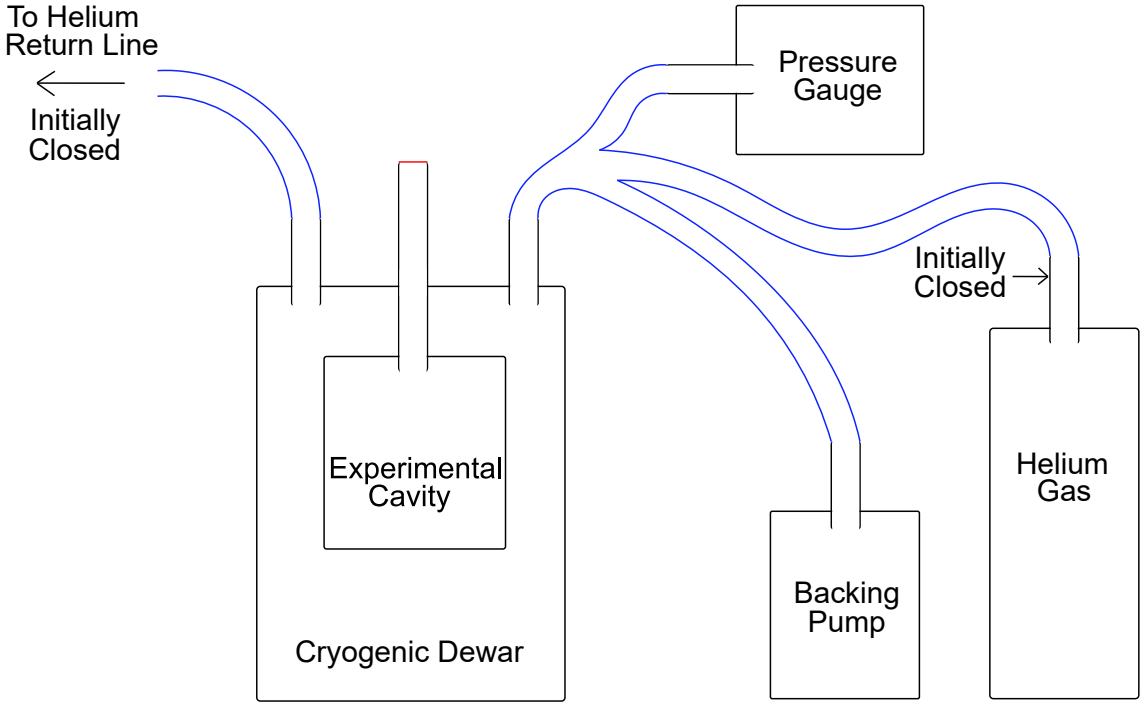

Figure A.3: The set-up required to remove any remaining nitrogen gas from the cryogenic dewar, and then introduce a helium gas atmosphere.

6. A helium gas atmosphere is needed in the cryogenic dewar before any liquid helium is introduced. Helium gas should be introduced from the helium gas cannister until there is a slightly positive pressure compared to the lab; to just above 1 atm. Then it is pumped out

and refilled with helium gas; this is repeated at least twice as an extra step to ensure the complete removal of any remaining nitrogen gas. The pressure gauge can be refereed to as before for when to start and stop pumping. This set-up is shown in Figure A.3, but now with the line to the helium open.

7. Anything containing cooled helium (gas or liquid) should be connected to the helium return line which is now opened for this step (with the exception of the liquid helium dewar). All connected pipes are filled with a cold helium gas atmosphere from the liquid helium dewar. Cold helium gas is then flushed into the cryogenic dewar. This is done by keeping the end of the connector between the cryogenic dewar and liquid helium dewar, called the transfer line, that goes into the cryogenic dewar free. Then the end that goes into the liquid helium dewar is slowly lowered; this is to check that cold helium gas is coming through first. Once this occurs the free end is lowered into the cryogenic dewar and the liquid helium itself can be flushed into the cryogenic dewar using the helium gas. The tap to the helium return line from the liquid helium dewar should be closed for this step, so that pressure doesn't escape that way. The Allen Bradleys, silicon diodes, and liquid helium level detector can all be used to check the rate of the liquid helium transfer. This set-up is shown in Figure A.4. The experimental cavity should be submerged in liquid helium to a depth of at least 10 cm to ensure there will be enough to allow the experiment to remain at 4.2 K for a sufficient duration. Once it is submerged, the experiment should be left for approximately one hour to ensure the contents of the experimental cavity have cooled to 4.2 K. The enthalpy of the helium exchange gas in the experimental cavity should allow it to efficiently cool its contents in this time-frame.

8. Once the experiment is over and has been left to heat up to room temperature for around 2-3 days, the experimental cavity should be filled with nitrogen gas to make future leak detection with helium gas easier. This set-up is shown in Figure A.5.

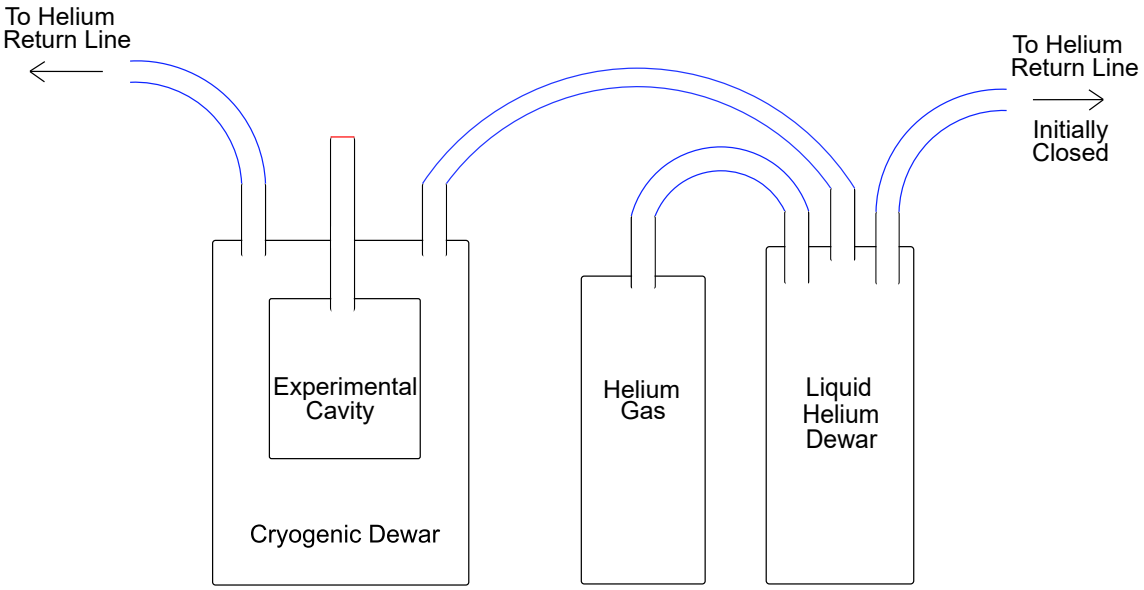

Figure A.4: The set-up required to transfer liquid helium to the cryogenic dewar using helium gas.

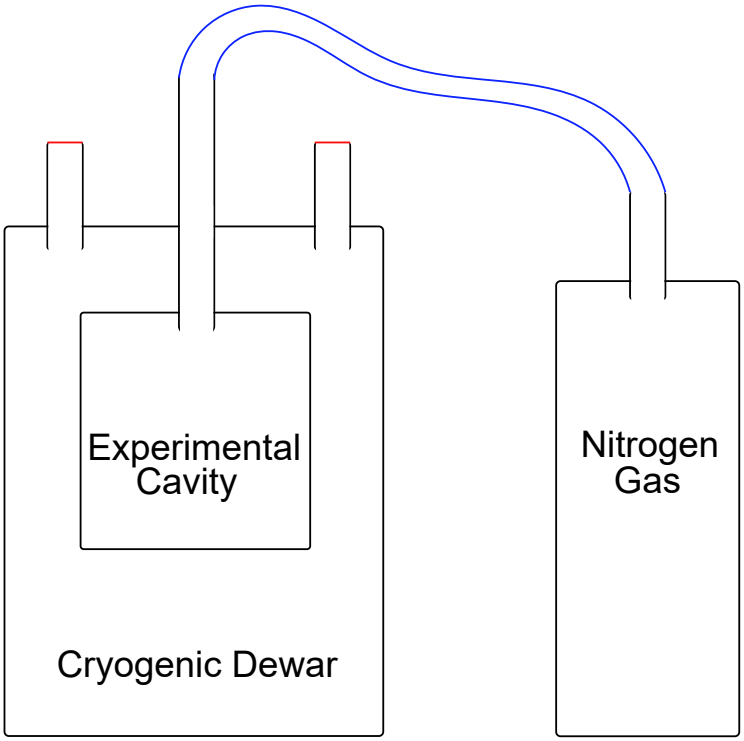

Figure A.5: The set-up required to fill the experimental cavity with nitrogen gas in preparation for future leak detection with helium gas.

Appendix B

Noise Gain Equations Derivations

B.1 Benchmark Circuit Noise Gain

This is a derivation for Equation 4.3 from Chapter 4. Equation 4.2 states that noise gain can be defined as

$$G = 1 + \frac{Z_2}{Z_1}. \tag{B.1}$$

From Figure 4.4 it is clear that impedance Z_2 is given by resistor R_1 and capacitor C_2 in parallel,

$$Z_2 = \left(\frac{1}{R_1} + i\omega C_2\right)^{-1}. \tag{B.2}$$

Z_1 is then simply the impedance from capacitor C_1,

$$Z_1 = \frac{1}{i\omega C_1}. \tag{B.3}$$

The noise gain for the benchmark circuit is then

$$G = \left(\frac{R_1}{1 + i\omega C_2 R_1}\right) \cdot (i\omega C_1) + 1 = \frac{i\omega C_1 R_1}{1 + i\omega C_2 R_1} + 1. \tag{B.4}$$

B.2 Stray-Capacitance Circuit Noise Gain

This is a derivation for Equation 4.6 from Chapter 4. Equation 4.2 remains the same as in Equation B.1. From Figure 4.7 it is clear that impedance Z_2 is the same as in Equation B.2, with

the component labels changed where necessary. Z_1 is then the impedance from capacitors C_1 and C_2 in parallel,

$$Z_1 = (i\omega C_1 + i\omega C_2)^{-1}. \tag{B.5}$$

The noise gain for the stray-capacitance circuit is then

$$G = \left(\frac{R_1}{1 + i\omega C_3 R_1}\right) \cdot (i\omega C_1 + i\omega C_2) + 1 = \frac{i\omega R_1 (C_1 + C_2)}{1 + i\omega C_3 R_1} + 1. \tag{B.6}$$

B.3 Proposed Circuit Noise Gain

This is a derivation for Equation 4.8 from Chapter 4. Equation 4.2 remains the same as in Equation B.1. From Figure 4.12 it is clear that impedance Z_2 is the same as in Equation B.2, with the component labels changed where necessary. Z_1 is then the impedance from capacitor C_1 in parallel with the impedances of capacitors C_2 and C_3 in series,

$$Z_1 = \left(i\omega C_1 + \left(\frac{1}{i\omega C_2} + \frac{1}{i\omega C_3}\right)^{-1}\right)^{-1} = \left(i\omega C_1 + \frac{i\omega C_2 C_3}{C_2 + C_3}\right)^{-1}. \tag{B.7}$$

The noise gain for the proposed circuit is then

$$G = \left(\frac{R_1}{1 + i\omega C_4 R_1}\right) \cdot \left(\frac{i\omega (C_1 (C_2 + C_3) + C_2 C_3)}{C_2 + C_3}\right) + 1 = \frac{i\omega R_1 (C_1 (C_2 + C_3) + C_2 C_3)}{(1 + i\omega C_4 R_1)(C_2 + C_3)} + 1. \tag{B.8}$$

Appendix C

Voltage Noise to Displacement Noise Conversion

To convert the measured voltages noises, V_n, of the circuits summarised in Table 4.1 in Chapter 4 to displacement noises, they must first be converted to current noises, I_n. Since the pre-amplifier of the capacitive sensor in each case is in a transimpedance configuration with a nominal voltage gain of unity, this can be done by dividing the output voltage noises by the impedance of the transmittance resistor, R, which was 620 $k\Omega$ in each case. And so,

$$I_n = \frac{V_n}{R}. \tag{C.1}$$

This could then be converted into a capacitance noise by dividing the current noise by the bias AC drive voltage, V_D, on each capacitive electrode of 4.0 V, as well as by the frequency of the modulation $\omega = 2\pi f$ at 100 kHz. Giving,

$$C_n = \frac{I_n}{V_D 2\pi f}. \tag{C.2}$$

Finally, this had to be converted to a displacement noise, D_n. As described in Section 3.1.1 of Chapter 3, a differential capacitive sensor was used as the displacement sensor for the float and test

mass. The two capacitive electrodes in the transducer bridge had a mean separation to the float's surface, d, of the order of 1 mm and a capacitive plate area, A, of 3.75×10^{-4} m^2. Due to the rotational motion of the float and test mass, the change in capacitance with the electrode-to-float gap would not be linear. However, an expected torque signal of the order of $2{\times}10^{-17}$ N·m would produce such a small displacement around this mean separation that this change can be assumed to be linear on that scale. The change in displacement corresponding to a change in capacitance equal to the capacitance noise, and hence the associated displacement noise itself, for a single capacitor electrode can be related by the following,

$$C_n = \frac{\epsilon_0 A}{d - D_n} - \frac{\epsilon_0 A}{d} = \frac{\epsilon_0 A D_n}{d(d - D_n)}. \tag{C.3}$$

The nominal capacitance between each electrode and the float due to their mean separation is simply,

$$C_0 = \frac{\epsilon_0 A}{d} = 3.32\,(p\mathrm{F})\,, \tag{C.4}$$

and since $d >> D_n$, Equation C.3 simplifies to,

$$C_n = \frac{D_n}{d} C_0. \tag{C.5}$$

Since this is a bridge, the overall capacitance change will be multiplied by a factor of 2. With this knowledge, rearranging for D_n, we find,

$$D_n = \frac{dC_n}{2C_0}. \tag{C.6}$$

Appendix D

Magnetic Actuator Derivations

D.1 Magnet/Coil Actuator Rotational Stiffness

This is a derivation for Equation 5.10 from Chapter 5. Equation 5.8 states the potential energy of a magnet/coil pair in Figure 5.1 can be written as

$$U = -mB\left(f(\psi) + y\right)\cos\left(\theta + \psi\right), \tag{D.1}$$

where in Equation 5.7 $f\left(\psi\right)$ is defined as

$$f\left(\psi\right) = b - a\cos\psi + x_0\sin\psi, \tag{D.2}$$

in the context of the set-up of each magnet/coil pair described in Figure 5.2. It is convenient to express the magnetic field produced by a coil as a Taylor series around the magnet's equilibrium position where we define the equilibrium spacing between each magnet and coil as g_0. From Equation 5.9 the magnetic field can then be written,

$$B = B_0 + \left(\frac{\mathrm{d}B}{\mathrm{d}\zeta}\right)_{g_0} \cdot \left(f\left(\psi\right) + y - g_0\right) + \frac{1}{2}\left(\frac{\mathrm{d}^2B}{\mathrm{d}\zeta^2}\right)_{g_0} \cdot \left(f\left(\psi\right) + y - g_0\right)^2. \tag{D.3}$$

Setting $y = 0$ and $\theta = \pi$, and substituting Equations D.2 and D.3 into Equation D.1, the following

is obtained,

$$\begin{aligned} U &= m\Bigg[B_0\cos\psi + \left(\frac{\mathrm{d}B}{\mathrm{d}\zeta}\right)_{g_0}\cdot\left(b\cos\psi - a\cos^2\psi + x_0\sin\psi\cos\psi - g_0\cos\psi\right) \\ &+ \frac{1}{2}\left(\frac{\mathrm{d}^2B}{\mathrm{d}\zeta^2}\right)_{g_0}\cdot\left(b^2\cos\psi + a^2\cos^3\psi + x_0^2\sin^2\psi\cos\psi + g_0^2\cos\psi\right. \\ &- 2ab\cos^2\psi + 2x_0b\sin\psi\cos\psi - 2bg_0\cos\psi + 2ag_0\cos^2\psi \\ &- \left.2x_0g_0\sin\psi\cos\psi - 2ax_0\sin\psi\cos^2\psi\right)\Bigg]. \end{aligned} \tag{D.4}$$

The rotational stiffness for a single magnet/coil pair is given by the second derivative of Equation D.4 with respect to ψ,

$$\begin{aligned} K^i_{\psi\psi} &= \frac{\mathrm{d}^2U}{\mathrm{d}\psi^2} = m\Bigg[-B_0\cos\psi + \left(\frac{\mathrm{d}B}{\mathrm{d}\zeta}\right)_{g_0}\cdot\left(2a\cos^2\psi - 2a\sin^2\psi - b\cos\psi - 4x_0\sin\psi\cos\psi\right. \\ &+ \left.g_0\cos\psi\right) + \frac{1}{2}\left(\frac{\mathrm{d}^2B}{\mathrm{d}\zeta^2}\right)_{g_0}\cdot\left(4ab\cos^2\psi - 4ab\sin^2\psi - b^2\cos\psi - 3a^2\cos^3\psi\right. \\ &+ 6a^2\sin^2\psi\cos\psi - 7x_0^2\sin^2\psi\cos\psi + 2x_0^2\cos^3\psi - g_0^2\cos\psi - 8bx_0\sin\psi\cos\psi \\ &+ 2bg_0\cos\psi - 4ag_0\cos^2\psi + 4ag_0\sin^2\psi + 8x_0g_0\sin\psi\cos\psi + 14ax_0\sin\psi\cos^2\psi \\ &- \left.4ax_0\sin^3\psi\right)\Bigg]. \end{aligned} \tag{D.5}$$

In the case presented in Chapter 5, ψ is a small angle whose mean is zero and so it can be assumed $\psi \approx 0$. This implies

$$\begin{aligned} K^i_{\psi\psi} &= m\Bigg[\frac{1}{2}\left(\frac{\mathrm{d}^2B}{\mathrm{d}\zeta^2}\right)_{g_0}\cdot\left(4ab - b^2 - 3a^2 + 2x_0^2 - g_0^2 + 2bg_0 - 4ag_0\right) \\ &+ \left(\frac{\mathrm{d}B}{\mathrm{d}\zeta}\right)_{g_0}\cdot\left(2a - b + g_0\right) - B_0\Bigg]. \end{aligned} \tag{D.6}$$

Finally, from the geometries present in Figure 5.3, $g_0 = b - a$, and so Equation D.6 can be simplified to the following,

$$K^i_{\psi\psi} = m\left(\frac{\mathrm{d}^2B}{\mathrm{d}\zeta^2}x_0^2 + \frac{\mathrm{d}B}{\mathrm{d}\zeta}a - B_0\right). \tag{D.7}$$

D.2 Magnet/Coil Actuator Centre-of-Buoyancy Tuning

This is a derivation for Equation 5.14 from Chapter 5. Equations 5.8, 5.7 and 5.9 remain the same as in Equations D.1, D.2 and D.3 respectively. Setting $\theta = \pi$, the potential energy of a magnet/coil

pair in this case is then

$$\begin{aligned} U &= m\Bigg[B_0\cos\psi + \left(\frac{\mathrm{d}B}{\mathrm{d}y}\right)_{g_0}\cdot\left(b\cos\psi - a\cos^2\psi + x_0\sin\psi\cos\psi + y\cos\phi - g_0\cos\psi\right) \\ &+ \frac{1}{2}\left(\frac{\mathrm{d}^2B}{\mathrm{d}y^2}\right)_{g_0}\cdot\left(2by\cos\psi - 2bg_0\cos\psi + a^2\cos^3\psi + x_0^2\sin^2\psi\cos\psi - 2yg_0\cos\psi\right. \\ &- 2ab\cos^2\psi + 2bx_0\sin\psi\cos\psi - 2ay\cos^2\psi + 2ag_0\cos^2\psi + 2yx_0\sin\psi\cos\psi \\ &- \left.2x_0g_0\sin\psi\cos\psi + y^2\cos\psi + b^2\cos\psi + g_0^2\cos\psi - 2ax_0\sin\psi\cos^2\psi\right)\Bigg]. \end{aligned} \tag{D.8}$$

The cross-term from the stiffness matrix describing the static behaviour of the float, $k_{y\psi}$, is defined as

$$\begin{aligned} k_{y\psi} &= \frac{\mathrm{d}^2U}{\mathrm{d}y\mathrm{d}\psi} = m\Bigg[-\left(\frac{\mathrm{d}B}{\mathrm{d}y}\right)_{g_0}\cdot\left(\sin\psi\right) + \frac{1}{2}\left(\frac{\mathrm{d}^2B}{\mathrm{d}y^2}\right)_{g_0}\cdot\left(2x_0\cos^2\psi + 4a\sin\psi\cos\psi\right. \\ &- \left.2x_0\sin^2\psi - 2b\sin\psi + 2g_0\sin\psi - 2y\sin\psi\right)\Bigg]. \end{aligned} \tag{D.9}$$

In the case presented in Chapter 5, ψ is a small angle whose mean is zero and so it can be assumed $\psi \approx 0$. This implies

$$k_{y\psi} = x_0 m\frac{\mathrm{d}^2B}{\mathrm{d}y^2}. \tag{D.10}$$

With $\theta = \pi$, Equation 5.4 becomes

$$k_{yy} = m\frac{\mathrm{d}^2B}{\mathrm{d}y^2}. \tag{D.11}$$

Considering the x direction of the float in Figure 5.2, the position of the centre-of-buoyancy with respect to the NCB of the float, x_{cb}, in that axis could be modified by changing the stiffnesses of some actuators relative to others as described by the relation from Equation 5.11,

$$x_{cb} = \frac{K_{y\psi}}{K_{yy}}. \tag{D.12}$$

The upper case notation for the stiffness terms refers to the sum of the terms over the magnet/coil pairs in the relevant axis rather than an individual pair. In the case of the x direction of the float in Figure 5.2, Equation D.12 becomes

$$x_{cb} = \frac{K^a_{y\psi} + K^b_{y\psi} + K^e_{y\psi} + K^f_{y\psi}}{K^a_{yy} + K^b_{yy} + K^e_{yy} + K^f_{yy}} = x_0\left(\frac{\frac{\mathrm{d}^2B^b}{\mathrm{d}y^2} + \frac{\mathrm{d}^2B^e}{\mathrm{d}y^2} - \frac{\mathrm{d}^2B^a}{\mathrm{d}y^2} - \frac{\mathrm{d}^2B^f}{\mathrm{d}y^2}}{\frac{\mathrm{d}^2B^b}{\mathrm{d}y^2} + \frac{\mathrm{d}^2B^e}{\mathrm{d}y^2} + \frac{\mathrm{d}^2B^a}{\mathrm{d}y^2} + \frac{\mathrm{d}^2B^f}{\mathrm{d}y^2}}\right). \tag{D.13}$$

Equation 5.1 indicates the magnetic field produced by the coils, and its derivatives, are all proportional to the current in the respective coils. Hence Equation D.13 becomes

$$x_{cb} \approx x_0 \frac{\left(I^b + I^e - I^a - I^f\right)}{I^b + I^e + I^a + I^f} = x_0 \frac{\left(I^b + I^e - I^a - I^f\right)}{4I}, \tag{D.14}$$

where I is the average bias current in the coils labelled a, b, e and f in Figure 5.2.

Bibliography

[1] H. Cavendish. XXI. Experiments to Determine the Density of the Earth. *Philosophical Transaction of the Royal Society of London*, 88(5-6):469–526, 1798.

[2] C. A. de Coulomb. Premier Mémoire sur l'Electricité et le Magnétisme, Mém. *Acad. Roy. Sci.*, 1:569–577, 1785.

[3] E. G. Adelberger, B. R. Heckel, and A. E. Nelson. Tests of the Gravitational Inverse-Square Law. *Annual Review of Nuclear and Particle Science*, 53(1):77–121, 2003.

[4] R. D. Newman, E. C. Berg, and P. E. Boynton. Tests of the Gravitational Inverse Square Law at Short Ranges. *Space Science Reviews*, 148(1-4):175–190, Dec 2009.

[5] J. Murata and S. Tanaka. A Review of Short-Range Gravity Experiments in the LHC Era. *Classical and Quantum Gravity*, 32(3), Feb 5 2015.

[6] W. Yao, C. D. Amsler, D. M. Asner, et al. Review of Particle Physics. *Journal of Physics G: Nuclear and Particle Physics*, 33(1):001, 2006.

[7] A. G. Riess, A. V. Filippenko, P. Challis, et al. Observational Evidence from Supernovae for an Accelerating Universe and a Cosmological Constant. *The Astronomical Journal*, 116(3):1009, 1998.

[8] S. Perlmutter, G. Aldering, G. Goldhaber, et al. Measurements of Ω and Λ From 42 High-Redshift Supernovae. *The Astrophysical Journal*, 517(2):565, 1999.

[9] S. M. Carroll, W. H. Press, and E. L. Turner. The cosmological constant. *Annual Review of Astronomy and Astrophysics*, 30(1):499–542, 1992.

[10] E. Rocco. *Development of a Test of Newton's Law of Gravitation at Micrometer Distances using a Superconducting Spherical Torsion Balance.* PhD Thesis, University of Birmingham, May 2008.

[11] I. J. R. Aitchison and Anthony J. G. H. *Gauge Theories in Particle Physics: From Relativistic Quantum Mechanics to QED.* Graduate Student Series in Physics. Institute of Physics, Bristol, third edition, 2003.

[12] Y. Fujii. Dilaton and Possible Non-Newtonian Gravity. *Nature Physical Science*, 234(44):5–7, 1971.

[13] N. Arkani-Hamed, S. Dimopoulos, and G. Dvali. The Hierarchy Problem and New Dimensions at a Millimeter. *Physics Letters B*, 429(3-4):263–272, Jun 18 1998.

[14] I. Antoniadis, N. Arkani-Hamed, S. Dimopoulos, and G. Dvali. New Dimensions at a Millimeter to a Fermi and Superstrings at a TeV. *Physics Letters B*, 436(3-4):257–263, 1998.

[15] C. D. Hoyle, D. J. Kapner, B. R. Heckel, et al. Submillimeter Tests of the Gravitational Inverse-Square Law. *Physical Review D*, 70(4):042004, 2004.

[16] C. P. Burgess. Towards a Natural Theory of Dark Energy: Supersymmetric Large Extra Dimensions. In *AIP Conference Proceedings*, volume 743, pages 417–449. American Institute of Physics, 2004.

[17] M. Pojer, R. Giachino, D. Nisbet, et al. LHC Operational Experience of the 6.5 TeV Proton Run with ATS Optics. In *Proceedings, 9th International Particle Accelerator Conference (IPAC 2018)*, pages 216–219, 2018.

[18] E. G. Floratos and G. K. Leontaris. Low Scale Unification, Newton's Law and Extra Dimensions. *Physics Letters B*, 465(1-4):95–100, 1999.

[19] A. Kehagias and K. Sfetsos. Deviations From the 1/r2 Newton Law due to Extra Dimensions. *Physics Letters B*, 472(1-2):39–44, 2000.

[20] D. B. Kaplan and M. B. Wise. Couplings of a Light Dilaton and Violations of the Equivalence Principle. *Journal of High Energy Physics*, 2000(08):037, 2000.

[21] Y-J. Chen, W. K. Tham, D. E. Krause, et al. Stronger Limits on Hypothetical Yukawa Interactions in the 30–8000 nm Range. *Physical review letters*, 116(22):221102, 2016.

[22] J. K. Hoskins, R. D. Newman, R. Spero, and J. Schultz. Experimental Tests of the Gravitational Inverse-Square Law for Mass Separations From 2 to 105 cm. *Physical Review D*, 32(12):3084, 1985.

[23] S-Q. Yang, B-F. Zhan, Q-L. Wang, et al. Test of the Gravitational Inverse Square Law at Millimeter Ranges. *Physical Review Letters*, 108(8):081101, 2012.

[24] W-H. Tan, A-B. Du, W-C. Dong, et al. Improvement for Testing the Gravitational Inverse-Square Law at the Submillimeter Range. *Physical Review Letters*, 124(5):051301, 2020.

[25] J. G. Lee, E. G. Adelberger, T. S. Cook, S. M. Fleischer, and B. R. Heckel. New Test of the Gravitational $1/r^2$ Law at Separations down to 52 μm. *Physical Review Letters*, 124(10):101101, 2020.

[26] D. J. Kapner, T. S. Cook, E. G. Adelberger, et al. Tests of the Gravitational Inverse-Square Law below the Dark-Energy Length Scale. *Physical Review Letters*, 98(2):021101, 2007.

[27] C. C. Speake and C. J. Collins. Torsion Balances with Fibres of Zero Length. *Physics Letters A*, 382(16):1069–1074, Apr 26 2018.

[28] C. Gettings and C. C. Speake. A Method for Reducing the Adverse Effects of Stray-Capacitance on Capacitive Sensor Circuits. *Review of Scientific Instruments*, 90(2):025004, Feb 2019.

[29] C. Gettings and C. C. Speake. An Air Suspension to Demonstrate the Properties of Torsion Balances with Fibres of Zero Length. *Review of Scientific Instruments*, 91(2):025108, Feb 2020.

[30] H. J. Paik. Superconducting Tunable-Diaphragm Transducer for Sensitive Acceleration Measurements. *Journal of Applied Physics*, 47(3):1168–1178, 1976.

[31] C. C. Speake and G. T. Gillies. Why is G the Least Precisely Known Physical Constant? *Zeitschrift fur Naturforschung Section A-A Journal of Physical Sciences*, 42(7):663–669, Jul 1987.

[32] C. C. Speake, G. D. Hammond, and C. Trenkel. The Torsion Balance as a Tool for Geophysical Prospecting. *Geophysics*, 66(2):527–534, Mar-Apr 2001.

[33] E. C. Chalkley, S. Aston, C. J. Collins, M. Nelson, and C. C. Speake. Testing the Inverse Square Law of Gravitation at Short Range with a Superconducting Torsion Balance. In *The XLVIth Rencontres de Moriond and GPhyS Colloqium 2011*, pages 207–210, Mar 20-27 2011.

[34] C. C. Speake, G. Hammond, T. Matthews, E. Rocco, and F. Pena-Arellano. Precision Tests of Gravitation at Short Ranges. Grant Proposal, University of Birmingham, 2007.

[35] C. T. Siebold. *Development of a Superconducting Torsion Balance Designed to Search for a New Short-Range Force Coupling Quantum-Mechanical Spin and Matter.* PhD Thesis, University of Birmingham, Nov 1997.

[36] G. D. Hammond. *Development of a Spherical Superconducting Torsion Balance for Weak Force Physics.* PhD Thesis, University of Birmingham, Oct 1999.

[37] G. D. Hammond, A. Pulido-Paton, C. C. Speake, and C. Trenkel. Novel Torsion Balance Based on a Spherical Superconducting Suspension. *Review of Scientific Instruments*, 75(4):955–961, Apr 2004.

[38] G. D. Hammond, C. C. Speake, A. J. Matthews, E. Rocco, and F. Pena-Arellano. Development

of a Second Generation Torsion Balance Based on a Spherical Superconducting Suspension. *Review of Scientific Instruments*, 79(2):025103, Feb 2008.

[39] G. D. Hammond, C. C. Speake, C. Trenkel, and A. P. Paton. New Constraints on Short-Range Forces Coupling Mass to Intrinsic Spin. *Physical Review Letters*, 98(8), Feb 23 2007.

[40] C. J. Collins, 2014. Photograph.

[41] C. J. Collins, 2014. Graphic Diagram.

[42] C. C. Speake, G. D. Hammond, T. Matthews, E. Rocco, and F. Pena-Arellano. Precision tests of gravitation at short ranges. Technical report, University of Birmingham, 2007.

[43] J. Sullivan. Manufacturing Flat Discs and Testing the Smallest Separation Distance to Further the Progress of the Inverse Square Law Experiment. Master's Thesis, University of Birmingham, Mar 2018.

[44] N. Jones. Continuing Efforts to Investigate the Inverse Square Law of Gravity at 15µm. Master's Thesis, University of Birmingham, Mar 2018.

[45] C. C. Speake and C. Trenkel. Forces Between Conducting Surfaces Due to Spatial Variations of Surface Potential. *Physical Review Letters*, 90(16), Apr 25 2003.

[46] P. G. DeGennes and P. A. Pincus. *Superconductivity of Metals and Alloys*. Addison-Wesley Publishing Company, Incorporated, second edition, 1989.

[47] C. Kittel. *Introduction to Solid State Physics*. Wiley India Pvt. Limited, seventh edition, 2007.

[48] J. W. Rohlf. *Modern Physics from α to Z^0*. Wiley, first edition, 1994.

[49] D. J. E. Callaway. On the Remarkable Structure of the Superconducting Intermediate State. *Nuclear Physics B*, 344(3):627–645, Nov 19 1990.

[50] R. V. Jones and J. C. Richards. Design and Some Applications of Sensitive Capacitance Micrometers. *Journal of Physics E-Scientific Instruments*, 6(7):589–600, 1973.

[51] S. T. Smith and R. M. Seugling. Sensor and Actuator Considerations for Precision, Small Machines. *Precision Engineering-Journal of the International Societies for Precision Engineering and Nanotechnology*, 30(3):245–264, Jul 2006.

[52] K. Chatterjee, S. N. Mahato, S. Chattopadhyay, and D. De. High Accuracy Displacement Measuring System using Strain Gauge Based Displacement Sensor and Direct Sequence Spread Spectrum Techniques in Data Acquisition System. *Instruments and Experimental Techniques*, 60(1):154–157, Jan 2017.

[53] R. Oven. Modified Charge Amplifier for Stray Immune Capacitance Measurements. *IEEE Transactions on Instrumentation and Measurement*, 63(7):1748–1752, Jul 2014.

[54] Prabhu Ramanathan, Sudha Ramasamy, Prateek Jain, et al. Low Value Capacitance Measurements for Capacitive Sensors: A Review. In SY Yurish, editor, *Sensors, Transducers, Signal Conditioning and Wireless Sensors Networks*, volume 3 of *Advances in Sensors-Reviews*, pages 213–227. Int Frequency Sensor Assoc-IFSA, C/Esteve Terradas, Parc UPC-PMT, Edifici RDIT-KAM, 1, Barcelona, Castelldefels 08860, Spain, 2016.

[55] A. Bertolini, R. DeSalvo, F. Fidecaro, et al. Readout System and Predicted Performance of a Low-Noise Low-Frequency Horizontal Accelerometer. *Nuclear Instruments & Methods in Physics Research Section A - Accelerators Spectrometers Detectors and Associated Equipment*, 564(1):579–586, Aug 2006.

[56] M. Hu, Y. Z. Bai, Z. B. Zhou, Z. X. Li, and J. Luo. Resonant Frequency Detection and Adjustment Method for a Capacitive Transducer with Differential Transformer Bridge. *Review of Scientific Instruments*, 85(5), May 2014.

[57] *Amplifier Reference Manual*. Analog Devices, Inc., 1992.

[58] P. Horowitz and W. Hill. *The Art of Electronics*. Cambridge University Press, second edition, 1989.

[59] W. G. Jung. *IC Op-Amp Cookbook*. Howard W. Sams & Co., Inc., second edition, 1980.

[60] S. M. Huang, A. L. Stott, R. G. Green, and M. S. Beck. Electronic Transducers for Industrial Measurement of Low Value Capacitances. *Journal of Physics E: Scientific Instruments*, 21(3):242–250, Mar 1988.

[61] D. Marioli, E. Sardini, and A. Taroni. High-Accuracy Measurement Techniques for Capacitance Transducers. *Measurement Science and Technology*, 4(3):337–343, Mar 1993.

[62] F. Reverter, X. Li, and G. C. M. Meijer. Stability and Accuracy of Active Shielding for Grounded Capacitive Sensors. *Measurement Science and Technology*, 17(11):2884–2890, Nov 2006.

[63] E. M. Spinelli and F. Reverter. On the Stability of Shield-Driver Circuits. *IEEE Transactions on Instrumentation and Measurement*, 59(2):458–462, Feb 2010.

[64] A. Rich. Shielding and Guarding. *Analog Devices*, 17(1):8–13, 1983.

[65] S. K. Lamoreaux. The Casimir Force: Background, Experiments, and Applications. *Reports on Progress in Physics*, 68(1):201–236, Jan 2005.

[66] T. A. Wagner, S. Schlamminger, J. H. Gundlach, and E. G. Adelberger. Torsion-Balance Tests of the Weak Equivalence Principle. *Classical and Quantum Gravity*, 29(18), Sep 21 2012.

[67] G. T. Gillies and R. C. Ritter. Torsion Balances, Torsion Pendulums, and Related Devices. *Review of Scientific Instruments*, 64(2):283–309, Feb 1993.

[68] E. G. Adelberger, J. H. Gundlach, B. R. Heckel, S. Hoedl, and S. Schlamminger. Torsion balance experiments: A low-energy frontier of particle physics. In A Faesssler, editor, *Progress in Particle and Nuclear Physics, Vol 62, No 1*, volume 62 of *Progress in Particle and Nuclear Physics*, pages 102–134. Elsevier Science B.V., Sara Burgerhartstrat 25, PO Box 211, 1000 AE Amsterdam, Netherlands, 2009.

[69] D. J. McManus, P. W .F. Forsyth, M. J. Yap, et al. Mechanical Characterisation of the TorPeDO: a Low Frequency Gravitational Force Sensor. *Classical and Quantum Gravity*, 34(13):135002, 2017.

[70] T. Shimoda and M. Ando. Nonlinear Vibration Transfer in Torsion Pendulums. *Classical and Quantum Gravity*, 36(12):125001, May 2019.

[71] C. M. Mow-Lowry and D. Martynov. A 6D Interferometric Inertial Isolation System. *Classical and Quantum Gravity*, 36(24):245006, Nov 2019.

[72] C. C. Speake and D. B. Newell. The Design and Application of a Novel High-Frequency Tiltmeter. *Review of Scientific Instruments*, 61(5):1500–1503, May 1990.

[73] J. Harms and K. Venkateswara. Newtonian-Noise Cancellation in Large-Scale Interferometric GW Detectors Using Seismic Tiltmeters. *Classical and Quantum Gravity*, 33(23), Dec 8 2016.

[74] J. Joynson. Air-Bearing Suspension with Passive Magnetic Stabilisation and Tuning. Master's Thesis, University of Birmingham, Mar 2019.

[75] T. Quinn, C. C. Speake, H. Parks, and R. Davis. The BIPM Measurements of the Newtonian Constant of Gravitation, G. *Philosophical Transactions of the Royal Society A-Mathematical Physical and Engineering Sciences*, 372(2026), Oct 13 2014.

[76] W. R. Smythe. *Static and Dynamic Electricity*. Taylor & Francis, third edition, 1989.

[77] A. Aston and D. Hoyland. OSEM Interface Control Document. Advanced LIGO UK Internal Document LIGO-T050111-06-K, University of Birmingham, Sep 2004.